

**NASA
Technical
Paper
2771**

1988

Supersonic Aerodynamics of Delta Wings

Richard M. Wood

*Langley Research Center
Hampton, Virginia*



National Aeronautics
and Space Administration

Scientific and Technical
Information Division

Contents

Summary	1
Introduction	1
Symbols	1
Discussion	3
Aerodynamic and Geometric Parameters	3
Zero-Lift Wave Drag	3
Diamond airfoil	3
Circular-arc airfoil	5
Modified four-digit-series airfoil	5
Comments on zero-lift wave drag	7
Lifting Characteristics	7
Lee-side flow characteristics	7
Flat delta wings	8
Thickness effects	14
Camber effects	15
Comments on lifting characteristics	16
Real-Flow Wing Design	16
Concluding Remarks	19
Appendix—Nonlinear Methodology	20
References	22
Table	24
Figures	26

PRECEDING PAGE BLANK NOT FILMED

Summary

Through the empirical correlation of experimental data and theoretical analysis, a set of graphs have been developed which summarize the inviscid aerodynamics of delta wings at supersonic speeds. The zero-lift wave-drag characteristics of delta wings with diamond, circular-arc, and NACA modified four-digit-series airfoils were determined through the application of a nonlinear computational technique. The nonlinear analysis varied substantially from the exact linear-theory predictions for all combinations of geometry and flow parameters under study. For slender wings with highly subsonic leading edges, the nonlinear analysis showed that the zero-lift wave-drag correlation relationship was maintained; however, as the wing geometry became nonslender, the flow about the wing became nonlinear and the relationships which define the zero-lift wave-drag correlation parameter were not maintained.

The aerodynamic characteristics of delta wings at lifting conditions have been evaluated for the effects of wing leading-edge sweep, leading-edge bluntness, and wing thickness and camber and then summarized in the form of graphs which may be used to assess the aerodynamics in the preliminary design process. Empirical curves have been developed for the lift-curve slope, nonlinear lift effects, maximum lift, longitudinal stability, and distribution of lift between the upper and lower surfaces of a wing. In addition, the impact of various airfoil parameters, wing leading-edge sweep, and lift coefficient on the drag-due-to-lift characteristics has been shown theoretically.

The various graphs which detail the aerodynamic performance of delta wings at both zero-lift and lifting conditions were then employed to define a preliminary wing design approach in which both the low-lift and high-lift design criteria were combined to define a feasible design space.

Introduction

An extensive survey of the literature reveals that supersonic aerodynamic research began in the 1940's. The literature survey showed that during the 1940's and 1950's most of the experimental studies at supersonic speeds were conducted on simple wings, bodies, and wing-body geometries as the aerodynamicists attempted to determine the nature of the new flow regime. However, with the introduction of linear theory in the 1950's and the emergence of high-speed computers in the 1960's, there was a gradual decline in the amount of experimental research directed toward the study of fundamental flows over simple wings and bodies and a large increase in research directed toward the application of linear theory to the

design of aerodynamic vehicles. This change in research emphasis was no doubt highly influenced by the challenge of a new frontier—efficient supersonic flight.

In the design of an optimum wing at supersonic speeds, the aerodynamicist may select from an infinite array of wing planforms, airfoil profiles, and camber and twist distributions to meet the desired aerodynamic performance requirements. Historically, the aerodynamicist relied heavily on linear theory for the selection of all wing parameters. However, comparison of linear-theory estimates with experimental data for wings has shown an inability of the theory to consistently predict the measured results (ref. 1). Linearized theory computational tools were limited by the constraints inherent to small perturbation theory.

An extensive survey of the literature was conducted to determine the dominant wing geometric characteristics and flow conditions which should be used in assessing the supersonic aerodynamics of wings. The initial result of this effort was the identification of the delta or triangular wing planform as the most likely candidate for future parametric supersonic wing studies due to the extensive experimental data base which was available. In addition, the empirical correlations derived for delta wings could be extended to other simple wing planforms, such as arrow and diamond wings, through the use of the geometric and flow correlation parameters.

This paper presents the results of a combined experimental and theoretical study of the aerodynamics of delta wings at supersonic speeds along with a preliminary delta wing selection and design philosophy. The supporting information for this study was derived from both the application of a nonlinear inviscid computational method (ref. 2) and from published force, pressure, and flow visualization data for delta wings.

Results of this study should provide a better understanding of the effect that airfoil profile, wing sweep, and Mach number have on the aerodynamics of delta wings at supersonic speeds and should establish the limitations of linear and nonlinear theories to predict these effects. The results of the study are presented in a parametric fashion in an effort to consolidate the effects of wing sweep, Mach number, and airfoil shape.

Symbols

A	wing aspect ratio
b	wing span
C_D	drag coefficient, $\frac{\text{Drag}}{qS}$

ΔC_D	change in drag coefficient relative to flat wing at zero lift	M_N	component of Mach number normal to wing leading edge, $M \cos \Lambda$ $(1 + \sin^2 \alpha \tan^2 \Lambda)^{1/2}$
$\Delta C_D/\beta C_L^2$	drag-due-to-lift parameter	m	position of airfoil maximum thickness, expressed as a fraction of local chord
$C_{D,W}$	zero-lift wave-drag coefficient	N_{Re}	Reynolds number
$C_{D,W}(DX)$	axial integration drag coefficient	q	dynamic pressure
$C_{D,W}(x)$	sectional drag coefficient	R	leading-edge radius parameter for NACA modified four-digit-series airfoil, Leading-edge radius = $c[1.1019(\tau R/6)^2]$
C_L	lift coefficient, $\frac{\text{Lift}}{qS}$	r	position of airfoil maximum thickness
ΔC_L	nonlinear incremental change in lift coefficient with respect to linear lift coefficient, $C_L _{\alpha=20^\circ} - 20C_{L\alpha}$	S	wing reference area
$C_{L,\max}$	maximum lift coefficient	$S(x)$	local wing cross-sectional area
$C_{L\alpha}$	lift-curve slope, evaluated at zero lift, per deg	t	wing airfoil thickness
C_m	pitching-moment coefficient, $\frac{\text{Pitching moment}}{qS\bar{c}}$	x	streamwise coordinate
ΔC_m	nonlinear increment in pitching-moment coefficient with respect to linear pitching-moment coefficient, $C_m _{\alpha=20^\circ} - 20\frac{dC_m}{d\alpha} _{\alpha=0^\circ}$	x_{cp}	streamwise center of pressure
C_N	normal-force coefficient	y	spanwise coordinate
C_N^ℓ	wing lower surface normal-force coefficient	y_{cp}	spanwise center of pressure on the wing semipanel
C_N^u	wing upper surface normal-force coefficient	y_{LE}	spanwise position of leading edge
C_p	coefficient of pressure	z	vertical coordinate
$C_{p,o}$	coefficient of pressure at zero lift	α	angle of attack
$C_{p,\min}^u$	minimum wing upper surface pressure coefficient	α_N	angle of attack normal to wing leading edge, $\tan^{-1} \frac{\tan \alpha}{\cos \Lambda}$
$C_{p,v}$	vacuum pressure coefficient, $-2/\gamma M^2$	β	$= \sqrt{M^2 - 1}$
c	wing chord	$\beta C_{L\alpha}$	lift-curve-slope parameter, per deg
\bar{c}	wing mean geometric chord	$\beta \cot \Lambda$	leading-edge sweep parameter
c_r	wing root chord	γ	ratio of specific heats, 1.40 for air
DX	marching step size used in nonlinear analysis	η	fraction of local wing semispan
dC_m/dC_L	longitudinal stability level evaluated at zero lift, per deg	η_v	semispan location of vortex action line
K	zero-lift wave-drag correlation parameter, $C_{D,W}/\tau^2 A$	Λ	wing leading-edge sweep angle, deg
LE	leading edge	τ	airfoil thickness parameter, expressed as fraction of local chord, t/c
M	Mach number	Subscripts:	
		C	cross flow
		ref	reference

Discussion

The present study is directed toward understanding the fundamental aerodynamic performance of delta wings through empirical correlations of experimental data and nonlinear computations. Nonlinear analysis is used only when there are insufficient experimental data with respect to a particular geometric or flow parameter under investigation. The data base used in this study is from references 3 through 25 and summarized in table I.

The geometric and flow parameters under investigation are presented first. The zero-lift drag results are then presented followed by the lifting characteristics.

Aerodynamic and Geometric Parameters

The identification of an adequate correlation parameter is critical to any empirical study. For delta wings, linear theory indicates that at supersonic speeds all aerodynamic characteristics are a function of the leading-edge flow condition, as described by the leading-edge sweep parameter $\beta \cot \Lambda$. In addition, the aspect ratio of a delta wing is defined as being four times the cotangent of the wing leading-edge sweep angle. (See fig. 1.)

Presented in figure 1 is a plot representing the range of leading-edge sweep under study, and presented in figure 2 is a plot of Mach number against $\beta \cot \Lambda$ for a range of Λ . Wings with aspect ratios varying from a minimum of 0.5 to a maximum of 4.0 were selected as being representative supersonic planforms (fig. 1). Also indicated in figure 2 is the sonic leading-edge condition ($\beta \cot \Lambda = 1.0$) for delta wings. The data of figure 2 show that increasing aspect ratio significantly reduces the Mach number for a given value of $\beta \cot \Lambda$.

The zero-lift drag study concentrated on the effect of airfoil profile on the supersonic aerodynamics of delta wings. The study includes a parametric investigation of diamond, circular-arc, and NACA modified four-digit-series airfoils (ref. 26) in which the effect of thickness ratio τ for all airfoils, maximum thickness position m for the diamond and NACA modified four-digit-series airfoils, and leading-edge bluntness R for the NACA modified four-digit-series airfoil is presented. The range of geometric parameters is graphically presented in figures 3, 4, and 5. Thickness ratio varies from 0.02 to 0.10; maximum thickness position, from 0.2 to 0.5; and leading-edge radius parameter, from 0.0 to 8.0 within the present study.

Zero-Lift Wave Drag

Supersonic linear theory suggests that the zero-lift wave-drag ($C_{D,W}$) of a delta wing varies as the airfoil thickness-to-chord ratio squared (τ^2) and as the wing aspect ratio (A) for a given airfoil profile. In 1957, Bishop and Cane (ref. 27) incorporated the dependence of the zero-lift wave drag upon Mach number into the standard linear-theory drag curves by combining the Mach number parameter β with the wing geometric parameter A and then plotting the linear-theory-dependence parameter ($C_{D,W}/\tau^2 A$) against the leading-edge sweep parameter ($\beta \cot \Lambda$). This method of presentation represents a plot of zero-lift wave drag against Mach number for a given wing airfoil shape rather than curves showing the effect on wave drag of one or more wing geometric parameters as had been done previously (ref. 28).

The primary intent of this section of the paper is to establish the dependence of the zero-lift wave drag for delta wings on τ^2 , A , and M for various airfoil profiles. The dependence is established through nonlinear aerodynamic analysis with the method of reference 2 because of a lack of experimental data. Nonlinear solutions are only presented for subsonic leading-edge conditions due to a restriction in the present full-potential solution technique. All zero-lift wave-drag plots are in the format established by Bishop and Cane.

Diamond airfoil. Computations of the zero-lift drag of three-dimensional wings with diamond airfoils have dominated the theoretical wave-drag studies. The simplicity of the geometry lends itself to a closed-form solution of the linearized equations. A comparison of the nonlinear and linear solutions for delta wings with diamond airfoils is presented in figure 6. Nonlinear solutions were obtained with the method of reference 2, and the linear solutions are taken from the closed-form solutions presented in reference 27. Attempts to exactly duplicate the closed-form linear-theory solutions of reference 27 with linear-theory computer codes (ref. 29) were unsuccessful because of the inaccuracies inherent to the numerical techniques employed to solve the equations. The best results received from the linear-theory codes had a maximum error, referenced to the closed-form solution, of 5 percent. Nonlinear-and linear-theory curves are presented for positions of maximum airfoil thickness (m) of 0.2, 0.3, 0.4, and 0.5. The linear-theory curves represent the zero-lift wave drag of all delta wings. The nonlinear curves were computed for a 4-percent-thick delta wing of aspect ratio 1.0. The delta wing with aspect ratio of 1.0 was selected for nonlinear calculations because

of the large variation in Mach number which could be analyzed for values of $\beta \cot \Lambda$ from 0.125 to 1.0. A review of figure 2 shows that values of $\beta \cot \Lambda$ between 0.125 and 1.0 correspond to a Mach number range of 1.12 to 4.12 for a wing with $A = 1.0$ compared with a Mach number range of 1.01 to 1.67 for a wing with $A = 3.0$.

Linear-theory zero-lift wave-drag predictions (fig. 6) show a large effect of the position of airfoil maximum thickness and increasing $\beta \cot \Lambda$. The results indicate that, for values of $\beta \cot \Lambda$ less than 0.6, a forward shift in the position of airfoil maximum thickness from 0.5 to 0.2 results in a reduction in drag of 80 percent. For values of $\beta \cot \Lambda$ greater than 0.8, a rearward shift in the position of airfoil maximum thickness from 0.2 to 0.5 would also produce a reduction in drag of 80 percent. For values of $\beta \cot \Lambda$ between 0.6 and 0.8, the relationship between the four linear-theory curves varies drastically. In this range of $\beta \cot \Lambda$, the airfoil maximum thickness lines become supersonic (Mach angle exceeds the maximum thickness line sweep angle) for each airfoil at different values of $\beta \cot \Lambda$. When the Mach number normal to the airfoil maximum thickness sweep line becomes supersonic, a singularity arises in the linear solution which produces a large drag rise (first peak). The second peak of each linear-theory curve corresponds to the drag rise associated with the occurrence of a sonic leading-edge condition; this occurs at $\beta \cot \Lambda = 1.0$ for delta wings. As Mach number is increased beyond the sonic leading-edge condition, $\beta \cot \Lambda > 1.0$, linear theory predicts a gradual reduction in the drag coefficient for all diamond airfoils.

Nonlinear zero-lift wave-drag estimates for the effect of the position of maximum airfoil thickness and Mach number are similar to the linear predictions; however, the details of the four nonlinear curves are significantly different from their linear-theory counterparts. Both linear and nonlinear theories predict a crossover in the four curves; however, the linear-predicted crossover occurs over a range of $\beta \cot \Lambda$ from 0.6 to 0.8, and the nonlinear-predicted crossover for all curves occurs at $\beta \cot \Lambda = 0.6$, indicating that, at $\beta \cot \Lambda = 0.6$, the drag of a delta wing with a diamond airfoil is independent of the position of airfoil maximum thickness. On either side of this crossover point in the drag curves the effect of the position of maximum airfoil thickness is similar to that predicted by linear theory. In general, the nonlinear analysis results show a much smoother variation with $\beta \cot \Lambda$ (no peaks or valleys) and lower drag than the linear-theory estimates. Nonlinear theory predicts lower drag for all conditions except for the curve for $m = 0.2$ for values of $\beta \cot \Lambda$ between 0.2 and 0.7

and the curve for $m = 0.3$ for values of $\beta \cot \Lambda$ between 0.275 and 0.55.

The large differences between the linear and nonlinear predictions do not solely establish the existence of nonlinear flow over the wings, such as large shocks or expansions. A comparison of the two methods shows that the linear method tends to predict a sharp pressure gradient due to local surface discontinuities, whereas the nonlinear method predicts a much more gradual change in pressure. For $\beta \cot \Lambda < 0.4$, the flow calculated with the nonlinear theory is subcritical in the cross-flow plane ($M_C < 1.00$), and the forces predicted by linear and nonlinear theories are in close agreement. At $\beta \cot \Lambda > 0.75$, the two solutions diverge and a comparison of the calculated flow fields, with the nonlinear code, reveals the development of supercritical cross-flow conditions ($M_C > 1.00$). However, for values of $\beta \cot \Lambda$ between 0.4 and 0.75, the flow about the wing is subcritical yet the differences between the linear and nonlinear curves are significant. To provide insight into the flow condition in this region, spanwise surface pressure distributions from the nonlinear analysis are shown in figure 7 for a delta wing with a 4-percent-thick diamond airfoil and aspect ratio of 1.0 at a Mach number of 2.60, $\beta \cot \Lambda = 0.6$. Predicted pressure results are presented for airfoils with $m = 0.2$ and 0.5 at streamwise positions of 20, 40, 60, and 80 percent of the root chord. A comparison of the pressures for the two airfoils shows a smooth and subcritical character to the flow with larger spanwise pressure gradients occurring for the airfoil with $m = 0.2$. The forward position of the airfoil maximum thickness creates an effectively blunter airfoil ($m = 0.2$); this results in larger compression pressures at the leading edge and lower expansion pressures as the flow expands around the airfoil ridge line when compared with the airfoil with $m = 0.5$. The equivalent drag values, at $\beta \cot \Lambda = 0.6$, which result from an integration of the pressure data are due to compensating drag characteristics in the streamwise direction. Over the forward portion of the wings ($0 < x/c_r < 0.3$), the local drag of the airfoil with $m = 0.2$ is greater than that of the airfoil with $m = 0.5$; between x/c_r of 0.3 to 0.7, the drag is similar; and over the aft portion of the wing ($0.7 < x/c_r < 1.0$), the drag of the airfoil with $m = 0.5$ is greater because of the increased slope at the trailing edge.

Selected nonlinear analysis was performed next to establish the dependence of the wave drag upon the thickness-to-chord ratio squared (τ^2) and aspect ratio (A) for delta wings with diamond airfoils. Presented in figure 8 is the predicted nonlinear effect for

a thickness variation from 0.02 to 0.10 and an aspect ratio variation from 0.5 to 3.0. Results are presented as a ratio of the nonlinear-predicted zero-lift wave drag for each geometry to a reference nonlinear-predicted zero-lift wave drag which has been scaled by the ratios of the computed to reference wing aspect ratios (A/A_{ref}) and thickness-to-chord ratio squared ($(\tau/\tau_{\text{ref}})^2$):

$$\frac{C_{D,W}(A, \tau)}{C_{D,W}(A_{\text{ref}}, \tau_{\text{ref}}) (A/A_{\text{ref}})(\tau/\tau_{\text{ref}})^2}$$

Thickness effects, presented on the left of figure 8, were evaluated for a reference delta wing with $A = 1.0$, $m = 0.5$, and an airfoil with $\tau = 0.04$ at $\beta \cot \Lambda = 0.25$, 0.5, and 0.75. The nonlinear analysis shows a reduced drag with increasing thickness compared with the value estimated with the zero-lift wave-drag correlation parameter (K). The data on the left of figure 8 show that, at $\beta \cot \Lambda = 0.25$, the linear-theory-dependence relationship is maintained within 2 percent; for $\beta \cot \Lambda = 0.5$, a 10-percent variation is observed; and for $\beta \cot \Lambda = 0.75$, a 20-percent variation is found. At $\beta \cot \Lambda = 0.75$, the predicted cross-flow Mach number is supercritical for the 4-percent-thick wing (figs. 7 and 8); an increase in thickness would only tend to magnify these effects. Note that solutions could not be attained for wings with zero thickness ($\tau = 0.00$) with the selected nonlinear methodology; however, by definition an exact agreement between the linear and nonlinear solutions would occur. Presented on the right of figure 8 is the effect of aspect ratio for a reference delta wing with $A = 1.0$, $\tau = 0.04$, and $m = 0.2$ at $\beta \cot \Lambda = 0.5$ and 0.75. Nonlinear analysis shows a nonlinearly increasing drag with increasing aspect ratio and a maximum perturbation of 5 percent for $\beta \cot \Lambda = 0.75$ and 10 percent for $\beta \cot \Lambda = 0.5$.

Nonlinear analysis of delta wings with diamond airfoils has shown that for $\beta \cot \Lambda$ less than 0.5 (subcritical range), the zero-lift wave drag varies with the thickness squared and aspect ratio, but for higher values of $\beta \cot \Lambda$ (supercritical range), the nonlinear results diverge significantly from the linear-theory-dependence relationship. Within this supercritical range, the nonlinearity of the flow over the wing increases significantly and is shown to be dependent upon both the wing and airfoil geometries.

Circular-arc airfoil. The circular-arc profile is a unique class of airfoils which is often used in the design of supersonic vehicles. The uniqueness of the circular-arc airfoil lies in the fact that it has only a single design parameter—airfoil thickness.

Except for the diamond profile, it is probably the airfoil most frequently used in fundamental studies of wings. Presented in figure 9 is a comparison of the axial distributions of area and drag for a series of equivalent 4-percent-thick sharp airfoils on a delta wing with $A = 1.0$ at $M = 1.80$. The three airfoil profiles are a diamond with $m = 0.5$, a circular arc, and a sharp modified four-digit series with $m = 0.5$. The diamond and modified four-digit-series airfoils are presented in this section of the paper to provide a reference point for discussions on the circular-arc profile. The axial distributions of area and drag show that the circular-arc airfoil and the equivalent sharp modified four-digit-series airfoil ($m = 0.5$, $R = 0$) are similar, and both have a greater volume and a different axial drag distribution than those for the diamond airfoil. The drag characteristics show that the circular-arc airfoil has higher drag than the diamond airfoil at the apex and trailing edge; this is due to the increased surface slopes in these regions.

The effect of Mach number on the nonlinear-predicted drag characteristics of the circular-arc airfoil is presented in figure 10. Also shown in the figure are the nonlinear drag characteristics of the equivalent modified four-digit-series airfoil and the diamond airfoil, along with the linear-theory solution for the diamond airfoil with $m = 0.5$. Nonlinear analysis shows a smooth variation in drag for $\beta \cot \Lambda$ between 0.125 and 1.0. Comparison of the drag levels shows that the diamond airfoil has the lowest drag, the modified four-digit-series airfoil has the highest, and the circular-arc profile has drag slightly less than that for the modified four-digit-series profile. These results are consistent with the data presented in figure 9.

Predicted nonlinear effects of airfoil thickness and wing aspect ratio for the circular-arc airfoil (fig. 11) are similar to those observed for the diamond airfoil. The analysis shows a decreasing drag value with increasing airfoil thickness and an increasing drag value with increasing wing aspect ratio. The data also show a greater percentage change in drag for the circular-arc airfoil than for the diamond airfoil (fig. 8) due to increasing $\beta \cot \Lambda$. This increased nonlinear variation in the drag is due to an increased amount of nonlinear-predicted flow over the wing with increasing Mach number. The analysis results presented in figures 9, 10, and 11 indicate that a different complex and nonlinear flow structure exists for the circular-arc airfoil than for the diamond airfoil. In addition, the characteristics for the circular-arc airfoil were shown to be very similar to those for the equivalent modified four-digit-series airfoil; this suggests that the circular-arc profile can be treated as a subset of the modified four-digit-series airfoil family. The

analysis clearly shows that the zero-lift drag of sharp airfoils with the same values of τ and m is not equal; the circular arc has 15 to 40 percent higher wave drag than the diamond airfoil but only 4 percent less drag than the equivalent modified four-digit-series airfoil.

Modified four-digit-series airfoil. The NACA modified four-digit-series airfoil was selected for the study of blunt leading-edge airfoils because of the flexibility in defining and altering the airfoil profile. The NACA modified four-digit-series airfoil family is defined analytically with the following three parameters: airfoil thickness (τ), position of airfoil maximum thickness (m), and leading-edge radius parameter (R). The leading-edge radius of the modified four-digit series is a function of the leading-edge radius parameter (R) and the airfoil thickness parameter (τ) through the relationship:

$$\text{Leading-edge radius} = c[1.1019(\tau R/6)^2]$$

This airfoil family is used to evaluate the effect of leading-edge bluntness in addition to the effects of τ , m , A , and M on the zero-lift wave drag. Results of the nonlinear analysis for the diamond and circular-arc airfoils are referenced. To provide insight into the geometric character of this class of airfoils, the axial distribution of area and drag for various values of the parameters m and R is presented in figure 12. Nonlinear results are presented for a 4-percent-thick delta wing with $A = 1.0$ at $M = 1.41$, $\beta \cot \Lambda = 0.25$. The effect of the position of airfoil maximum thickness is shown at the left of the figure for sharp airfoils. The area distribution shows that moving the airfoil maximum thickness forward results in a forward shift in wing volume and a decrease in the maximum cross-sectional area. These two effects combine to produce a smoother area distribution and lower drag.

A review of the axial distribution of drag for the airfoil with $m = 0.2$ shows longitudinal symmetry, whereas the drag of the airfoil with $m = 0.5$ is mostly generated over the final 20 percent of the wing length. The integrated drag values (ref. 2), which are listed in figure 12, show that the airfoil with $m = 0.5$ has 60 percent higher drag than the airfoil with $m = 0.2$. As Mach number is increased, the character of the drag for each airfoil changes dramatically as the compressive pressures begin to dominate the flow. The apex drag of the airfoil with $m = 0.2$ would be expected to increase significantly compared with the airfoil with $m = 0.5$, and the trailing-edge drag of both airfoils would reduce.

Shown on the right of figure 12 is the effect of leading-edge bluntness on the axial distribution of

area and computed nonlinear drag. Results are presented for a 4-percent-thick airfoil with $m = 0.5$ at $R = 0$, 4.0, and 8.0, which correspond to a leading-edge radius, expressed as a fraction of the chord, of approximately 0.0, 0.001, and 0.003, respectively. The area and drag data clearly show that leading-edge bluntness only affects the forward half of the wing. Drag data show that increasing airfoil bluntness produces a localized increase in drag at the wing apex followed immediately by a rapid reduction in drag. At $x/c_r = 0.4$, the data show a merging of the drag data for the three airfoils which then remain coincident over the remainder of the geometry. The crossover in the drag data of the three airfoils which occurs at the apex of the wing produces a canceling effect that results in a drag value of approximately 21 counts (0.0021) for the three airfoils. This independent nature of the drag due to changes in leading-edge bluntness is discussed further later.

The fundamental nonlinear characteristics for the modified four-digit-series airfoil are established for 4-percent-thick sharp airfoils on a wing with $A = 1.0$. The dependence of the drag on the thickness, aspect ratio, and leading-edge bluntness is established separately.

Presented in figure 13 are the nonlinear-theory predictions of drag characteristics for sharp modified four-digit-series airfoils with maximum thickness locations of 0.2, 0.3, 0.4, and 0.5. Results are presented for values of $\beta \cot \Lambda$ between 0.125 and 1.0. The nonlinear analysis shows trends similar to those predicted for the diamond airfoil: smooth variations with $\beta \cot \Lambda$ and a crossover in the drag of all geometries over a range of $\beta \cot \Lambda$ from 0.65 to 0.8. The crossover for the modified four-digit-series airfoil occurs at a value of $\beta \cot \Lambda$ of approximately 0.7 compared with a value of 0.6 for the diamond airfoil. The data show that, for values of $\beta \cot \Lambda$ less than 0.65, moving the maximum airfoil thickness position from 0.5 to 0.2 reduces the drag by a maximum of 50 percent, and for values greater than 0.8, a rearward shift in the maximum airfoil thickness position from 0.2 to 0.5 produces a maximum drag reduction of 30 percent.

The zero-lift wave-drag correlation parameter is evaluated for the modified four-digit-series airfoil in figure 14. The trends and levels for both the effects of thickness and aspect ratio are similar to the results for the circular-arc airfoil. The nonlinear predictions show a maximum variation of 30 percent for thickness variations from 0.02 to 0.10 and a 15-percent variation for variations in aspect ratio from 0.5 to 3.0. A comparison of these results with those for the circular-arc and diamond airfoils shows an increase in the nonlinearity of the characteristics with increasing

geometric complexity. However, as mentioned previously, the discrepancy between the nonlinear predictions and the linear-theory-dependence parameter estimates is probably due to a combination of an increased nonlinear flow field and a less accurate resolution of the geometry within the solution.

The effect of leading-edge bluntness on the drag characteristics of wings is a highly debated and important question in the design of wings and complete aircraft configurations. In general, previous supersonic wing design studies which were based upon linear theory would frequently employ a sharp airfoil or small amounts of bluntness on the leading edge of the wing in order to minimize the zero-lift wave-drag penalty.

Presented in figure 15 is the nonlinear-predicted effect of airfoil bluntness on the zero-lift wave drag of various modified four-digit-series airfoil geometries. The nonlinear analysis shows that increasing leading-edge bluntness in combination with increasing maximum thickness position, increasing thickness, or increasing Mach number generally produced increasingly larger drag reductions when compared with a sharp leading edge, with a maximum drag reduction of 6 percent occurring for $\beta \cot \Lambda = 0.75$ and $R = 4.0$. However, the magnitudes of all the variations in drag with increasing leading-edge bluntness are small compared with the effect of m , M , τ , and A observed in figures 14 and 15. This analysis clearly shows that leading-edge bluntness is the least influential geometric parameter on zero-lift wave drag for subsonic leading-edge conditions, despite the increased nonlinearity in the wing flow field.

Presented in figure 16 are the spanwise surface pressure coefficient data predicted by nonlinear theory for two delta wings with $A = 1.0$ and 4-percent-thick modified four-digit-series airfoils with $m = 0.5$ and $R = 0$ and 8.0 . The analysis was performed at $M = 3.16$, $\beta \cot \Lambda = 0.75$, which corresponds to geometries which have similar drag values (see right side of fig. 15) and are relatively independent of maximum thickness position (see fig. 13). Predicted pressure distributions are presented for $x/c_r = 0.2$, 0.4 , 0.6 , and 0.8 . The data show that, at $x/c_r = 0.2$, the blunt airfoil experiences higher surface pressures over the total span compared with the sharp airfoil. For x/c_r values of 0.4 , 0.6 , and 0.8 , the blunt airfoil experiences an expansion (low pressures) at the leading edge and an overall pressure distribution which is lower or equal to that of the sharp airfoil. The lower pressures at the leading edge result from the expansion of the flow around the airfoil nose; thus, an aerodynamic thrust force is produced which counteracts the drag increase produced by the more positive pressures at the apex of the wing. These

findings also support the data presented in figure 15 in which the axial distributions of drag for a wing with a sharp and a blunt airfoil were shown to cross over just aft of the wing apex producing a canceling effect of the local drag.

Comments on zero-lift wave drag. Predicted nonlinear zero-lift wave-drag characteristics of delta wings with diamond, circular-arc, and NACA modified four-digit-series airfoils have been shown to vary substantially from the characteristics predicted by linear theory. The nonlinear analysis suggests that for slender delta wings at small values of $\beta \cot \Lambda$ the zero-lift wave-drag correlation relationship is maintained to a higher degree; however, as the wing aspect ratio or airfoil thickness ratio increases, the flow about the wing becomes more nonlinear and the zero-lift wave-drag correlation parameter is not maintained. The delta wing drag curves presented in figures 6, 10, and 13 should be adequate for the preliminary design studies of delta wings (aspect ratio, Mach number, and airfoil selection).

Lifting Characteristics

The ability to take into account the effect of airfoil profile, aspect ratio, and Mach number on the lifting characteristics of delta wings is extremely important in selecting the proper wing geometry. The predicted flow about a delta wing at the zero-lift condition has been shown to be a strong function of these parameters, and as the wing is taken to a lifting condition, the nonlinear effects would be expected to increase significantly (ref. 30). The existing design philosophy for delta wings, which is based upon linear theory, assumes that the lift and drag due to lift of a flat wing are only a function of the leading-edge sweep angle and Mach number. The lifting characteristics are presented in the form of summary graphs in which the drag, lift, and pitching-moment characteristics are highlighted.

Lee-side flow characteristics. At zero angle of attack, the flow over the upper and lower surfaces of the wing is characterized as attached; however, as the wing is taken to angle of attack, the lee-side flow characteristics can change dramatically (ref. 21). In general the lee-side flow over a wing at angle of attack can be divided into two categories: attached or separated. The development and character of each flow type are dependent upon wing planform, airfoil profile, and wing camber in addition to the free-stream flow conditions.

The values of M_N and α_N conducive to the existence of an attached flow over the lee side of a zero-thick delta wing are shown at the top of figure 17 (ref. 21). At zero- to low-lift conditions, the

flow is subcritical in the cross-flow plane (small cross-flow velocity) with the primary flow direction being streamwise. As lift is increased, the flow turning angle about the leading edge becomes greater, thus resulting in an acceleration of the flow and an increase in the inboard flow component. The cross flow will eventually turn streamwise as the flow recompresses. Further increases in lift increase both the cross-flow component of the flow and the resultant recompression as shown in figure 17 and will eventually produce a cross-flow shock. The occurrence of a cross-flow shock system is an indication of the existence of nonlinear supercritical-type flow. Further increases in lift result in shock-induced separation of the boundary layer and the formation of a leading-edge bubble.

The second type of flow which occurs on the lee side of a wing is a leading-edge separation system, which is characterized by a viscous, rotational mass of air that resides inboard of the wing leading edge. (See the lower portion of fig. 17.) At low-lift conditions, a leading-edge bubble develops, and as the angle of attack is increased, the bubble lifts off the wing surface and evolves into a vortex. Further increases in angle of attack result in the development of a secondary vortex and eventually a vortex with shock occurs. For a vortex system, the vortex body is connected to the wing surface via the vortex stem or feed sheet. The feed sheet is also a viscous flow region that emanates from the wing boundary layer near the wing leading edge. The shape and position of the viscous vortex system are dependent upon the flow field external to the vortex which interacts with the vortex system until an equilibrium condition is established. In the steady-state model, the vortex system acts as a physical boundary to the external flow field system boundary. The free-stream flow expands around the wing leading edge and follows the contour of the vortex system undergoing an expansion followed by a recompression as the flow turns about the vortex.

This flow field external to, yet influenced by the viscous vortex system, is termed the "induced flow field." The extent of the induced flow field is characterized by a stagnation point or reattachment line on the wing upper surface inboard of the vortex body. Inboard of this induced flow field is the potential flow field, where the flow is attached in a streamwise direction.

The effects of angle of attack, Mach number, and leading-edge sweep on the vortex location were detailed in reference 31. (See fig. 18.) As shown in the sketch, the vortex action line is identified as the fraction of the local wing semispan η_v . The vortex action line is the position at which the

vortex normal-force vector should be placed to give the same wing bending moment as produced by the vortex pressures. The data show that the vortex position depends mainly on angle of attack and leading-edge sweep angle. Typically the vortex moves from a location near 80 percent semispan to a location near 50 percent semispan as angle of attack changes from 4° to 20°.

The lee-side flow descriptions presented are typical for any wing geometry at both subsonic and supersonic speeds. However, the magnitudes of these individual effects differ substantially with Mach number. The most notable of these differences are observed in the static pressures measured on the wing upper surface. As Mach number increases beyond 1.0, the free-stream static pressure decreases rapidly to significantly reduce the aerodynamic impact of the expansion over the wing lee side.

Flat delta wings. This section of the paper draws upon several previous empirical correlations (refs. 3, 4, 32, and 33) as well as the extensive data base in order to investigate how wing leading-edge sweep, Mach number, and angle of attack affect the lifting characteristics of delta wings. The supersonic aerodynamic characteristics of flat uncambered delta wings are presented in figures 19 through 37. All aerodynamic characteristics are presented in a parametric fashion in order to consolidate a wide range of geometric and flow conditions and in an effort to provide a set of empirical aerodynamic curves which may be used in preliminary supersonic wing design.

The characteristic lift-curve slope, nonlinear lift effects, and maximum lift for flat delta wings are presented in figures 19, 20, 21, and 22. The data presented in figure 19 are an extension to the analysis of reference 4 in which additional data sets have been evaluated to establish definitive aerodynamic characteristics of delta wings. The experimental data shown in figure 19 represent a wide range of wing leading-edge sweep, airfoil thickness, and airfoil shape; however, the primary distinguishing feature of the data is that of airfoil bluntness, as noted by the open and solid symbols. A comparison of the experimental data with linear-theory results shows excellent agreement; for values of $\beta \cot \Lambda$ below 0.5 and between 0.5 and 1.0, the experimental data break away from the linear-theory curve and show lift-curve-slope values below those predicted by linear theory. The data of figure 20 show that not until a value of $\beta \cot \Lambda$ of approximately 2.0 do the experimental data reach the linear-theory level. A close examination of the data also shows a division of the two experimental data sets with the sharp leading-edge data falling below the blunt leading-edge data.

The scattering of the two data sets could be due to an effective bluntness that may occur for the sharp-edge wings which have large thickness or those which have the maximum thickness position near the leading edge. The change in characteristic lift-curve slope with leading-edge bluntness and increasing $\beta \cot \Lambda$ indicates a change in the local wing flow characteristics from the linear-theory model. Linear theory assumes that all flow disturbances are weak and are propagated along Mach lines. For small values of $\beta \cot \Lambda$, the disturbances are weak and the Mach cone is an excellent approximation of the bow shock, but as the free-stream Mach number is increased (increasing $\beta \cot \Lambda$), the differences between the linear-theory Mach cone and the finite-strength bow shock increase; this indicates the growth of a strong nonlinear disturbance field. This effect tends to produce a change in flow angularity, a loss in energy, and a reduction in the Mach number at the wing leading edge. Further increases in Mach number, angle of attack, or $\beta \cot \Lambda$ produce greater changes in all flow conditions and a reduced lift effectiveness compared with those for the linear-theory model. The increased lift-curve slope with increased wing leading-edge bluntness is attributed to both the increased expansion of the flow about the wing leading edge onto the wing upper surface and the increased lower surface compression pressures.

Presented in figure 20 are lift-curve slopes predicted by nonlinear theory for delta wings with sharp and blunt leading edges. A comparison of the linear, nonlinear, and experimental data shows that the linear-theory analysis is in very good agreement with the experimental data and nonlinear-theory analysis for values of $\beta \cot \Lambda$ less than 0.5. For values of $\beta \cot \Lambda$ greater than 0.5, the nonlinear analysis and experimental data show a lower lift-curve slope than that predicted by linear theory. At these large values of the leading-edge sweep parameter, the nonlinear-theory analysis of wave drag at zero lift (fig. 6) also shows an increase in the nonlinear characteristics of the flow and a diverging of the two solutions.

The effect of airfoil bluntness on the lift characteristics was studied on the modified four-digit-series airfoil. Analysis was performed over a range of angle of attack from 0° to 10° in which the linearity of the lift-curve slope was established within 3 percent. The nonlinear analysis and experimental data are in excellent agreement and both compare well with linear theory for values of $\beta \cot \Lambda$ less than 0.7. (See fig. 20.) For values of $\beta \cot \Lambda$ greater than 0.7, leading-edge bluntness results in a lift-curve slope below that predicted by linear theory but greater than that for sharp airfoils.

The characteristics of lift-curve slope presented in figure 19 were established by evaluating the experimental data at zero lift. To establish the extent of these linear lift characteristics, data were evaluated at an angle of attack of 20° and compared with the lift coefficients which result from an extrapolation of the experimentally determined lift-curve slope at an angle of attack of 20° . These results are presented in figure 21 as an increment in nonlinear lift as a function of the parameter $4\beta \cot^2 \Lambda$. The data clearly show that only for combinations of low Mach number and high leading-edge sweep (low aspect ratio) does nonlinear increasing lift occur (positive values of ΔC_L).

This observation was initially reported by Brown and Michael in 1954 (ref. 34), Squire, Jones, and Stanbrook in 1963 (ref. 10), and Squire in 1967 (ref. 35) and 1980 (ref. 36). However, with this present analysis, the bounds of this unique flow condition have been established. For values of the correlation parameter $4\beta \cot^2 \Lambda$ between 0.5 and 1.0, nonlinear lift effects are not present; for values of $4\beta \cot^2 \Lambda$ greater than 1.0, nonlinear decreasing lift occurs; and for values of $4\beta \cot^2 \Lambda$ less than 0.5, nonlinear increasing lift is found.

The maximum lift coefficient for thin delta wings plotted against the parameter M/A is presented in figure 22. The supersonic aerodynamics of delta wings at high angles of attack is presented to ensure a complete review of all pertinent aerodynamic characteristics. Possible applications of the data at these characteristics would be to canards or horizontal tails of aircraft and fins of missiles. An interesting point to note is that, despite the large range in $C_{L,\max}$ which was observed in the data ($1.1 \geq C_{L,\max} \geq 0.7$), all data showed that the maximum lift occurred at an angle of attack between 40° and 50° ; this indicates that $C_{L,\max}$ is dominated by the rotation of normal-force vector and not a function of flow conditions on the wing upper surface as is true at subsonic speeds. Experimental data at subsonic speeds show that wing upper surface flow separation or vortex breakdown has a large influence on $C_{L,\max}$. The data show that $C_{L,\max}$ varies from a maximum of 1.1 at a value of M/A of 0.05 to a minimum value of 0.7 at a value of M/A of 9.0; this indicates the effect of both Mach number and wing sweep. The combination of high supersonic Mach number and high wing sweep which is required to achieve large values of the correlation parameter (M/A) corresponds to wing flow conditions which would produce reduced values of $C_{L,\max}$. As an example, experimental data show that the contribution to the total lift coefficient from the wing windward side is only slightly dependent of wing sweep and Mach number at maximum

lift coefficient. However, the leeward-side contribution to the lift coefficient is greatly reduced with increases in both wing sweep and Mach number; these effects combine to produce the characteristics shown in figure 22. These individual wing upper and lower surface lift characteristics are discussed in more detail in the discussion of figures 27 through 38.

The longitudinal stability characteristics of uncambered delta wings, presented in figures 23 through 26, were determined by computing the slope across the zero-lift condition. The data have all been reduced about the two-thirds root-chord location, the linear-theory-predicted moment center. Presented in figure 23 is the longitudinal stability parameter $\beta(dC_m/dC_L)$ evaluated at zero lift plotted against the leading-edge sweep parameter $\beta \cot \Lambda$. Experimental data are presented for both sharp- and blunt-leading-edge wings with various leading-edge sweep angles and airfoil shapes over a wide range of Mach number. An examination of the data in figure 23 shows a gradual forward movement in the wing center of pressure when the wing leading-edge flow condition changes from subsonic to supersonic. For the subsonic leading-edge condition, all data show either neutral stability or positive stability, whereas for the supersonic leading-edge condition, all data show a negative stability level. As mentioned previously, these data were obtained at the zero-lift condition. To evaluate the extent of the linearity of these characteristics, the zero-lift dC_m/dC_L level was extrapolated to an angle of attack of 20° and compared with the measured experimental data at that angle of attack. Presented in figure 24 are the nonlinear increments in pitching moment evaluated at an angle of attack of 20° . The data show a trend with increasing $\beta \cot \Lambda$ which is opposite that for the stability data of figure 23. For $\beta \cot \Lambda$ less than 1.0, the data show a positive increment in pitching moment, and for $\beta \cot \Lambda$ greater than 1.0, the data show negligible increments in pitching moment. The data of figure 23 indicate that, for the subsonic leading-edge condition at zero lift, the majority of the data show that the wing stability level was approximated well by linear theory; however, as the wing is taken to an angle of attack, the data of figure 24 show the development of a nonlinear increment in pitching moment for the subsonic leading-edge condition, and this suggests the development of nonlinear flow over the wing.

The longitudinal stability characteristics are presented in figures 25(a) and 25(b) where the streamwise and spanwise wing centers of pressure on a single wing panel are presented for angles of attack of 5° and 50° , respectively. The data of figure 25(a)

show a variation in both the spanwise and streamwise center of pressure with changes in wing aspect ratio, whereas the data at an angle of attack of 50° (fig. 25(b)) collapse into a single curve. The variation in wing center of pressure can be directly related to the flow conditions about the wing. At low angles of attack, the lee-side flow characteristics for each wing vary considerably between attached and separated flow; however, as the wings are taken to $\alpha = 50^\circ$, the flow becomes quite similar and is characterized by two wing leading-edge vortices.

The lift and pitching-moment data presented have been shown to be dominated by wing leading-edge sweep effects. A review of the existing data base failed to uncover an adequate parametric set of wing data which could be used to isolate the effects of geometry and flow conditions on the drag-due-to-lift characteristic; therefore, the nonlinear computational method of reference 2 was employed for this analysis.

Nonlinear-predicted drag-due-to-lift characteristics for blunt airfoils are presented in figures 26 and 27. Also noted in each figure are the linear-theory zero-thrust and full-thrust boundaries. The nonlinear-theory method selected for this study is valid only for conditions of attached flow; as a result, nonlinear analysis was limited to blunt airfoils at conditions of low-to-moderate lift coefficients ($C_L \leq 0.3$). The effect of airfoil thickness, airfoil maximum thickness position, and airfoil bluntness on the drag-due-to-lift parameter has been studied for a delta wing with aspect ratio 1.0 at a Mach number of 1.41 (fig. 26). Results of the analysis show that increasing thickness, moving the maximum thickness location forward, or increasing airfoil bluntness improves the lifting efficiency of the airfoil, with airfoil thickness providing the largest improvement and bluntness the smallest. Comparison of the results shows that the nonlinear theory predicts a lower drag-due-to-lift parameter value than that predicted by linear theory for uncambered wings (no thrust), and for low values of the lift coefficient ($C_L < 0.1$), the nonlinear theory predicts drag characteristics below the linear-theory optimum (full thrust). The increase in the drag-due-to-lift parameter with increasing lift coefficient is a result of a loss in the aerodynamic thrust force as the wing rotates through a range of angles of attack. At low-lift conditions, the flow about the wing surface is characterized by a gradual expansion about the nose of the airfoil followed by a smooth recompression on the upper surface; this produces significant amounts of aerodynamic thrust. As angle of attack is increased, the local expansion about the airfoil nose increases significantly and extends over a greater portion of the airfoil leeward surface; this results in a

smaller percentage of the local expansion pressures acting on the nose of the airfoil. This expansion results in a reduction in the aerodynamic thrust force of the wing. The favorable flow conditions which exist about the nose of a blunt airfoil (low pressures) must coincide with favorable flow conditions over the aft section of the airfoil (high pressures) if an improvement in the drag-due-to-lift characteristics is to be realized.

The improvement in drag-due-to-lift characteristics with increasing airfoil bluntness is contradictory to the results of previous studies (ref. 37) in which complex wing geometries were employed in the study of the leading-edge thrust phenomenon. However, as discussed, the variation in drag due to lift is not solely dependent upon the loading at the leading edge of the wing, but it is dependent upon the total wing loading. The nonlinear analysis presented in figure 26 was performed at conditions which were previously determined to have a subcritical-type flow structure over the wing ($\beta \cot \Lambda = 0.25$); however, the drag-due-to-lift analysis showed a highly nonlinear characteristic. To investigate these effects further, nonlinear analysis was performed on both a delta wing with $A = 1.0$ and one with $A = 2.0$ with blunt modified four-digit-series airfoils ($\tau = 0.40$, $m = 0.5$, and $R = 4.0$). Analysis was conducted for values of $\beta \cot \Lambda$ from 0.25 to 0.8. Results of this analysis are presented in figure 27 in which curves of constant lift coefficient for both wings are shown. Also presented in the figure are the linear-theory zero-thrust and linear-theory full-thrust curves of the drag-due-to-lift parameter. The nonlinear analyses show an increase in the drag-due-to-lift parameter with increasing lift coefficient, decreasing $\beta \cot \Lambda$, and decreasing aspect ratio. Results for the wing with $A = 1.0$ at $C_L = 0.1$ show a variation in the aerodynamic thrust from 70 percent of the full-thrust linear-theory value at $\beta \cot \Lambda = 0.25$ to 0 percent at $\beta \cot \Lambda = 0.75$. The drag-due-to-lift parameter for the wing with $A = 2.0$ at $C_L = 0.1$ varied from 114 percent to 100 percent at $\beta \cot \Lambda = 0.25$ to 0.75. Similar characteristics to those observed at $C_L = 0.1$ were also observed for the two wings at $C_L = 0.2$. An increase in drag due to lift with decreasing wing aspect ratio would normally be expected for a constant Mach number; however, by presenting the data with respect to $\beta \cot \Lambda$, wing leading-edge sweep or aspect ratio effects should be factored out of the solution. As a result, the analyses suggest that Mach number has a large impact on the aerodynamic performance of a given wing. As Mach number is reduced, the characteristics around the wing change dramatically; the upper surface leading-edge suction pressure coefficients become more negative and the lower surface

leading-edge pressure reduces slightly to increase the aerodynamic thrust force. In addition, the thrust force which is produced normal to the wing leading edge varies as the cosine of the leading-edge sweep angle. As aspect ratio is increased the wing sweep decreases to increase the aerodynamic thrust force. In general, the character of all the curves presented in the figure is a rapid reduction in the drag-due-to-lift parameter (increased performance) with increasing $\beta \cot \Lambda$ up to a value of approximately 0.6. For values of $\beta \cot \Lambda$ greater than 0.6, the curves tend to flatten out. This characteristic seems to be quite sensitive to aspect ratio and lift coefficient; however, a value of $\beta \cot \Lambda$ of 0.6 seems to be a representative mean value for the analysis conducted.

The previous analysis reviewed the aerodynamic forces and moments of flat delta wings at lifting conditions in which the lift and pitching-moment characteristics were shown to be dominated by the flow condition at the wing leading edge ($\beta \cot \Lambda$) and the drag to be equally sensitive to all geometric and flow parameters. To provide further insight into these observed characteristics for flat delta wings, wing upper and lower surface static-pressure distributions are reviewed. The experimental pressure data are reviewed to investigate the effects of wing leading-edge sweep, leading-edge bluntness, wing thickness, wing camber, Mach number, and angle of attack on the total wing loading and the individual upper surface and lower surface wing loadings. This study makes use of the known existence of conical flow for conical geometries at supersonic speeds to extend the use of the limited amount of wing surface pressures in an effort to represent the total wing loading. However, before this analysis can be generally applied, the lower Mach number bounds of the supersonic flow regime need to be identified in order to determine where the conical flow assumption may be used. In order to determine the lower Mach number bound of the supersonic flow regime, subsonic and transonic data need to be reviewed to ensure that the characteristics of these two flow fields are differentiated from those at supersonic speeds. Presented in figure 28 are spanwise pressure distributions at various longitudinal (x/c_r) stations for a delta wing with $A = 1.0$ at Mach numbers from 0.60 to 3.50. The pressure data clearly show that nonconical flow conditions exist at both $M = 0.60$ and 0.90. However, between $M = 0.90$ and 1.20, the pressure data change from a nonconical nature to a very nearly conical flow on both the upper and lower surfaces. At a Mach number of 1.60, the spanwise pressure distributions are conical and remain conical for all further increases in Mach number. Based upon these data, a minimum supersonic Mach number is defined as approximately 1.20. An

interesting point to note is the dramatic change in the upper surface pressures and the comparative insensitive nature of the lower surface pressures with increasing supersonic Mach number. These effects are discussed further in the discussion of figure 29.

Typical effects of Mach number and angle of attack on the spanwise pressure distribution for a delta wing with $A = 1.0$ are presented in figures 29 and 30, respectively. To assist in the discussion of the pressure data only a single pressure distribution is presented in figures 29 and 30. In addition, the data of figures 29 and 30 are used to represent the total wing pressure distribution (conical flow).

If the assumption is made that conical flow exists, then the data presented in figure 29 show that, at a constant angle of attack of 15° , increasing the Mach number from 0.6 results in an ever increasing reduction in upper surface normal-force coefficient. A reversal of these upper surface effects is found on the lower surface where the lower surface normal-force coefficient increases with an increase in Mach number as the transition is made to supersonic speeds and then remains constant. As Mach number increases, the increase in lower surface lift coefficient does not completely compensate for the reduction in upper surface lift, and the result is a reduction in total wing lift coefficient with increasing Mach number at a constant angle of attack. The combination of a reduction in the upper surface lift coefficient with an increase in lower surface lift coefficient highlights the impact of compressibility and the vacuum pressure coefficient at supersonic speeds.

Presented in figure 30 is the effect of increasing angle of attack on the spanwise pressure distribution at $M = 0.60$, 0.90 , 1.20 , and 1.60 for the delta wing with $A = 1.0$. The pressure data show that at $M = 0.60$ and 0.90 , both the upper and lower surface lift increase proportionally. The data for $M = 1.20$ and for $M = 1.60$ indicate a shift in the percentage of lift force from the upper surface to the lower surface. This effect is quantified in figure 31 which depicts the percentage of lift on both the upper and lower surfaces for angles of attack of 10° and 20° . The graph of figure 31 shows that at subsonic speeds ($M = 0.60$ and 0.90), approximately 70 percent of the total lift comes from the upper surface, independent of angle of attack. At $M = 1.20$ and $\alpha = 10^\circ$, the upper surface carries 70 percent of the lift, but at $\alpha = 20^\circ$, this is reduced to 60 percent. This trend is also observed at $M = 1.60$ where at $\alpha = 10^\circ$ the upper surface dominates with 56 percent of the lift and at $\alpha = 20^\circ$ it has been reduced to 48 percent of the lift. The shifting of lift from the upper to the lower surface with increasing angle of attack at

supersonic speeds is a combination of nonlinearly decreasing upper surface normal force and nonlinearly increasing lower surface normal force. These results suggest that only at subsonic speeds ($M \leq 0.90$) can the lift increment between the linear potential-theory solution and experimental data belong solely to upper surface vortex-induced effects. At both transonic and supersonic speeds, the lift increment is probably due to a combination of both nonlinear lower surface and nonlinear upper surface effects. In particular, at supersonic speeds, the upper surface vortex-induced lift increment reduces with increasing angle of attack, and the lower surface compression lift increment increases with increasing angle of attack.

At both subsonic and supersonic speeds, the lift-curve slope and lifting efficiency of a wing are directly related to the aspect ratio of the wing. To determine the effect of aspect ratio on the distribution of lift between the upper and lower surface of a wing, the analysis presented in figures 30 and 31 was repeated for a wing with $A = 0.5$ ($\Lambda = 82.87^\circ$) and one with $A = 2.0$ ($\Lambda = 63.43^\circ$). Presented in figure 32 are spanwise surface pressure distributions for wings with $A = 0.5$, 1.0 , and 2.0 at angles of attack of 10° and 20° for $M = 0.60$ and 1.60 . Comparison of the upper and lower surface pressure plots in figure 32 shows that the supersonic data vary in a more orderly fashion with increases in aspect ratio. The data at both $M = 0.60$ and 1.60 show an increase in lift with increasing aspect ratio, with the upper surface dominating at subsonic speeds, but a more equal distribution is evident at supersonic speeds. These effects are quantified in figure 33 in which the percentage of lift on the upper and lower surfaces is depicted. The graph shows that Mach number has the largest impact on the distribution of lift for all wings at angles of attack of 10° and 20° . All wings show a shifting of lift from the upper surface to the lower surface with increasing angle of attack except for the wing with $A = 0.5$ at $M = 1.60$, which shows a reverse effect. The combination of low aspect ratio and low free-stream Mach number creates conditions favorable to the development of nonlinear lift effects. (See fig. 21.) These conditions combine to give a value of the nonlinear lift correlation parameter ($4\beta \cot^2 \Lambda$) of 0.08, which is a condition at which large amounts of nonlinear lift would occur. Based upon the data in figure 33 it may be concluded that this increment can be attributed to the wing upper surface flow field. A comparison of the wings with $A = 1.0$ and 2.0 at $M = 1.60$ shows a gradual increase in lower surface dominance with increasing wing aspect ratio at both angles of attack. The pressure data of figure 32 show that this transition in lift force is primarily due to an increase in the lower

surface contribution to the normal force and not due to upper surface effects.

A summary of the individual normal-force characteristics of the upper and lower surfaces for thin delta wings is presented in figures 34, 35, and 36. Figures 34 and 36 are formulated by integrating experimental spanwise pressure distributions to extract sectional upper and lower surface normal-force coefficients. The sectional normal-force coefficients are then used to represent the total wing upper or lower surface normal-force coefficient based upon the known existence of conical flow for delta wings at supersonic speeds. The curves of figures 34, 35, and 36 cover a range of Mach number from 1.50 to 3.50 and leading-edge sweep of 52° to 85° . The results could not be produced for Mach numbers below 1.50 because of insufficient experimental data. As shown in figure 34, when the upper surface normal-force coefficient C_N^u is plotted as a function of the parameter $\alpha_N \beta \cot \Lambda$, the data collapse into a family of constant Mach number curves. The large effect of Mach number on upper surface normal force is clearly shown; for example, an increase in Mach number from 1.50 to 2.00 (fig. 34(b)) reduces the upper surface lifting potential by 50 percent at a given value of the correlation parameter. The large reduction in upper surface lifting capability with increasing Mach number is due to the inability to achieve low values of the upper surface suction pressure coefficient. The characteristics of the data of figure 34 also indicate that, for a given Mach number and leading-edge sweep, an increase in angle of attack results in an upper surface normal-force coefficient that increases nonlinearly with a decreasing slope.

Presented in figure 35 is the upper surface minimum pressure coefficient $C_{p,\min}^u$ plotted as a function of the parameter $\alpha_N \beta \cot \Lambda$. These data also collapse into a family of constant Mach number curves. Also noted in this figure is the percent of vacuum limit which was attained for that particular Mach number. The data show that the percent of the vacuum pressure actually attained is reduced with increasing Mach number. At a Mach number of 3.50 (fig. 35(a)), only 75 percent of the vacuum limit pressure coefficient was reached; however, at a Mach number of 1.50, 97 percent of the vacuum limit pressure coefficient was attained (fig. 35(b)).

The variation in the lower surface normal-force coefficient is presented in figure 36. Unlike the data of figures 34 and 35, which showed that the upper surface characteristics are a function of leading-edge sweep, Mach number, and angle of attack, the lower surface characteristics were found to be predominantly a function of leading-edge sweep and angle

of attack. The lower surface normal-force coefficient C_N^ℓ is plotted as a function of the normal angle of attack α_N and the data collapse into a family of constant leading-edge sweep curves. Each of these curves is comprised for a range of Mach numbers, with the only limitation being that the normal Mach number M_N of all these data be less than 1.00. However, the data have a maximum variation with Mach number of approximately $\pm 0.03 C_N$. The data show that the lower surface produces a nonlinearly increasing normal-force increment with increasing angle of attack, and it can be seen that the nonlinearity increases with an increase in leading-edge sweep.

An evaluation of the data of figures 34 and 36 supports the findings previously observed in figures 21 and 33, which indicate that nonlinear lift is most pronounced for extremely highly swept wings at low Mach numbers. For these very low values of the parameter $\beta \cot \Lambda$, the highly nonlinear character of the lower surface normal-force coefficient adds to the linear character of the upper surface normal-force coefficient and produces a total lift force which increases in a nonlinear sense. Similarly, figures 34 and 36 can be used to show that the reduction in lift-curve slope with an increase in leading-edge sweep is primarily a lower surface-dominated effect and the increase in lift-curve slope with a decrease in Mach number is an upper surface-dominated effect.

To further extend these findings, the effects associated with varying leading-edge bluntness and Reynolds number (N_{Re}) on the minimum upper surface pressure are presented in figures 37 and 38, respectively. The data for $C_{p,\min}^u$ are plotted as a function of the parameter $\alpha_N \beta \cot \Lambda$ for flat wings at conditions in which the flow has separated at the leading edge. A summary of the effect of leading-edge bluntness on $C_{p,\min}^u$ is presented in figure 37(a) in which curves are presented for both sharp and blunt leading-edge wings at Mach numbers of approximately 1.50, 1.60, 1.90, and 2.40. The blunt leading-edge curves were taken from figures 37(b) and 37(c), and the sharp leading-edge data curves were taken from figure 35. The data show that leading-edge bluntness increases the minimum upper surface pressure coefficient for a given value of $\alpha_N \beta \cot \Lambda$ but does not affect the minimum value of $C_{p,\min}^u$. The increased upper surface suction pressures with leading-edge bluntness would be expected to increase the lift-curve slope and allow for the development of a given level of lift at a lower wing incidence angle, and, thus, result in lower drag. These results are directly reflected in the data of figure 19 where the lift-curve slope is shown to increase over that for a sharp wing with the addition of leading-edge bluntness.

The data of figure 38 show that at a constant Mach number increasing N_{Re} for a blunt leading-edge wing increases the minimum upper surface pressure coefficient for a given value of $\alpha_N \beta \cot \Lambda$; however, these effects decrease with an increase in Mach number.

These data show that at supersonic speeds significant amounts of nonlinear flow exist on flat, sharp-leading-edge delta wings, and that the nonlinear characteristics of delta wings are affected by leading-edge bluntness and Reynolds number. These nonlinear characteristics which occur on both the upper and lower surfaces of flat wings are summarized in the form of graphs to provide a fundamental understanding of the aerodynamics of delta wings to the designer.

Thickness effects. The figures discussed in the previous section, which summarized the global and local aerodynamics of flat delta wings, relied heavily on the known existence of conical flow for their development. The figures were constructed from data sets obtained with zero-thick delta wings (conical geometries) or very slender geometries which are near conical in nature. In order to study similar aerodynamic effects for typical wing thickness variations, it would be necessary to have an extensive amount of upper surface and lower surface pressure distributions in order to resolve the nonconical flow conditions. However, if the thick-wing geometry is conical, the flow may be assumed to be conical and a single spanwise pressure distribution is all that is required on both the wing upper surface and lower surface to represent the total wing flow field.

In an attempt to assess the effect of leading-edge angle, a comparison is made between the 30° diamond wing and the 60° biconvex wing. In an attempt to assess thickness effects, a comparison is made between the 30° biconvex wing and the 30° diamond wing. Presented in figures 39 through 48 are the effects of thickness on the total wing aerodynamics and the local wing loadings for several conical geometries. The thick-wing data were obtained from reference 23 in which three delta wings with $A = 1.0$ differing in thickness and cross-section shape were tested between $M = 1.30$ and 2.80 . As shown in the inset sketch of figure 39, the three different thicknesses correspond to a diamond cross section with a 30° leading-edge half-angle, measured in the cross-flow plane, and two biconvex cross sections with 30° and 60° leading-edge half-angles, also measured in the cross-flow plane. It is recognized that these cross sections do not form typical airfoil shapes; however, they probably represent reasonable upper bounds on airfoil leading-edge angles and airfoil thicknesses.

The effect of wing thickness on the wing leading-edge vortex position is presented in figure 39. The zero-thickness flat-wing curve shown in the figure has been taken from the flat-wing data of reference 31. The data clearly show an outward movement of the vortex with increasing leading-edge slope at all conditions evaluated. The thick-wing data show that the wing leading-edge angle acts to delay the onset of flow separation to a higher angle of attack. For a constant angle of attack, the data show a weaker vortex which is located more outboard compared with the flat-wing data (fig. 42). A comparison of the data for the two wings with a 30° leading-edge sweep angle shows a slight shift in the vortex position due to thickness. The data indicate that wing leading-edge angle and not wing thickness is the dominant mechanism which controls vortex formation, strength, and position. Despite these large effects on the lee-side flow characteristics between the three wings, there were no noticeable changes on the total wing lifting characteristics. (See fig. 40.) For values of $\beta \cot \Lambda$ below 0.5, the lift-curve-slope data show an insensitivity to thickness; for values of $\beta \cot \Lambda$ above 0.5, the data show an increase over the flat delta data but yet show no variation between the three thick wings. The lift-curve-slope data were evaluated between $\alpha = 0.0^\circ$ and 2.05° in which the flow is attached and both surfaces have positive pressure coefficients. (See fig. 44.) The lift curve of these thick wings was found to be quite different from that of the flat wings. In particular, the linearity of the lift curve for all wings was found to be limited to a few degrees angle of attack. Moreover, the data of figure 41 show that the bounds established for the development of nonlinear lift for thin flat wings are not applicable to thick wings because significant amounts of nonlinear lift are evident well within the flat-wing linear lift region. An examination of the surface pressure coefficient data indicated that the increased lift effect may be attributed to the wing upper surface. At zero lift the thick-wing upper surface has large positive pressures, and as we have already seen from the flat-wing data, there is a minimum upper surface pressure which may be attained at a given Mach number. The differences between these two pressure levels define the maximum attainable upper surface wing loading. If we compare this value to that for a zero-thick or flat wing, at zero lift the flat wing has a pressure coefficient value of approximately 0.0 compared with a value of 0.05 to 0.10 for the thick wing. (See fig. 44.) This difference would reduce the allowable change in upper surface pressure coefficient for the flat wing and, thus, the resultant wing lifting potential. These effects are quantified in figures 42

through 44 for changes in thickness, Mach number, and angle of attack.

The lower surface pressures show an equal effect of both the wing leading-edge angle and wing thickness. Mach number effects are shown in figure 43 for the 30° biconvex wing geometry at an angle of attack of 8°. The data show trends similar to those observed for the flat delta wings, a reduced upper surface loading with increased Mach number, and a general insensitivity to Mach number on the lower surface. A comparison of the thick-wing lower surface data with the flat-wing data (fig. 29) shows a reversed variation with increasing Mach number. The flat-wing data indicate a slight increase in lower surface pressure with increasing Mach number whereas the thick-wing data show a decrease in pressure. This pressure reduction is actually misleading, because the pressure data at an angle of attack of 0° also show a pressure reduction with increased Mach number, which occurs at a rate equal to that observed at angle of attack; this results in an invariant lower surface loading.

Presented in figure 44 is the effect of angle of attack on the spanwise pressures for the 30° biconvex geometry at $M = 1.30$. The data show trends similar to those for the flat wings; however, the levels are quite different especially at an angle of attack of 0°. As mentioned previously, the positive upper surface pressure coefficient at $\alpha = 0^\circ$ for the thick wings allows for a greater increment in upper surface loading with increased angle of attack. In particular, the data show an average pressure coefficient of 0.075 at an angle of attack of 0°, which is approximately 9 percent of the maximum flat-wing upper surface lift force, with total vacuum pressure coefficient on the wing upper surface being assumed.

The distribution of loading between the upper and lower surfaces of the 30° biconvex wing at $\alpha = 8^\circ$ and 16° for Mach numbers of 1.30, 2.00, and 2.80 is shown in figure 45. The data show a gradual shifting in lift from the upper surface to the lower surface with increasing Mach number and angle of attack. If the thick-wing results of figure 45 are compared with the flat-wing data of figures 29 through 31, we see a delay of the dominance of the lower surface on the total lift with increasing Mach number.

A summary of the individual normal-force characteristics of the upper and lower surfaces for the three thick delta wings is presented in figures 46, 47, and 48. Figures 46 and 48 were formulated in the same manner as those for the flat wings. Thick-wing upper surface normal-force data are presented in figure 46 along with the flat-wing curves from figure 34 for Mach numbers 1.30, 2.00, and 2.80. The thick-wing data collapse into three groups of

constant Mach number in which the data agree reasonably well over the range of the correlation parameter $\alpha_N \beta \cot \Lambda$. At low values of the correlation parameter, the thick-wing results fall below the flat-wing curves, and as the correlation parameter is increased the thick-wing data increase more rapidly and eventually cross over the flat-wing curves. The nonlinearity in the thick-wing data curves can be attributed to the large positive pressure coefficients which exist at $\alpha = 0^\circ$. Despite these differences between the two data sets, some of the general trends of the thick wings agree reasonably well with the flat-wing results.

The effect of the pressure at $\alpha = 0^\circ$ is highlighted in figure 47, which presents the upper surface minimum pressure coefficient at $M = 1.30$, 2.00, and 2.80. The data show a significant delay in the occurrence of a negative pressure coefficient due to increased thickness and leading-edge slope. This effect is most evident for the data at $M = 1.30$ where there is a 0.25 variation in the minimum pressure coefficient between the three wings at an angle of attack of 12°.

The effect of thickness on the lower surface normal-force coefficient compares well to the flat-wing results of figure 36 (fig. 48); this indicates that lower surface normal-force characteristics are independent of wing thickness and Mach number.

Camber effects. In designing a wing for efficient supersonic flight, the geometric parameter which is usually optimized after the wing planform selection is the camber and twist distribution. The purpose of this section is to evaluate the following: the wing lift-curve slope sensitivity to camber, the effect of aspect ratio on nonlinearities in the flow, and the lift distribution between the upper and lower surfaces relative to that for a flat wing. These points were addressed by analyzing a parametric set of six conical, zero-thickness, cambered delta wings tested at $M = 1.90$. The geometries consisted of 15° streamwise leading-edge deflections of the outboard 10 percent and 20 percent of the semispan for each of the three leading-edge sweep angles of 75°, 67.5°, and 58.25° (ref. 24). These wings were used to evaluate the effect of camber only, since no twist was applied to the spanwise sections. The data are presented in a similar fashion as those for thickness effects in figures 49 through 57.

Unlike the thick-wing data which showed a uniform progression in the location of the vortex with all parameters, the cambered wing data were very erratic (fig. 49). A review of the pressure data revealed that the lee-side flow characteristics were quite complex due to the sudden expansion about camber

hinge line. (See figs. 52, 53, and 54.) However, once flow separation occurs at the wing leading edge ($\alpha > 10^\circ$), the flow behaves similar to that for the thin flat wings. The data also show that increasing wing camber delays the formation of a wing leading-edge vortex. These results are analogous to the effect of increasing the leading-edge sweep angle for thick wings. However despite these flow complexities the agreement between the flat-wing and cambered-wing lift-curve slopes was quite surprising (fig. 50). The cambered-wing data show a variation in lift-curve slope similar to that observed for thick wings with an increased lift-curve slope for $\beta \cot \Lambda$ greater than 0.5. This increased lifting efficiency at the higher values of $\beta \cot \Lambda$ may be attributed to the increased loading potential of the wing leading edge. The cambered wing at an angle of attack of 0° would have a large negative load on the deflected portion of the wing leading edge. The magnitude of this load at $\alpha = 0^\circ$ would be equivalent to the additional lift increment available to the cambered wing compared with the flat wing. This effect is supported by the comparison of flat and cambered nonlinear lift increments which show the existence of nonlinear lift for all values of the correlation parameter (fig. 51). To further evaluate the local aerodynamics of cambered delta wings, detailed upper and lower surface pressure coefficient (at $x/c_r \approx 0.66$) distributions highlighting the individual effects of camber, leading-edge sweep, and angle of attack are presented in figures 52, 53, and 54, respectively.

The effect of camber on the spanwise surface pressure distributions is presented in figure 52 for the 75° swept wing at an angle of attack of 8° . A significant variation in the leading-edge upper surface pressures is evident due to increasing camber; however, the loadings are equivalent. On the lower surface the spanwise pressure distributions show less sensitivity to camber.

Presented in figure 53 is the effect of leading-edge sweep on the spanwise pressure distributions at an angle of attack of 8° . The data show that the major influence of leading-edge sweep is an increase in the lower surface loading with decreasing sweep; this also correlates well with the flat-wing data of figure 32(b). There is also a significant influence on the position of the vortex.

The variation in the spanwise surface pressure distributions with angle of attack for cambered wings is presented in figure 54. The data clearly show the loading at the wing leading edge for an angle of attack of 0° , which was alluded to earlier. The integrated lift increment between the upper and lower surface spanwise pressure distributions at $\alpha = 0^\circ$ provides an additional increment in lift to the wing similar to

that observed for the thick wings. Also evident are the large hinge-line-induced expansion pressures on the wing upper surface ($\alpha = 8^\circ$) and the oscillatory nature of the lower surface pressure due to the irregular geometry. As with the thick wings, an integration of the pressures to obtain the upper and lower surface wing loadings resulted in values comparable with those for the flat wings (figs. 55 and 57).

The upper surface normal-force data for all cambered wings are presented in figure 55. The data are shown to collect near or below the flat-wing data at $M = 1.90$ from figure 34 (solid line) and show little effect of leading-edge sweep or camber. Presented in figure 56 are the upper surface minimum pressure coefficients for all cambered wings. The data fall into a broad band which lies below and parallel to the flat-wing data. This large scatter of the $C_{p,\min}^u$ data can be attributed to the interaction between the hinge-line expansion and the leading-edge separation and produces both a wide range and a dramatic change in the lee-side flow with changes in camber, wing sweep, and angle of attack. The effect of camber on the lower surface normal-force coefficient is presented in figure 57. The lower surface characteristics are shown to separate according to the wing leading-edge sweep as indicated by the flat-wing data (solid line), and the data show little effect of camber. A comparison of the two data sets seems to indicate a reduction in the lower surface normal force due to camber; however, the cambered delta wings of reference 24 were constructed by a deflection of the outboard segment of the reference flat wing. This would result in leading-edge sweep angles for the cambered wings which are greater than those listed.

Comments on lifting characteristics. The aerodynamic characteristics of delta wings at lifting conditions have been evaluated for the effects of wing leading-edge sweep, leading-edge bluntness, and wing thickness and camber and then summarized in the form of graphs which may be used to represent the aerodynamic characteristics of delta wings. Empirical correlation curves derived from experimental data have been developed for the lift-curve slopes, nonlinear lift effects, maximum lift, longitudinal stability, and distribution of lift between the upper and lower surfaces of a wing. However, the impact of airfoil thickness, maximum thickness position, leading-edge bluntness, wing leading-edge sweep, and lift coefficient on the drag and the drag-due-to-lift characteristics is shown theoretically.

Real-Flow Wing Design

Wing design studies at supersonic speeds have typically been prefaced with the terms "linear" or

"nonlinear" depending upon the theoretical method which was employed within the investigation. In addition, the previous nonlinear studies have employed traditional linear-theory rules in planform and airfoil selection. Previous supersonic wing design studies have also typically employed airfoils with thicknesses between 3 and 6 percent and the maximum thickness located at 40 percent to 50 percent chord. The aerodynamic reasoning for selecting or limiting the selection of wing geometries to these geometries has never been documented. In fact, linear-theory aerodynamic graphs which are typically used in preliminary design indicate that significant drag reductions may be attained with alternate airfoil shapes. (See fig. 6.) The intent of this section of the paper is to employ the empirically derived graphs of the previous sections in a systematic fashion to select wing geometric characteristics conducive to high levels of aerodynamic performance.

The zero-lift, low-lift, and high-lift aerodynamic characteristics previously presented for delta wings show a large influence due to changes in wing geometry and flow conditions. At zero lift, theoretical analysis with an inviscid nonlinear method shows significant variations from the standard linear-theory curves due to changes in airfoil shape, airfoil thickness, leading-edge bluntness, and wing leading-edge sweep. A review of the zero-lift-curve drag analysis shows that for a cruise or low-lift-dominated design the diamond airfoil could provide 20-percent to 50-percent reductions in wave drag compared with the NACA modified four-digit-series airfoil. However, if the wing is to operate over a range of Mach number and lift coefficient the problem becomes more complex and a blunt airfoil should be employed to improve the drag-due-to-lift characteristics. The zero-lift wave-drag analysis for the NACA modified four-digit-series airfoil (fig. 13) shows that for values of $\beta \cot \Lambda$ between 0.6 and 0.8 locating the airfoil maximum thickness at the 20-percent chord provides low drag, and the analysis presented in figure 26 shows an improvement in the drag-due-to-lift characteristics for the same geometry. The design of a wing within this range of $\beta \cot \Lambda$ would provide the opportunity to achieve good aerodynamic performance.

A review of the lift-curve-slope data of figure 20 and the computed drag-due-to-lift results of figure 27 supports the range of $\beta \cot \Lambda$ from 0.6 to 0.8 as a feasible design region. The data of figure 20 show that at a value of $\beta \cot \Lambda$ of 0.6 the data for the sharp leading-edge wings level off and at a value of $\beta \cot \Lambda$ of 0.8 the same occurs for the blunt leading-edge data. For flat wings, the lift-curve slope is inversely proportional to the drag-due-to-lift characteristics; therefore, a leveling off of the lift efficiency should

indicate the point of optimum performance. However, the data of figure 27 show that the drag-due-to-lift characteristics are much more complex. Whereas the data of figure 20 showed no distinguishable effects of aspect ratio, the drag data show large variations in performance due to both wing sweep and lift coefficient. The data show that the value of $\beta \cot \Lambda$ at which the drag-due-to-lift characteristics reach a minimum varies between 0.4 and 0.8 depending upon lift coefficient and aspect ratio. A review of the zero-lift wave-drag data (fig. 13) shows that a value of $\beta \cot \Lambda$ of 0.4 corresponds to the bucket of the curve for $m = 0.2$; as a result, the design space is expanded to values of $\beta \cot \Lambda$ between 0.4 and 0.8 for completeness.

The typical application of thickness to uncambered delta wing results in a geometry which is conical about the wing tip. This classical application of thickness to a swept wing is no doubt less than optimum for supersonic flight. Experimental data (ref. 38) and theoretical analysis (ref. 2) show that the flow over a swept wing at supersonic speeds tends to be conical about the wing apex and not conical about the wing tip as observed in subsonic flow for unswept wings. The conical nature of the flow field over the wing produces favorable and unfavorable pressure fields on the wing surface. For a wing at lift, the flow over the wing upper surface would be characterized by an expansion over the leading edge which is followed by a recompression to a more positive pressure as the flow moves inboard. The location of the recompression has been observed to lie along a ray emanating from the wing apex, independent of the wing geometry. If the upper surface is divided into four quadrants, defined by the intersection of the airfoil maximum thickness line and the recompression line, two favorable and two unfavorable performance regions may be identified. The two unfavorable regions, which contribute to the drag, are the inboard forward portion and the outboard aft portion of the wing. The inboard forward portion of the wing experiences a recompression of the flow prior to the airfoil maximum thickness line; this results in more positive pressures acting on a forward-facing wing surface. On the other hand, the outboard aft portion of the wing is characterized by a rearward-sloping surface which combines with the high negative pressure coefficients to produce high drag levels. The other two quadrants of the wing upper surface would have pressure fields which combine favorably with the local surface geometry to produce drag reductions. These observations suggest that improved supersonic performance could be achieved if the wing designer configures the wing geometry to take advantage of the natural conical flow structure

against it. Future supersonic wing designs should break from tradition and begin to explore new airfoil shapes and distributions of airfoils, such as increasing leading-edge bluntness, airfoil maximum thickness, and airfoil maximum thickness position with increasing spanwise position to take full advantage of the conical nature of the flow.

To define a high-lift ($0.2 \leq C_L \leq 0.4$) wing design philosophy, an understanding of the flow limitations which exist is required. At these high-lift conditions, the flow will undoubtedly separate at the leading edge for an uncambered subsonic leading-edge wing independent of airfoil shape. The lee-side flow condition which would exist for delta wings at angle of attack is shown in figure 17. The data of figure 17 clearly show that within the feasible range of values of $\beta \cot \Lambda$ identified for low lift ($0.4 \leq \beta \cot \Lambda \leq 0.8$), $M_N < 1.00$, the lee-side flow is characterized by a leading-edge separation. By limiting the high-lift design to separated flows and by imposing the minimum supersonic Mach number identified in figure 28 and an arbitrary selection of $\Lambda = 75^\circ$ as the maximum sweep angle, the M_N and α_N space can be reduced significantly. (See fig. 58.) The primary premise on which the high-lift wing design concept is to be based is the assumption that the lift force on the wing upper surface must be equal to or greater than the lift force on the lower surface. The supporting argument for these criteria is that the negative pressure coefficients acting on the upper surface at the leading edge of the wing are the primary mechanism for creating aerodynamic thrust; thus, if the upper surface of the wing does not produce at least 50 percent of the lift, then significant drag reductions may not be realized. In order to satisfy these conditions, delta wing upper surface and lower surface normal-force coefficient design graphs have been developed from the data of figures 34 and 36 (figs. 59 and 60). The upper surface normal-force coefficient characteristics are strongly dependent on Mach number; for example, an increase in Mach number from 1.50 to 2.00 reduces the upper surface normal-force coefficient by 50 percent. In a similar manner the lower surface normal-force coefficient is a strong function of leading-edge sweep. Additional data show that both the upper surface and lower surface normal-force coefficients of delta wings are not significantly influenced by thickness or camber; thus, the application of these graphs to the development of a high-lift wing design space for delta wing geometries should be acceptable.

By imposing a design C_N value and requiring that the design C_N can be distributed between the upper and lower wing surfaces such that the upper surface normal-force coefficient always equals or exceeds the

lower surface normal-force coefficient ($C_N^u \geq C_N^\ell$), the data presented in figures 59 and 60 can be used in an iterative sense to define a feasible high-lift separated-flow design space. To assist in the iteration process, plots of M_N and α_N against α are presented in figure 61. Presented in figure 62 is a matrix of points, identified by their associated Mach number and leading-edge sweep values, that satisfy the distributive normal-force coefficient relationship ($C_N^u \geq C_N^\ell$) for a design condition of $C_N \approx 0.40$. Each of these points in the matrix was determined by iterating through figures 59 and 60 until the distributive requirement was satisfied. A sample design iteration for $C_N = 0.4$ and $\Lambda = 75^\circ$ is initiated by determining the α_N at which $C_N^\ell = 0.2$ and then through trial and error the maximum Mach number is determined at which $C_N^u = 0.2$. Once α_N and M are known, the graphs in figure 61 can be used to compute M_N for plotting in figure 62. The matrix of feasible solutions presented in figure 62 can be thought of in terms of lines of constant Mach number (solid lines) in which both α and Λ vary and lines of constant leading-edge sweep (dashed lines) in which only M varies. The boundaries of a given design space are defined on the right by the maximum wing leading-edge sweep under consideration, on the bottom by the minimum Mach number, and on the left by the minimum allowable wing leading-edge sweep under consideration. The upper boundary is defined by iterating through the design process to determine the maximum Mach number for which a given wing geometry (leading-edge sweep) satisfies the distributive requirement. Shown in figure 62 are the maximum Mach numbers for several leading-edge sweep conditions.

Presented in figure 63 is the design space for design values of C_N of 0.40 and 0.20. The data indicate that a reduction in the design value of C_N expands the range of feasible solutions and shifts it to a lower value of α_N and M_N . A decrease in design C_N allows for the extension to higher Mach numbers. The apparent reduction in the size of the design space with reduced design C_N is strictly graphical in nature due to the nonlinearly decreasing relationship between α and α_N . The design-space concept for moderate-to-high-lift conditions ($0.2 \leq C_L \leq 0.4$) was evaluated with data from previous supersonic wing designs (ref. 39). The study showed that designs conducted for conditions which lie within the appropriate design space had lower drag due to lift compared with those outside the design space.

To further evaluate the design-space concept and to relate the high-lift requirements to the low-lift requirements, lines of constant values of $\beta \cot \Lambda$

of 0.4, 0.6, and 0.8 are presented in each plot. The value of α_N for each point in figure 63 corresponds to the value of α_N at which C_N^ℓ equals 50 percent of the total design C_N value for each wing sweep. The value of M_N was then determined by iterating through figure 61(a) for the particular value of $\beta \cot \Lambda$. The graphs show that decreasing both $\beta \cot \Lambda$ and the design C_N expands the design matrix. For the design C_N of 0.4, decreasing $\beta \cot \Lambda$ from 0.8 to 0.6 and 0.4 increases the maximum wing leading-edge sweep for designs from 55° to 65° and to a value greater than 75° , respectively. Similarly decreasing design C_N to 0.2 increases the maximum wing leading-edge sweep from 55° to 60° for a design at a value of $\beta \cot \Lambda$ of 0.8. These results have been summarized in figure 64 in which the limiting sweep angle for a delta wing has been plotted against the leading-edge sweep parameter $\beta \cot \Lambda$ for design values of C_N of 0.2 and 0.4. This graph clearly shows the dominance that the $\beta \cot \Lambda$ condition has on the ability to produce efficient lifting conditions required for high-lift wing design.

If the high-lift design trade data of figure 64 are combined with the zero-lift data of figure 13 and the low-lift data of figures 20 and 27, it may be concluded that a value of $\beta \cot \Lambda$ of approximately 0.6 composed of $\Lambda = 65^\circ$ and $M = 1.63$ would provide the optimum performance for lift coefficients between 0.0 and 0.4. For a conventional design, the wing would be configured with a moderately thick airfoil ($t/c \approx 0.04$) with maximum thickness located at 20 percent of the chord to minimize the zero-lift drag at $\beta \cot \Lambda = 0.6$ and to maximize the low-lift drag-due-to-lift characteristics. (See fig. 26.) The 65° swept delta wing with aspect ratio of 1.86 should provide a minimum zero-lift drag penalty and a significant improvement in drag due to lift compared with a more slender geometry. At $M = 1.63$, the effect of vacuum limit is minimal, providing a 70-percent increase in upper surface lifting potential over the 75° design ($\beta \cot \Lambda = 0.45$) and an 8-percent decrease from the 55° design ($\beta \cot \Lambda = 0.8$). If a simple variable camber system (simple flap), which is conical in nature, is added to the described design, the aerodynamic performance across the range of lift coefficient could approach that of the practical goal established in reference 40. (See fig. 65.) Also presented in the figure are the flat-wing aerodynamic characteristics for delta wings with $A = 1$ and 2 from figure 27. The projected performance levels probably represent the minimum and not the maximum allowable performance levels. If both the airfoil and

the camber are integrated together to take full advantage of the conical flow characteristics over the wing at zero-lift to high-lift conditions, then aerodynamic performance levels which exceed the practical goal limits might be realized.

Concluding Remarks

Through the empirical correlation of experimental data and theoretical analysis, a set of graphs have been developed which quantify the inviscid aerodynamics of delta wings at supersonic speeds.

The zero-lift wave-drag characteristics of delta wings with diamond, circular-arc, and NACA modified four-digit-series airfoils were determined through the application of a nonlinear computational technique. The nonlinear analysis varied substantially from the exact linear-theory predictions for all combinations of geometry and flow parameters under study. The nonlinear analysis showed that for slender wings with highly subsonic leading edges the zero-lift wave-drag correlation relationship is maintained; however, as the wing geometry becomes nonslender, the flow about the wing becomes nonlinear and the relationships which define the zero-lift wave-drag correlation parameter are not maintained.

The aerodynamic characteristics of delta wings at lifting conditions have been evaluated for the effects of wing leading-edge sweep, leading-edge bluntness, and wing thickness and camber and then summarized in the form of graphs which may be used to assess for the aerodynamics in the preliminary design process. Empirical curves have been developed for the lift-curve slope, nonlinear lift effects, maximum lift, longitudinal stability, and distribution of lift between the upper and lower surfaces of a wing. In addition, the impact of various airfoil parameters, wing leading-edge sweep, and lift coefficient on the drag-due-to-lift characteristics has been shown theoretically.

The various graphs which detail the aerodynamics of delta wings at both zero-lift and lifting conditions were then employed to define a preliminary wing design approach in which both the low-lift and high-lift design criteria were combined to define a feasible design space.

NASA Langley Research Center
Hampton, Virginia 23665-5225
December 11, 1987

Appendix

Nonlinear Methodology

The nonlinear computational technique (ref. 2) selected for analysis solves the nonconservative finite-difference analog of the full-potential equation in a spherical coordinate system. The method marches in the radial direction to obtain three-dimensional cross-flow solutions of the wing geometry. The ability to compute the flow over a wing with this method is restricted to conditions in which the flow in the marching direction remains supersonic; thus, the code would be expected to be more successful for higher free-stream Mach numbers. The solution technique is graphically depicted in figure A1. A series of three transformations are used in the code: the geometry in Cartesian coordinates is transformed to spherical coordinates followed by a stereographic projection (not shown) and a conformal mapping to a circle. A shearing transformation is then performed to the computational plane. Grid points are internally computed within the code and are positioned between the body surface (inner boundary) and the bow shock (outer boundary). The method has been shown to be ideally suited for the solution of three-dimensional wing flow fields (ref. 2).

Solutions were obtained by fitting the bow shock and capturing all internal shocks. Due to the supersonic nature of the wing trailing edge, the wake was modeled as an extension of the wing surface. Sensitivity studies were conducted to determine marching step size and cross-plane grid resolution. These studies indicated a dependence of both parameters to free-stream flow conditions as well as geometry. Selection of the marching step size was based upon the analysis of a series of airfoil geometries at various flow conditions. A representative sampling of this analysis is presented in figure A2 in which the axially integrated drag values for three airfoil types are presented for step sizes of 0.2, 0.5, and 1.0, which correspond to 50, 20, and 10 marching steps, respectively. Results of the analysis show a convergence of the solution with decreasing step size. Based upon these results and considerations of computational cost, a step size of 0.5 was selected for the study. Cross-plane mesh density was selected to be 30×30 based upon a similar parametric study. Presented in figure A3 are representative 30×30 cross-plane computational grids for the four basic airfoil types under investigation: diamond, circular arc, sharp NACA modified four-digit series, and blunt NACA modified four-digit series. The grid plots clearly show clustering of the grid points at the wing leading edge in both the radial and circumferential directions; this is critical to resolving the wing flow field.

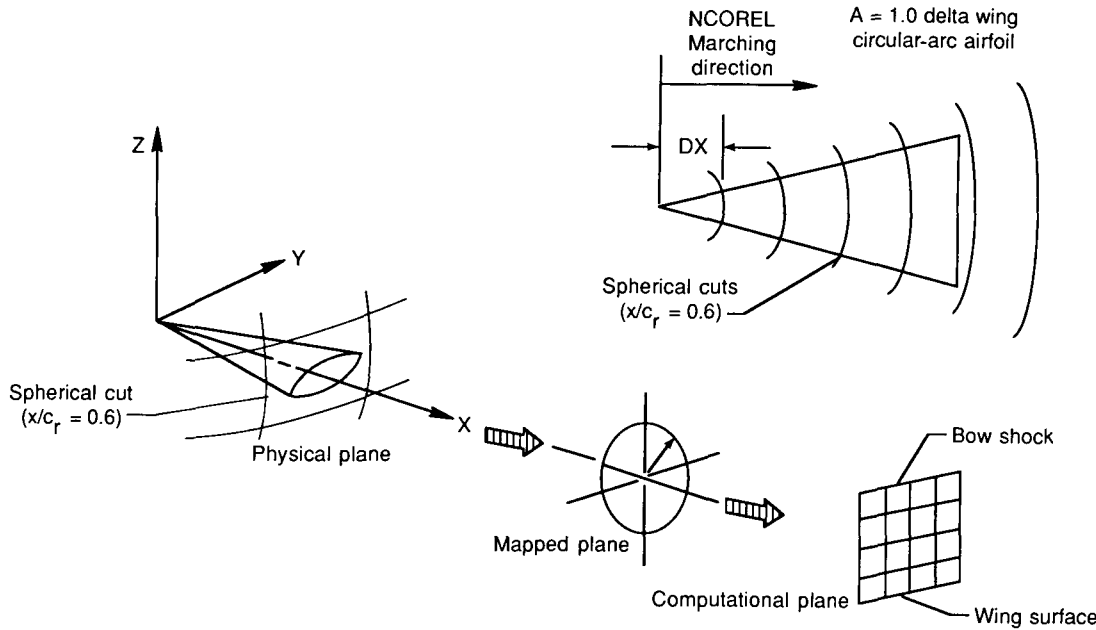


Figure A1. Nonlinear method solution process used for delta wing study.

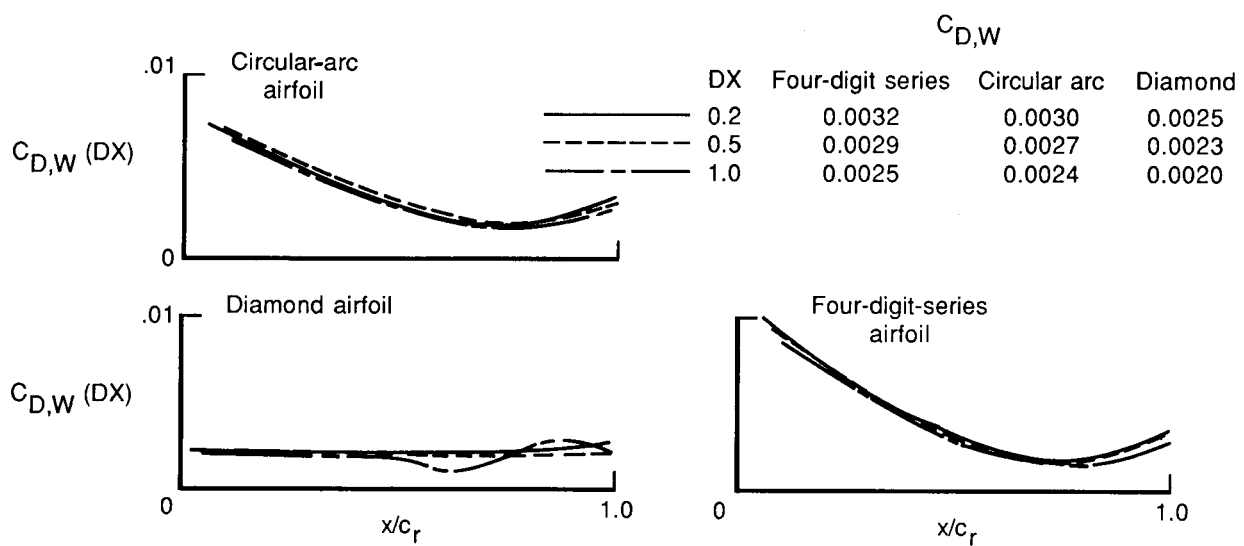


Figure A2. Selection of step size for analysis based upon delta wing with $A = 1.0$ and airfoils with $\tau = 0.04$ and $m = 0.5$.

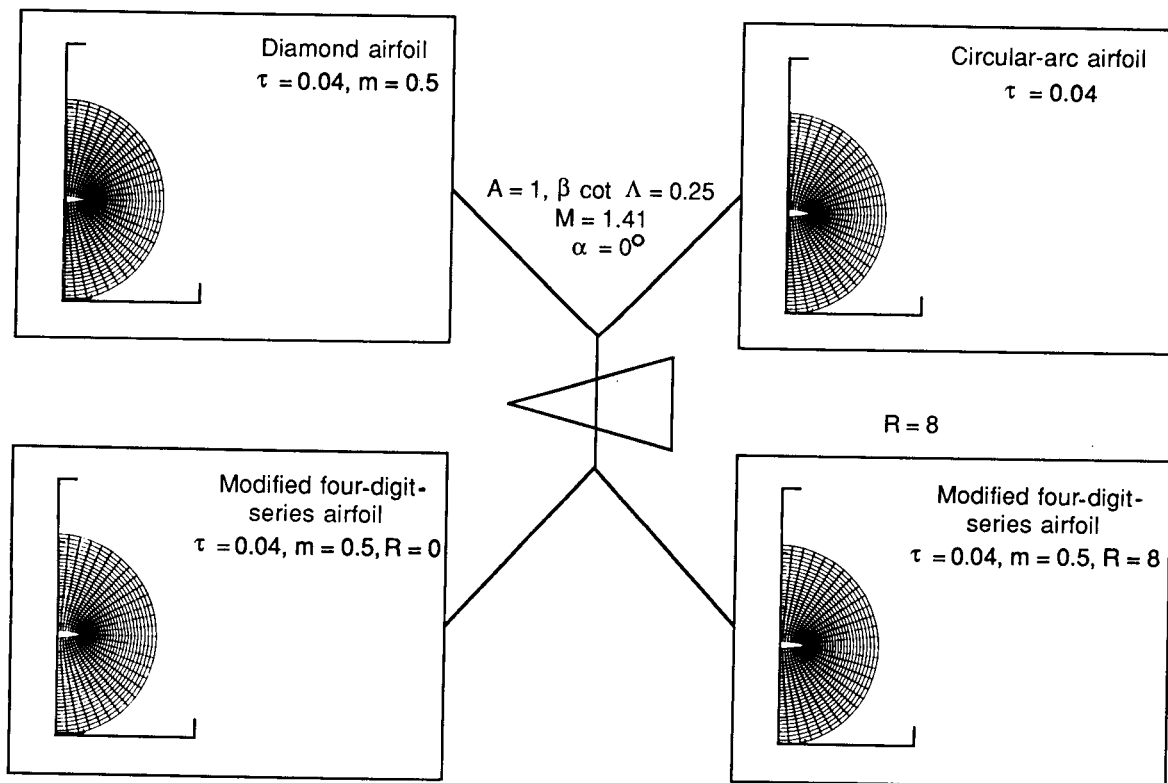


Figure A3. Representative computational grids for $A = 1.0$ delta wing at $M = 1.41$ and $\alpha = 0^\circ$.

References

1. Weber, J.; and King, C.: *Analysis of the Zero-Lift Wave Drag Measured on Delta Wings.* R. & M. No. 3818, British Aeronautical Research Council, 1978.
2. Siclari, Michael J.: *The NCOREL Computer Program for 3D Nonlinear Supersonic Potential Flow Computations.* NASA CR-3694, 1983.
3. Hill, William A., Jr.: *Experimental Lift of Low-Aspect-Ratio Triangular Wings at Large Angles of Attack and Supersonic Speeds.* NACA RM A57I17, 1957.
4. Love, Eugene S.: *Investigations at Supersonic Speeds of 22 Triangular Wings Representing Two Airfoil Sections for Each of 11 Apex Angles.* NACA Rep. 1238, 1955. (Supersedes NACA RM L9D07.)
5. Henderson, Arthur, Jr.: *Experimental Investigation of the Zero-Lift Wave Drag of Seven Pairs of Delta Wings With Constant and Varying Thickness Ratios at Mach Numbers of 1.62, 1.93, and 2.41.* NACA RM L55D13, 1955.
6. Stallings, Robert L., Jr.; and Lamb, Milton: *Wing-Alone Aerodynamic Characteristics for High Angles of Attack at Supersonic Speeds.* NASA TP-1889, 1981.
7. Smith, Fred M.: *Experimental and Theoretical Aerodynamic Characteristics of Two Low-Aspect-Ratio Delta Wings at Angles of Attack to 50° at a Mach Number of 4.07.* NACA RM L57E02, 1957.
8. Hatch, John E., Jr.; and Hargrave, L. Keith: *Effects of Reynolds Number on the Aerodynamic Characteristics of a Delta Wing at Mach Number of 2.41.* NACA RM L51H06, 1951.
9. Gallagher, James J.; and Mueller, James N.: *An Investigation of the Maximum Lift of Wings at Supersonic Speeds.* NACA Rep. 1227, 1955. (Supersedes NACA RM L7J10.)
10. Squire, L. C.; Jones, J. G.; and Stanbrook, A.: *An Experimental Investigation of the Characteristics of Some Plane and Cambered 65° Delta Wings at Mach Numbers From 0.7 to 2.0.* R. & M. No. 3305, British Aeronautical Research Council, 1963.
11. Ellis, Macon C., Jr.; and Hasel, Lowell E.: *Preliminary Investigation at Supersonic Speeds of Triangular and Sweptback Wings.* NACA TN 1955, 1949.
12. Vincenti, Walter G.; Nielsen, Jack N.; and Matteson, Frederick H.: *Investigation of Wing Characteristics at a Mach Number of 1.58. I—Triangular Wings of Aspect Ratio 2.* NACA RM A7I10, 1947.
13. Ulmann, Edward F.; and Dunning, Robert W.: *Aerodynamic Characteristics of Two Delta Wings at Mach Number 4.04 and Correlations of Lift and Minimum-Drag Data for Delta Wings at Mach Numbers From 1.62 to 6.9.* NACA RM L52K19, 1952.
14. Hatch, John E., Jr.; and Gallagher, James J.: *Aerodynamic Characteristics of a 68.4° Delta Wing at Mach Numbers of 1.6 and 1.9 Over a Wide Reynolds Number Range.* NACA RM L53I08, 1953.
15. Menees, Gene P.: *Lift, Drag, and Pitching Moment of an Aspect-Ratio-2 Triangular Wing With Leading-Edge Flaps Designed To Simulate Conical Camber.* NASA MEMO 10-5-58A, 1958.
16. Kaattari, George E.: *Pressure Distributions on Triangular and Rectangular Wings to High Angles of Attack—Mach Numbers 1.45 and 1.97.* NACA RM A54D19, 1954.
17. Hall, Charles F.: *Lift, Drag, and Pitching Moment of Low-Aspect-Ratio Wings at Subsonic and Supersonic Speeds.* NACA RM A53A30, 1953.
18. Boatright, William B.: *Experimental Study and Analysis of Loading and Pressure Distributions on Delta Wings Due to Thickness and to Angle of Attack at Supersonic Speeds.* NACA RM L56I14, 1956.
19. Briggs, M. M.; Reed, R. E.; and Nielsen, J. N.: *Wing-Alone Aerodynamic Characteristics to High Angles of Attack at Subsonic and Transonic Speeds.* NEAR TR 269 (Contract DAAG29-79-C-0020), Nielsen Engineering & Research, Inc., Nov. 1982. (Available from DTIC as AD A125 764.)
20. Michael, William H., Jr.: *Flow Studies on Flat-Plate Delta Wings at Supersonic Speed.* NACA TN 3472, 1955.
21. Miller, David S.; and Wood, Richard M.: *Lee-Side Flow Over Delta Wings at Supersonic Speeds.* NASA TP-2430, 1985.
22. Boyd, John W.; and Phelps, E. Ray: *A Comparison of the Experimental and Theoretical Loading Over Triangular Wings at Supersonic Speeds.* NACA RM A50J17, 1951.
23. Britton, J. W.: *Pressure Measurements at Supersonic Speeds on Three Uncambered Conical Wings of Unit Aspect Ratio.* C.P. No. 641, British Aeronautical Research Council, 1963.
24. Michael, William H., Jr.: *Flow Studies on Drooped-Leading-Edge Delta Wings at Supersonic Speed.* NACA TN 3614, 1956.
25. Iggleston, M. S.: *Wind Tunnel Measurements of the Lift-Dependent Drag of Thin Conically Cambered Slender Delta Wings at Mach Numbers 1.4 and 1.8.* Tech. Note No. Aero 2677, British Royal Aircraft Establishment, Apr. 1960.
26. Abbott, Ira H.; and Von Doenhoff, Albert E.: *Theory of Wing Sections.* Dover Publ., Inc., c.1959.
27. Bishop, R. A.; and Cane, E. G.: *Charts of the Theoretical Wave Drag of Wings at Zero-Lift.* C.P. No. 313, British Aeronautical Research Council, 1957.
28. Puckett, Allen E.: *Supersonic Wave Drag of Thin Airfoils.* *J. Aeronaut. Sci.*, vol. 13, no. 9, Sept. 1946, pp. 475–484.
29. Middleton, W. D.; Lundry, J. L.; and Coleman, R. G.: *A System for Aerodynamic Design and Analysis of Supersonic Aircraft. Part 2—User's Manual.* NASA CR-3352, 1980.
30. Wood, Richard M.; and Miller, David S.: *Experimental Investigation of Leading-Edge Thrust at Supersonic Speeds.* NASA TP-2204, 1983.
31. Miller, David S.; and Wood, Richard M.: *An Investigation of Wing Leading-Edge Vortices at Supersonic Speeds.* AIAA-83-1816, July 1983.
32. Mayer, John P.: *A Limit Pressure Coefficient and an Estimation of Limit Forces on Airfoils at Supersonic Speeds.* NACA RM L8F23, 1948.

33. Stanbrook, A.; and Squire, L. C.: Possible Types of Flow at Swept Leading Edges. *Aeronaut. Q.*, vol. XV, pt. 1, Feb. 1964, pp. 72-82.
34. Brown, C. E.; and Michael, W. H., Jr.: Effect of Leading-Edge Separation on the Lift of a Delta Wing. *J. Aeronaut. Sci.*, vol. 21, no. 10, Oct. 1954, pp. 690-694, 706.
35. Squire, L. C.: *Camber Effects on the Non-Linear Lift of Slender Wings With Sharp Leading Edges*. C.P. No. 924, British Aeronautical Research Council, 1967.
36. Squire, L. C.: Experimental Work on the Aerodynamics of Integrated Slender Wings for Supersonic Flight. *Prog. Aerosp. Sci.*, vol. 20, no. 1, 1981, pp. 1-96.
37. Mack, Robert J.: *Wind-Tunnel Investigation of Leading-Edge Thrust on Arrow Wings in Supersonic Flow*. NASA TP-2167, 1983.
38. Covell, Peter F.; Miller, David S.; and Wood, Richard M.: An Evaluation of Leading-Edge Flap Performance on Delta and Double-Delta Wings at Supersonic Speeds. AIAA-86-0315, Jan. 1986.
39. Miller, David S.; and Wood, Richard M.: Aerodynamic Design Considerations for Efficient High-Lift Supersonic Wings. AIAA-85-4076, Oct. 1985.
40. Wood, Richard M.; Miller, David S.; Raney, David L.; and Roesch, Michael T.: *A Low-Lift Wing Camber Design Approach for Fighter Aircraft*. NASA TP-2465, 1985.

Table I. Experimental Data Set

Reference	Planform	Airfoil			Flow conditions			Data type			
		A	Type	t/c	LE	M	α , deg	N_{Re}/\bar{c}	Force	Pressure	Flow visualization
3	3 wings 76° to 84.6°	Modified biconvex	4% at 0.59c	Sharp	1.96 to 3.30	0 to 47	1.68×10^6 to 4.48×10^6		✓		
4	11 wings 45° to 80°	Diamond	8% at 0.18c	Sharp and blunt	1.62 to 2.40	-6 to 6	0.46×10^6 to 1.39×10^6		✓		
	4 wings 65° to 75°	Slab		Sharp and blunt	1.92	-6 to 6	0.46×10^6 to 1.39×10^6		✓		
5	4 wings 48° to 73°	Diamond	6% at 0.20c to 0.55c	Sharp	1.62 to 2.41	-2 to 6	2.36×10^6 to 4.32×10^6		✓		
6	3 wings 63.43° to 82.87°	Slab		Sharp	1.60 to 4.60	-5 to 60	1.41×10^6 to 2.82×10^6		✓		
7	2 wings 60°	Diamond	5%	Sharp	4.07	-4 to 50	5.3×10^6		✓		
	71.6°	Diamond	8%	Sharp	4.07	-4 to 50	6×10^6				
8	1 wing 68.6°	NACA-00	4 to 6.24%	Blunt	2.41	0 to 20	1.04×10^6 to 18.3×10^6		✓	✓	
9	3 wings 45° and 64°	Slab		Sharp	1.55 to 2.32	0 to 50	0.18×10^6 to 0.49×10^6		✓		
	58°	Diamond	10% at 0.50c	Sharp	2.40					✓	
10	2 wings 65°	RAE 101 Biconvex	4%	Blunt	1.51 to 2.0	-6 to 10	3×10^6				
11	8 wings 36.4° to 70.6°	Slab		Blunt	1.43 and 1.71	-5 to 5	0.24×10^6 to 0.62×10^6		✓		
12	2 wings 63.43°	Diamond	5% at 0.20c and 0.50c	Sharp and blunt	1.53	-2 to 16	0.75×10^6		✓		
13	2 wings 60°	Diamond	8% at 0.18c and 0.60c	Sharp	4.04	-15 to 15	6×10^6		✓		
14	2 wings 68.4°	NACA-00	4 to 6.24% at 0.30c	Blunt	1.6 and 1.9	-4 to 16	2.2×10^6 to 18.4×10^6		✓	✓	
15	1 wing 63.26°	NACA-0003	6%	Blunt	1.30 to 2.22	-6 to 18	3.68×10^6		✓		
16	2 wings 45° and 63.4°	Biconvex	5% at 0.50c	Sharp	1.45 and 1.97	0 to 50	0.68×10^6 to 3.27×10^6		✓		
17	3 wings 45° to 63.26°	NACA-0003 and Biconvex	3 to 8%	Sharp and blunt	1.2 to 1.7	-4 to 20	1.4×10^6 to 3.0×10^6		✓		

Table I. Concluded

Reference	Planform	Airfoil			Flow conditions			Data type		
		A	Type	t/c	LE	M	α , deg	N_{Re}/\bar{c}	Force	Pressure
18	3 wings 53° to 66.6°	65A003	3%	Blunt	1.62 to 2.41	0 to 20	2.3×10^6 to 4.65×10^6	✓	✓	
19	3 wings 63.43° to 82.87°	Slab		Sharp	0.30 to 1.20	0 to 55	1×10^6 to 2×10^6	✓	✓	
20	6 wings 58.25° to 85°	Flat		Sharp	1.90	0 to 20	5.21×10^6 to 9.38×10^6	✓	✓	
21	4 wings 52.5° to 75°	Flat		Sharp	1.50 to 2.80	0 to 20	0.86×10^6 to 2.46×10^6	✓	✓	✓
22	2 wings 45° 45°	NACA 0006-63	6%	Blunt	1.20	0 to 20	1.8×10^6	✓	✓	
					1.30 to 1.70					
23	3 wings 76°	Cross sections: 30° Diamond 30° Biconvex 60° Biconvex	Conical	Sharp	1.30 to 2.80	0 to 16	3.63×10^6 to 2.26×10^6	✓	✓	
24	3 wings 58.25° to 75°	Flat	Cambered	Sharp	1.90	0 to 20	4.7×10^6 to 8.4×10^6	✓	✓	✓
25	8 wings 71.56°	Slab		Sharp	1.40 and 1.80	-8 to 12	0.66×10^6	✓		

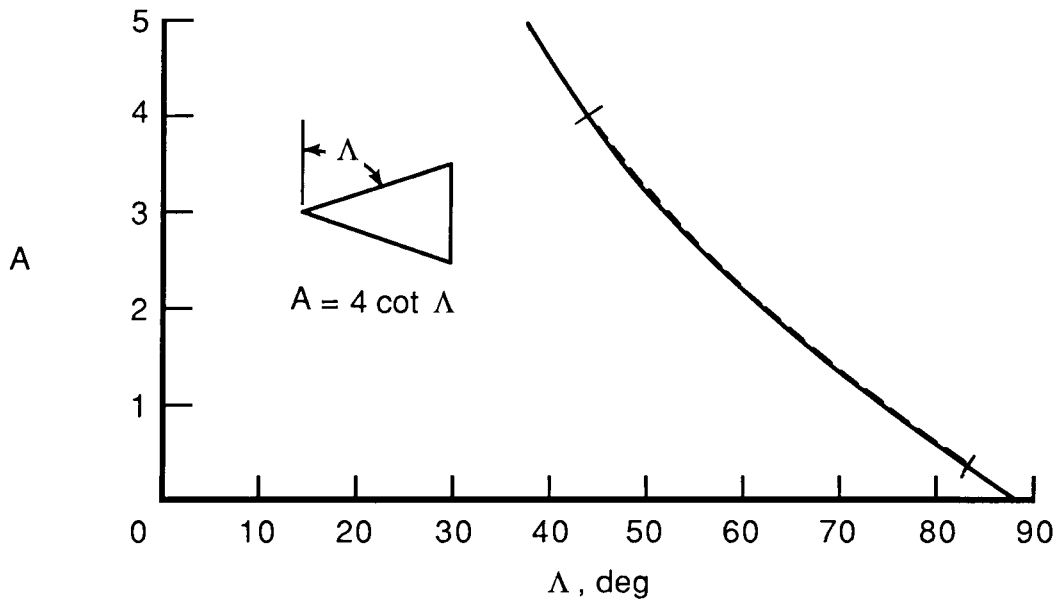


Figure 1. Relationship between A and Λ for delta wings.

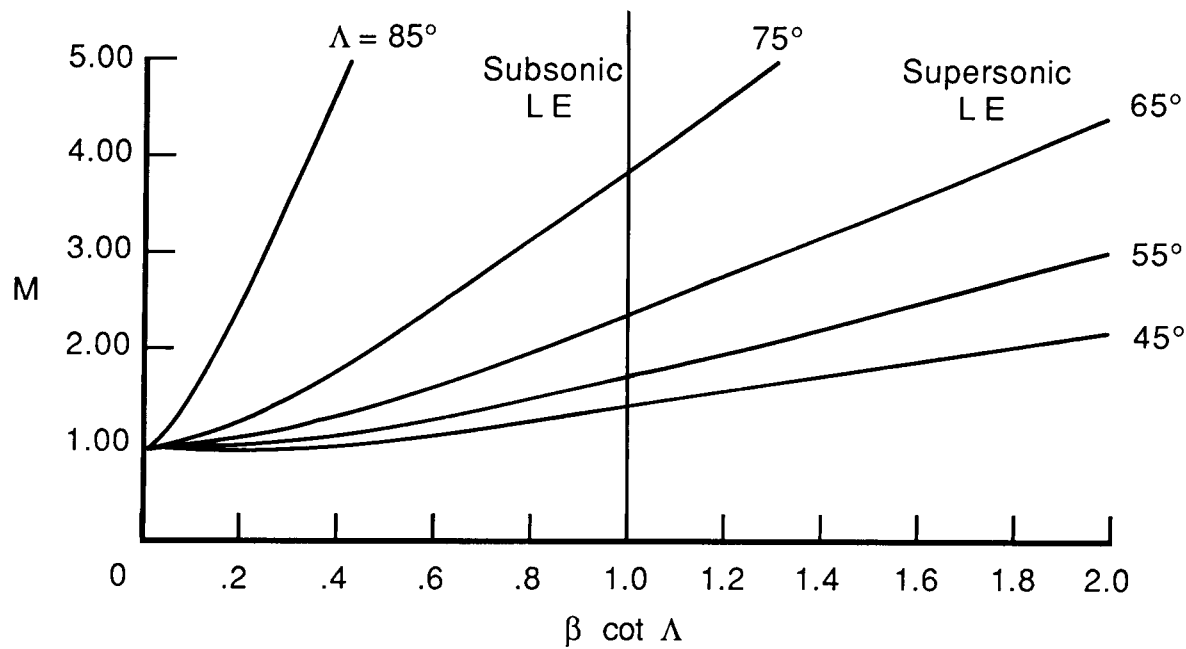


Figure 2. Relationship between M and $\beta \cot \Lambda$ for delta wings.

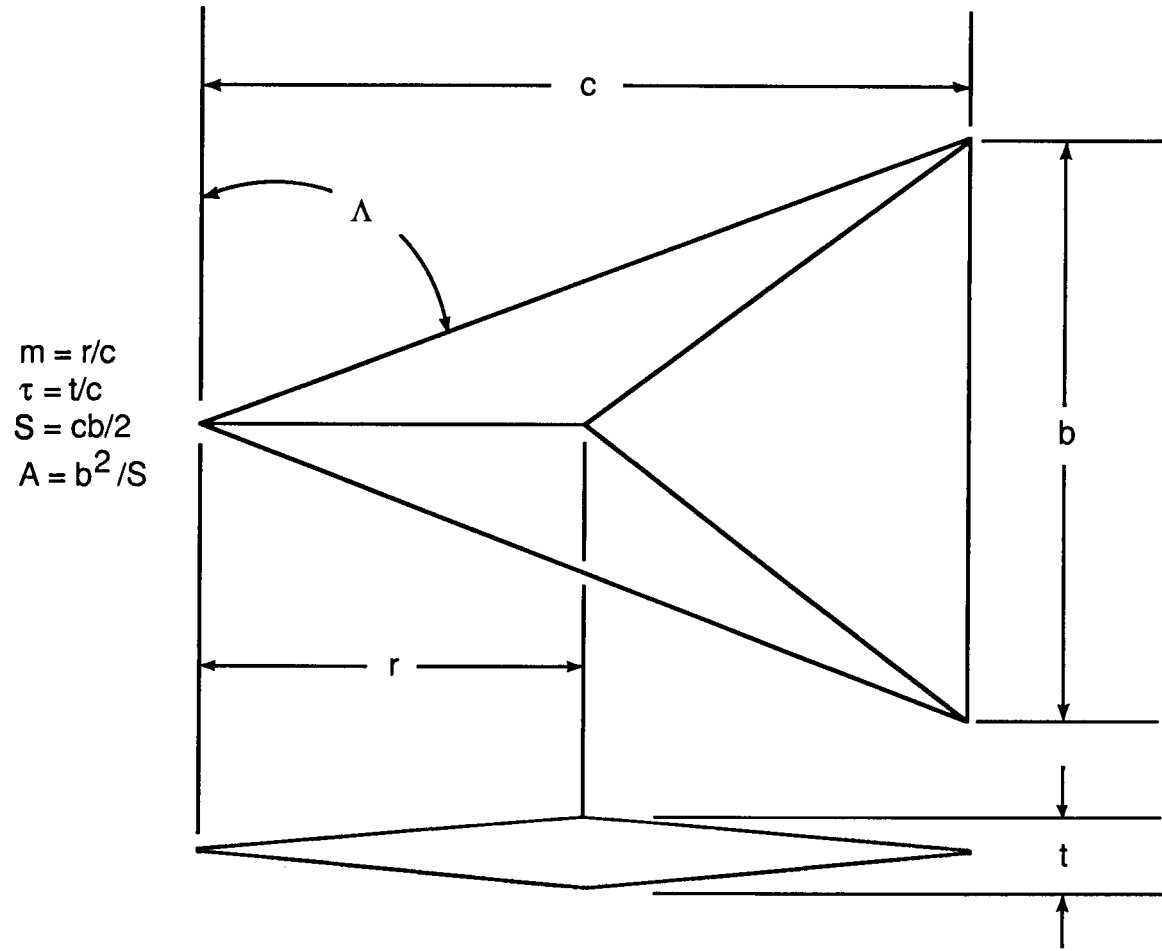


Figure 3. Identification of geometric parameters for delta wings with diamond airfoil.

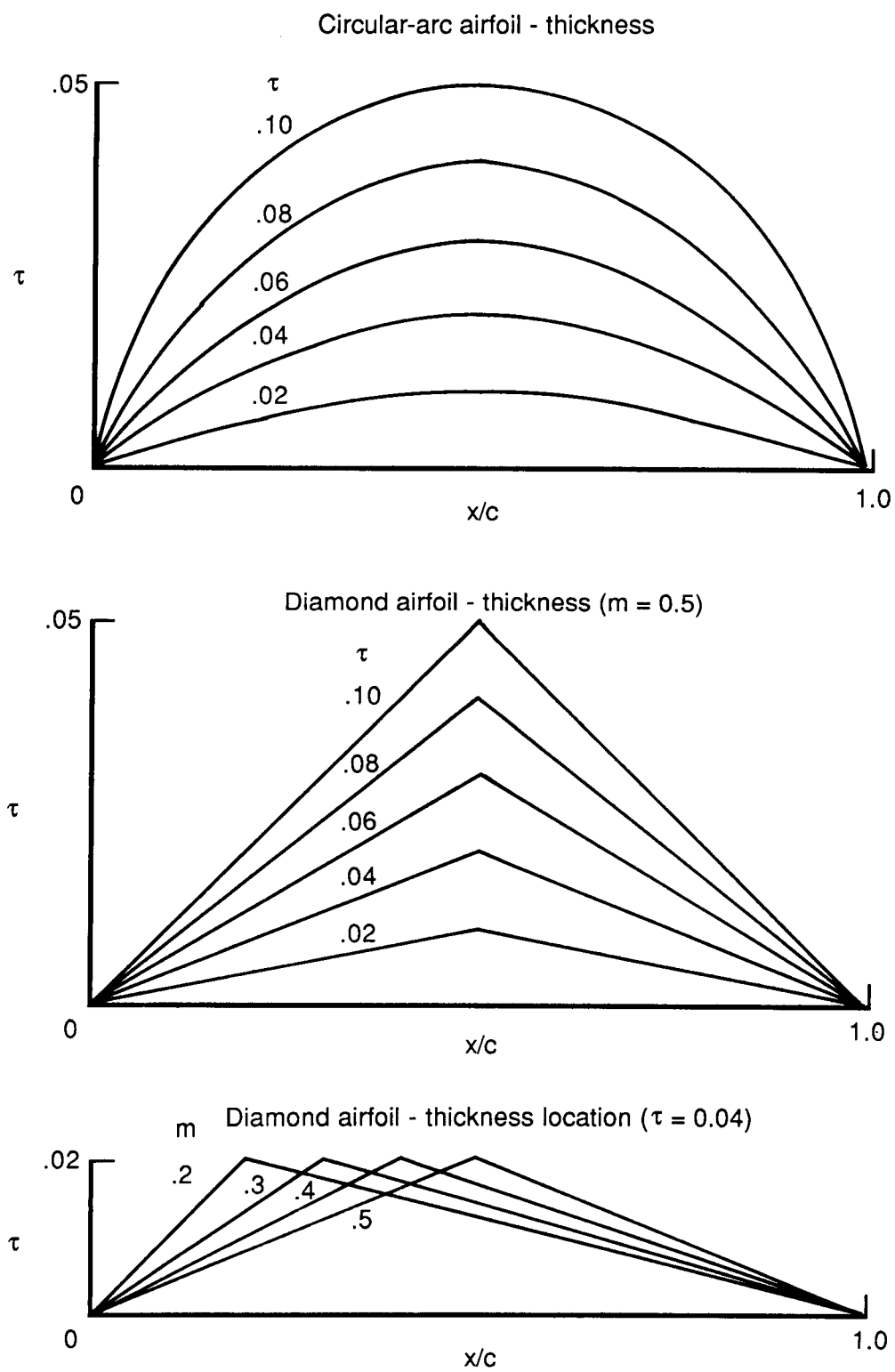


Figure 4. Representative profiles of circular-arc and diamond airfoils.

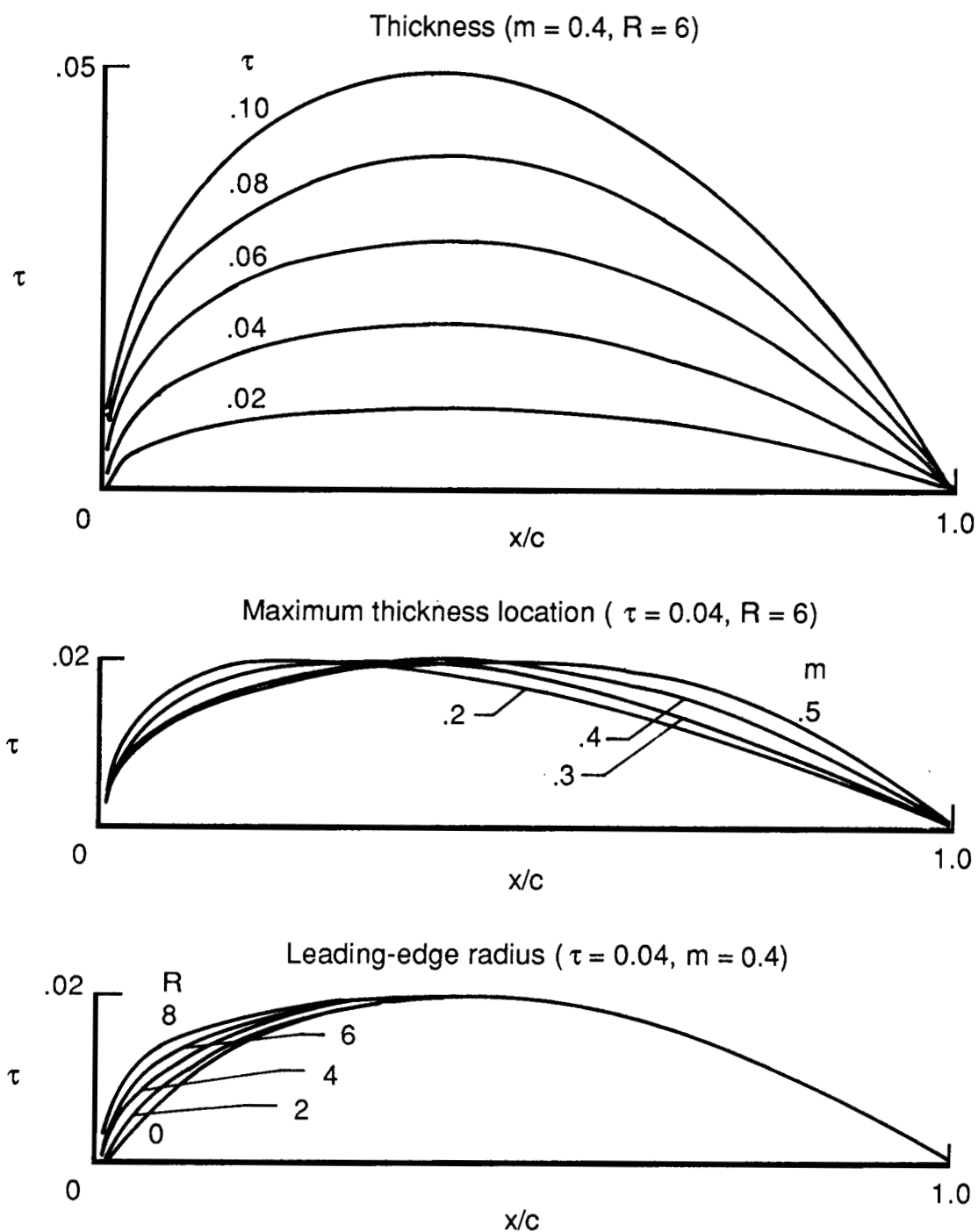


Figure 5. Representative profiles of NACA four-digit-series airfoil.

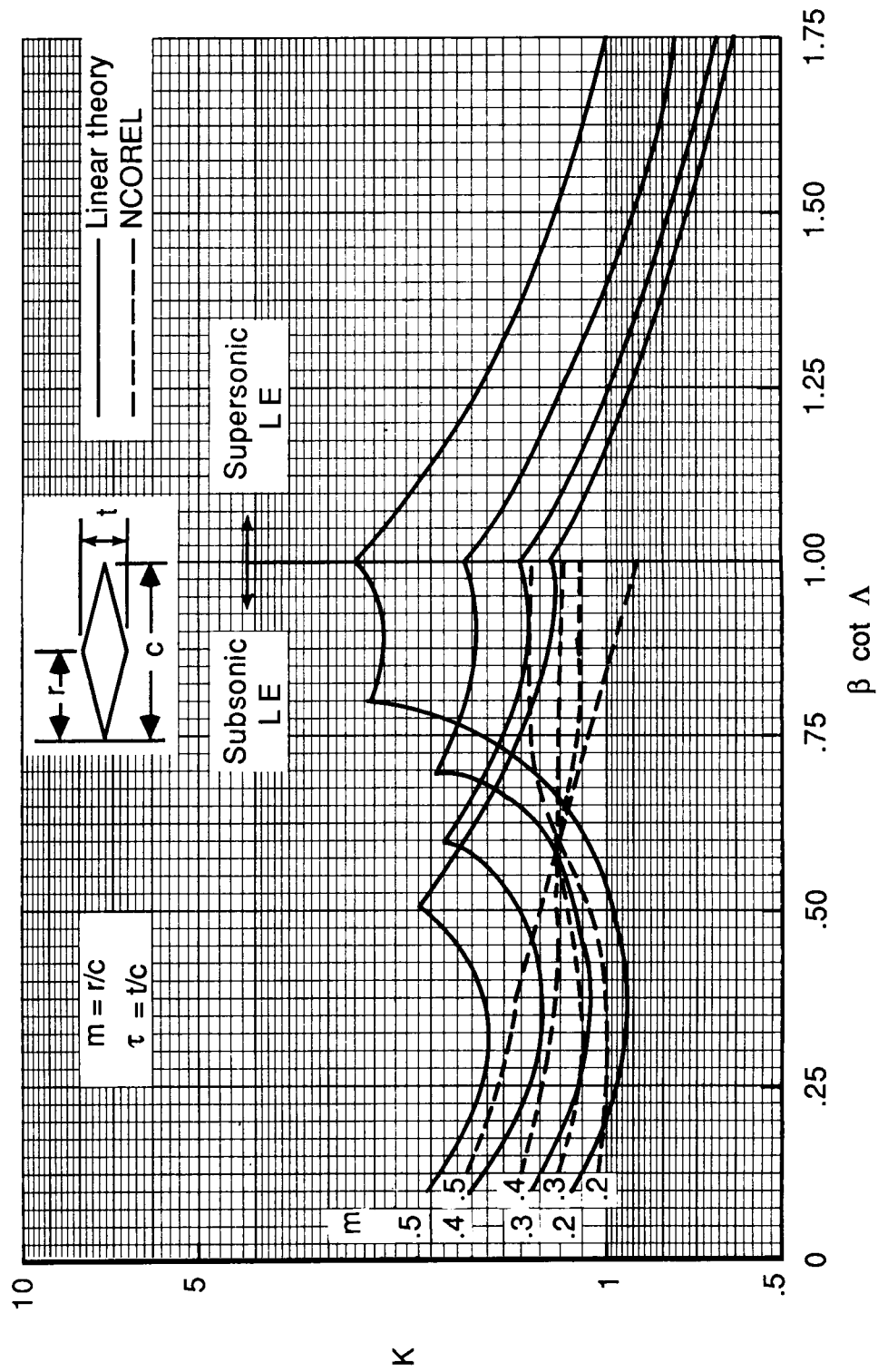


Figure 6. Linear- and nonlinear-theory-predicted zero-lift wave drag for delta wings with diamond airfoils.

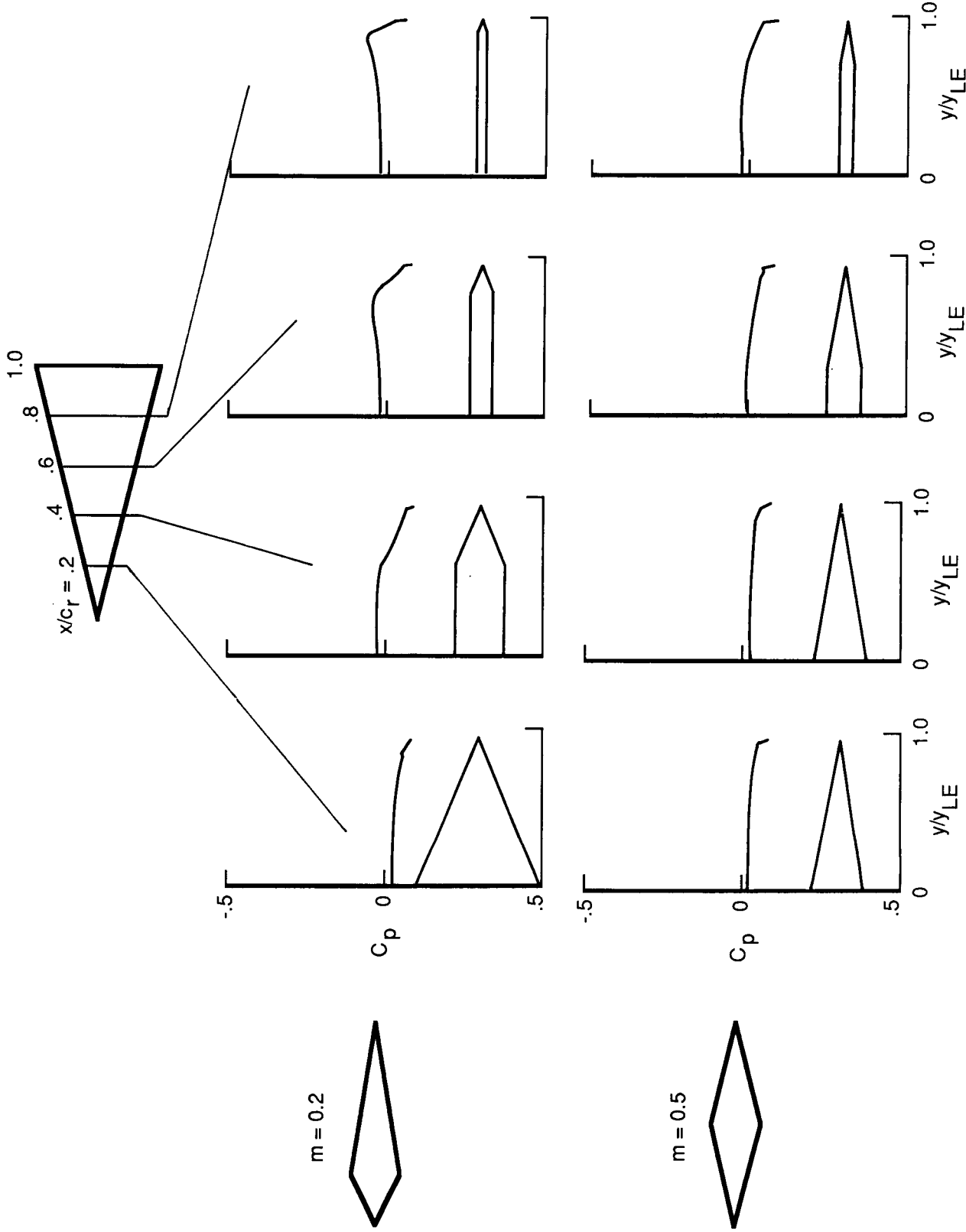


Figure 7. Spanwise pressure distributions predicted by nonlinear theory for delta wing with $A = 1.0$ and diamond airfoil with $r = 0.04$ at $M = 2.60$.

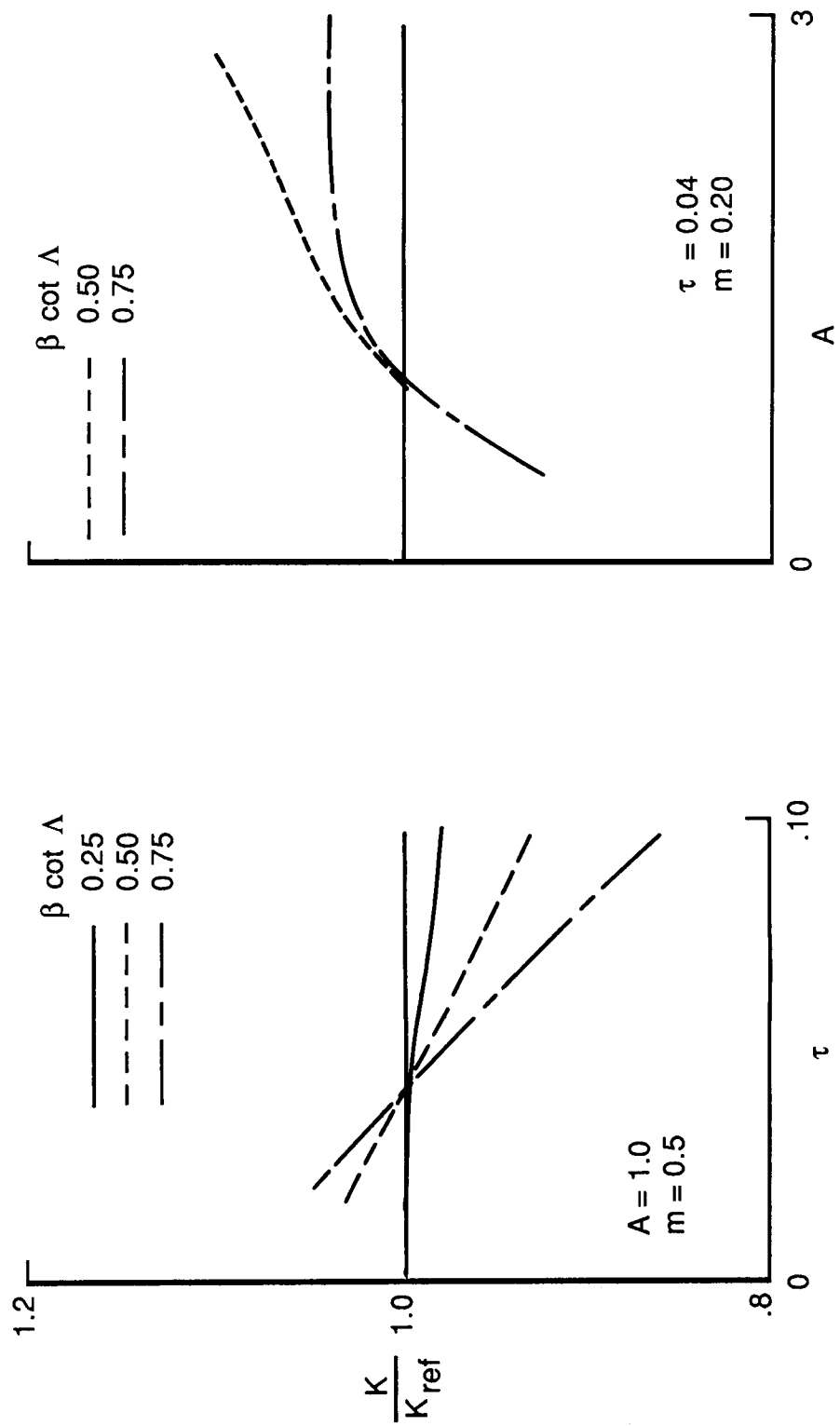


Figure 8. Nonlinear-theory-predicted effect of τ and A for delta wings with diamond airfoils.

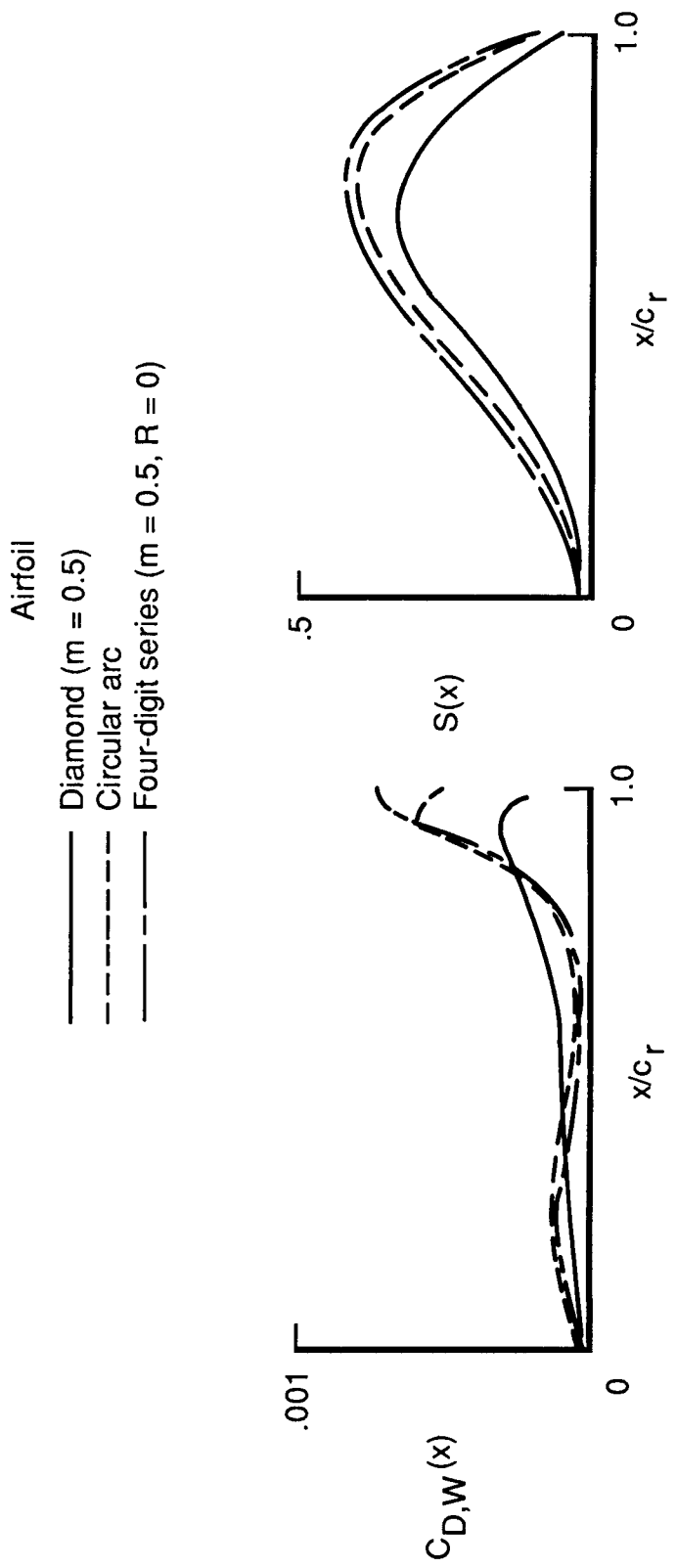


Figure 9. Axial distribution of area and nonlinear-theory-predicted drag for delta wing with $A = 1.0$ and 4-percent-thick airfoils at $M = 1.80$.

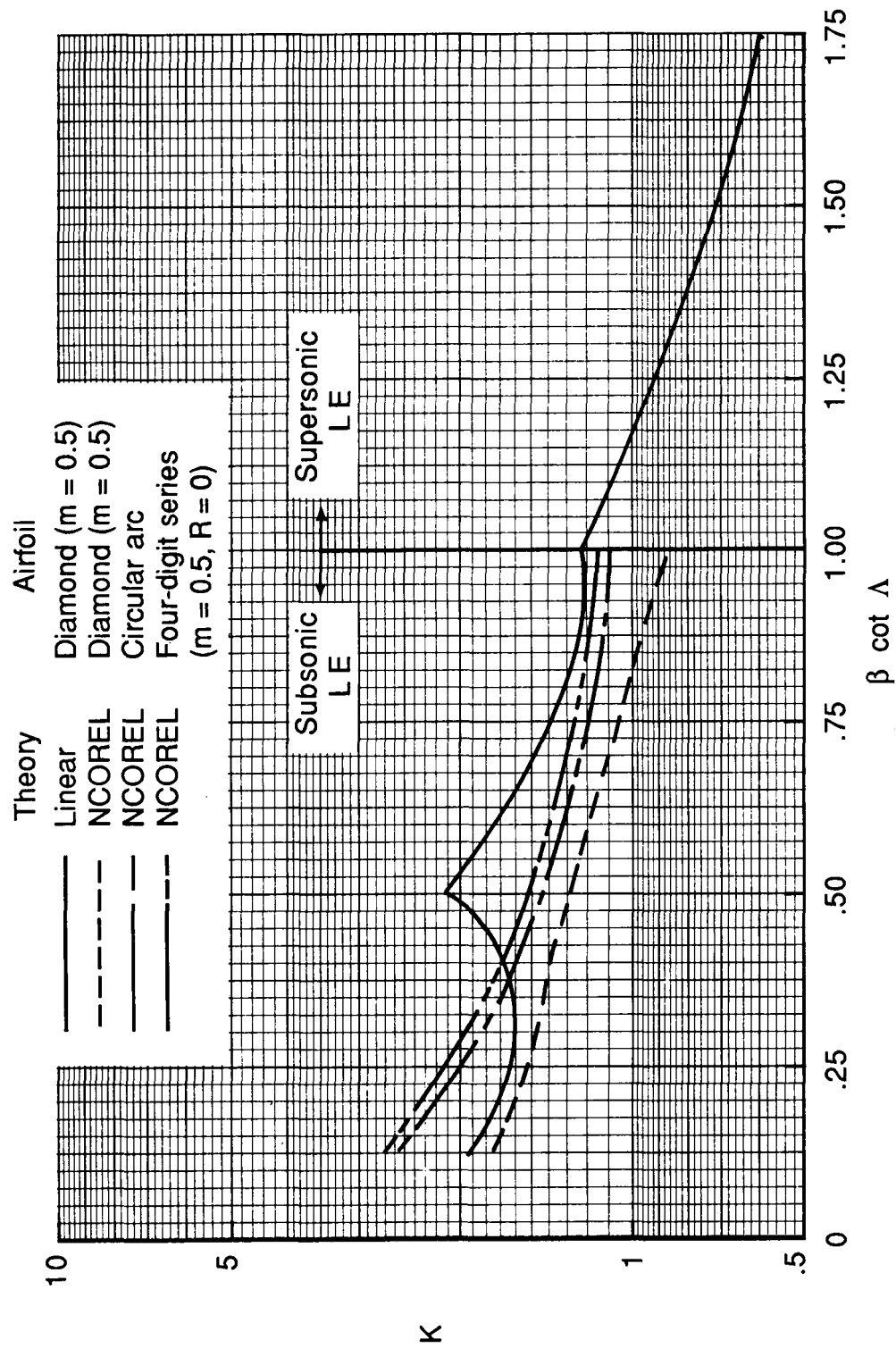


Figure 10. Linear- and nonlinear-theory-predicted zero-lift wave drag for delta wings.

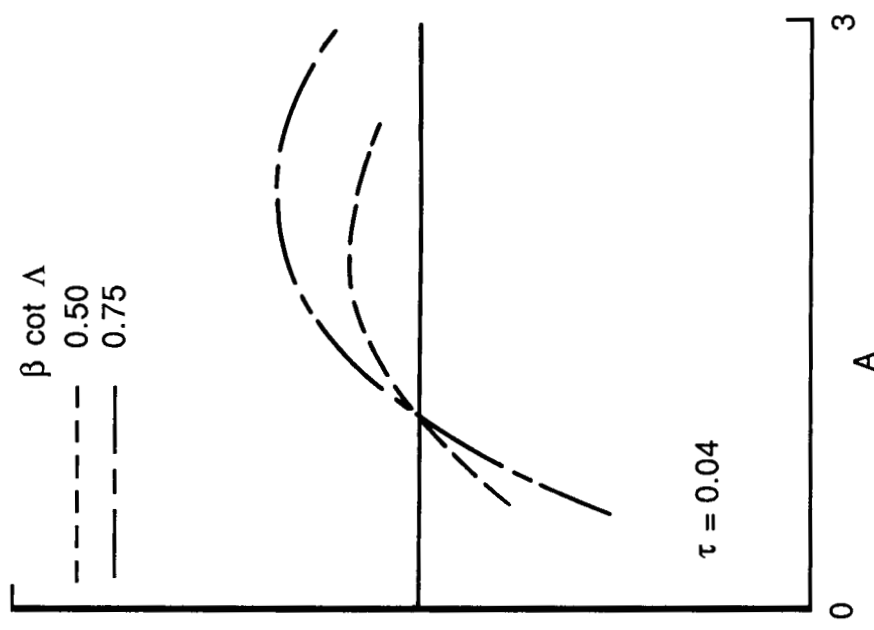
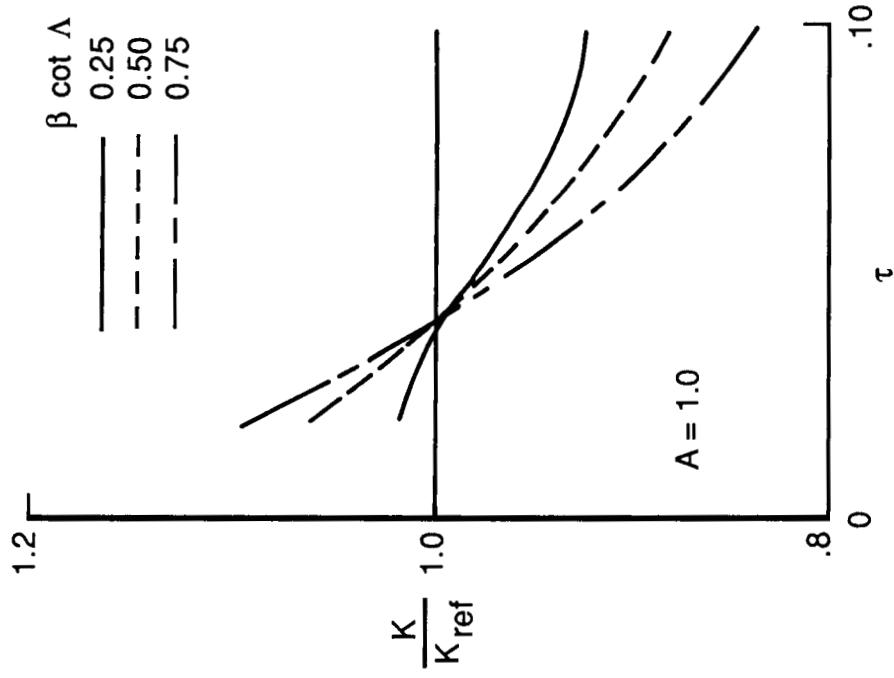


Figure 11. Nonlinear-theory-predicted effect of τ and A for delta wings with circular-arc airfoils.

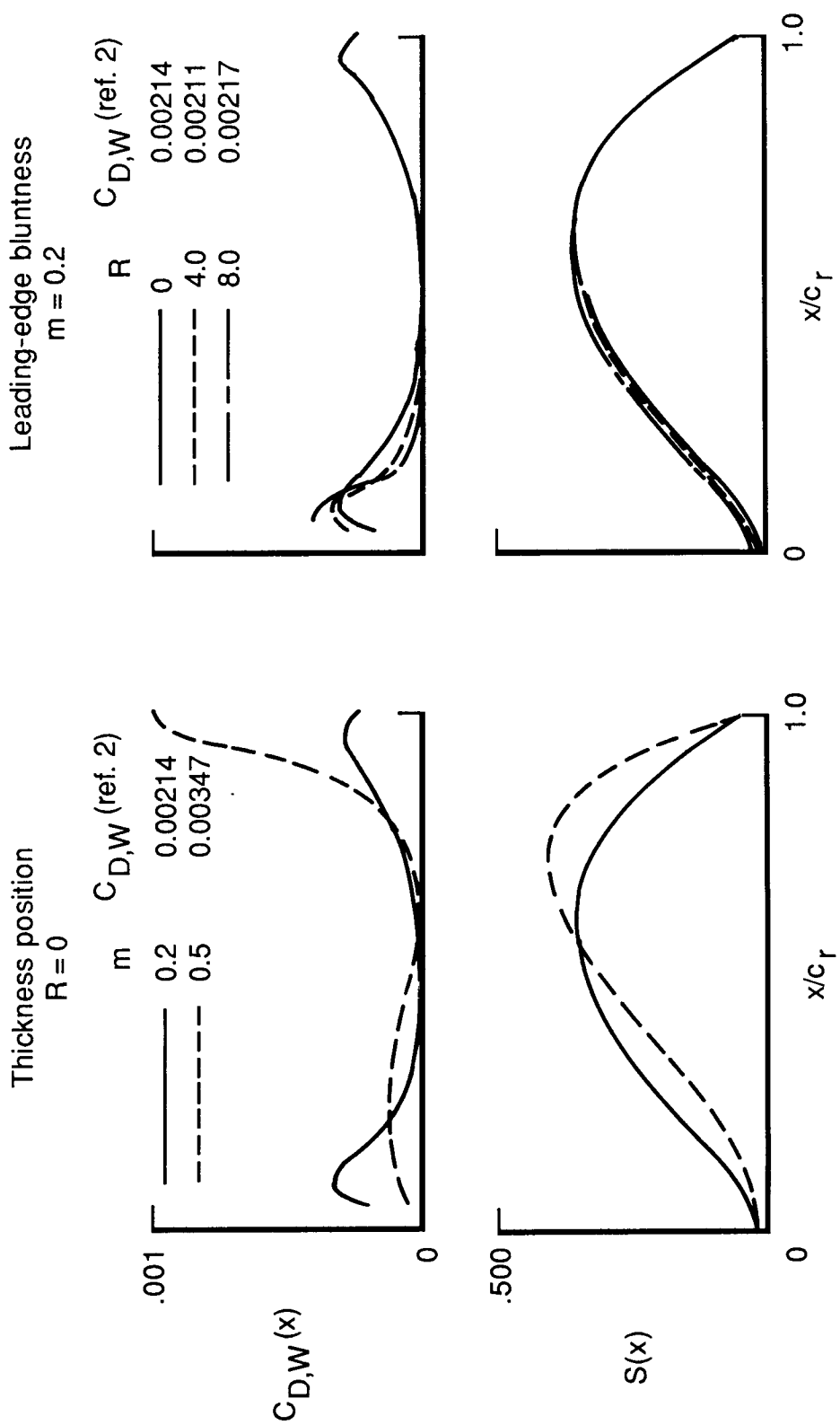


Figure 12. Axial distribution of area and nonlinear-theory-predicted drag for delta wing with $A = 1.0$ and 4-percent-thick modified NACA four-digit-series airfoils.

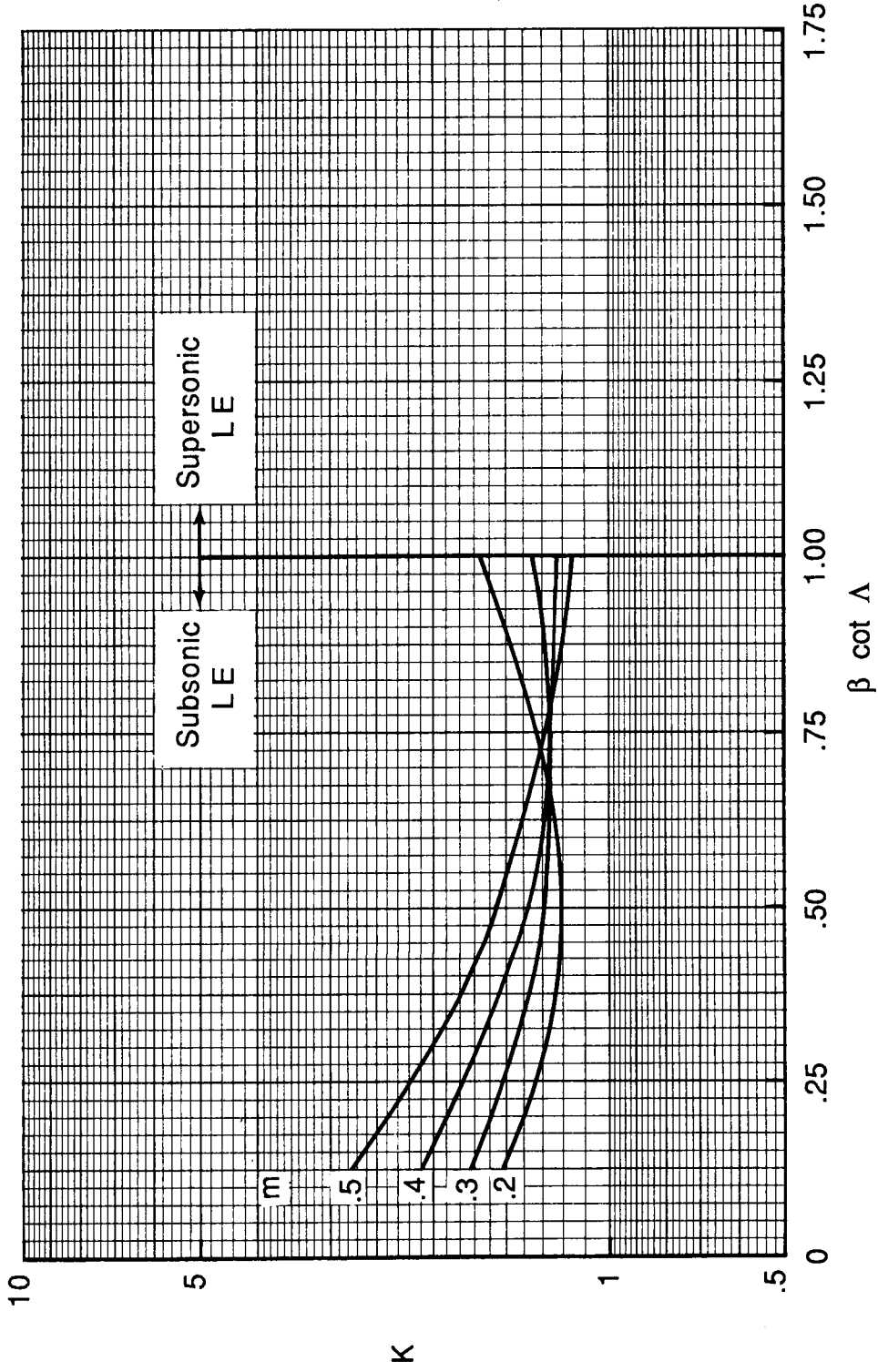


Figure 13. Nonlinear-theory-predicted zero-lift wave drag of delta wing with NACA modified four-digit-series airfoils.

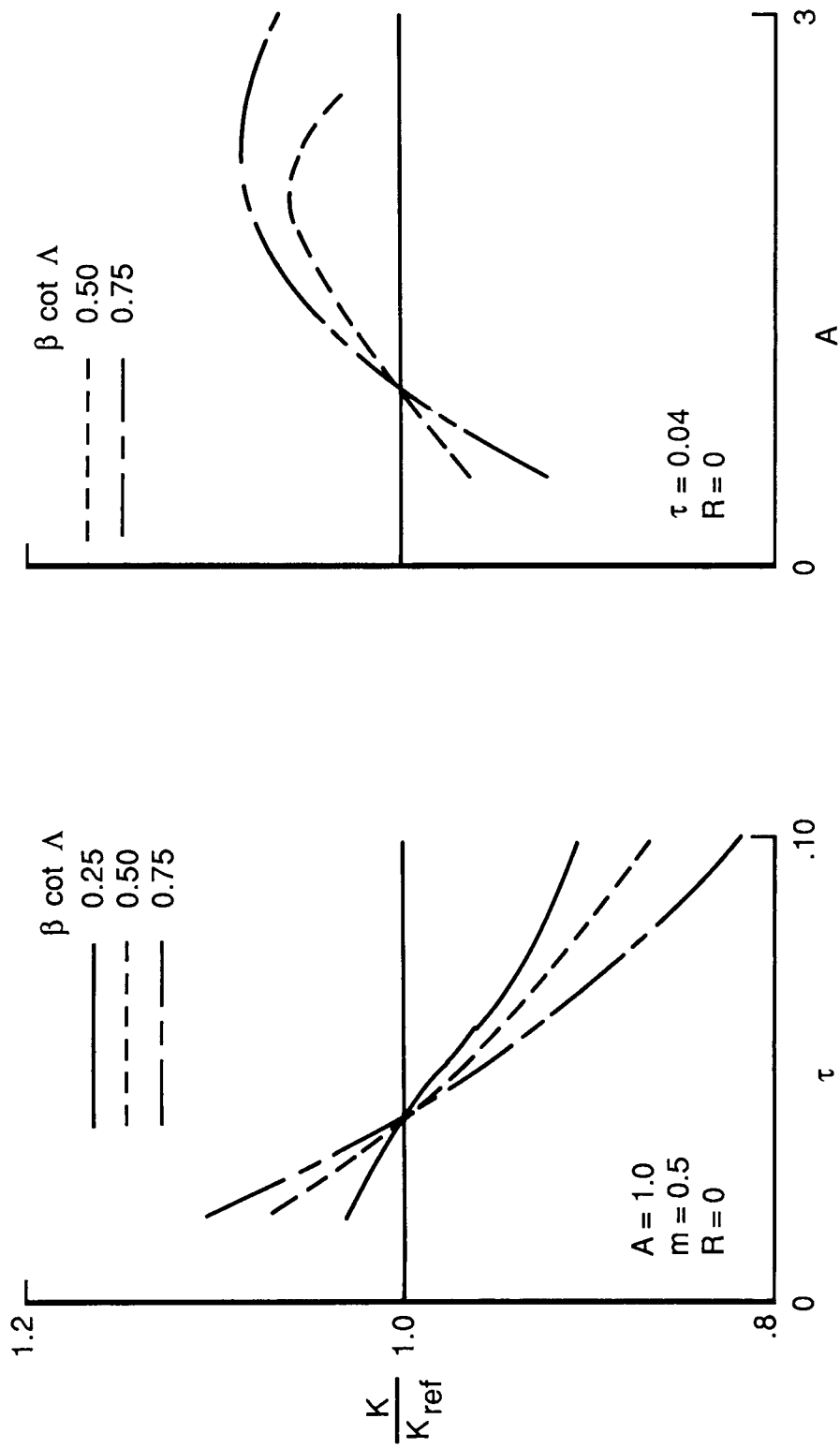


Figure 14. Nonlinear-theory-predicted τ and A effects for delta wings with modified NACA four-digit-series airfoils.

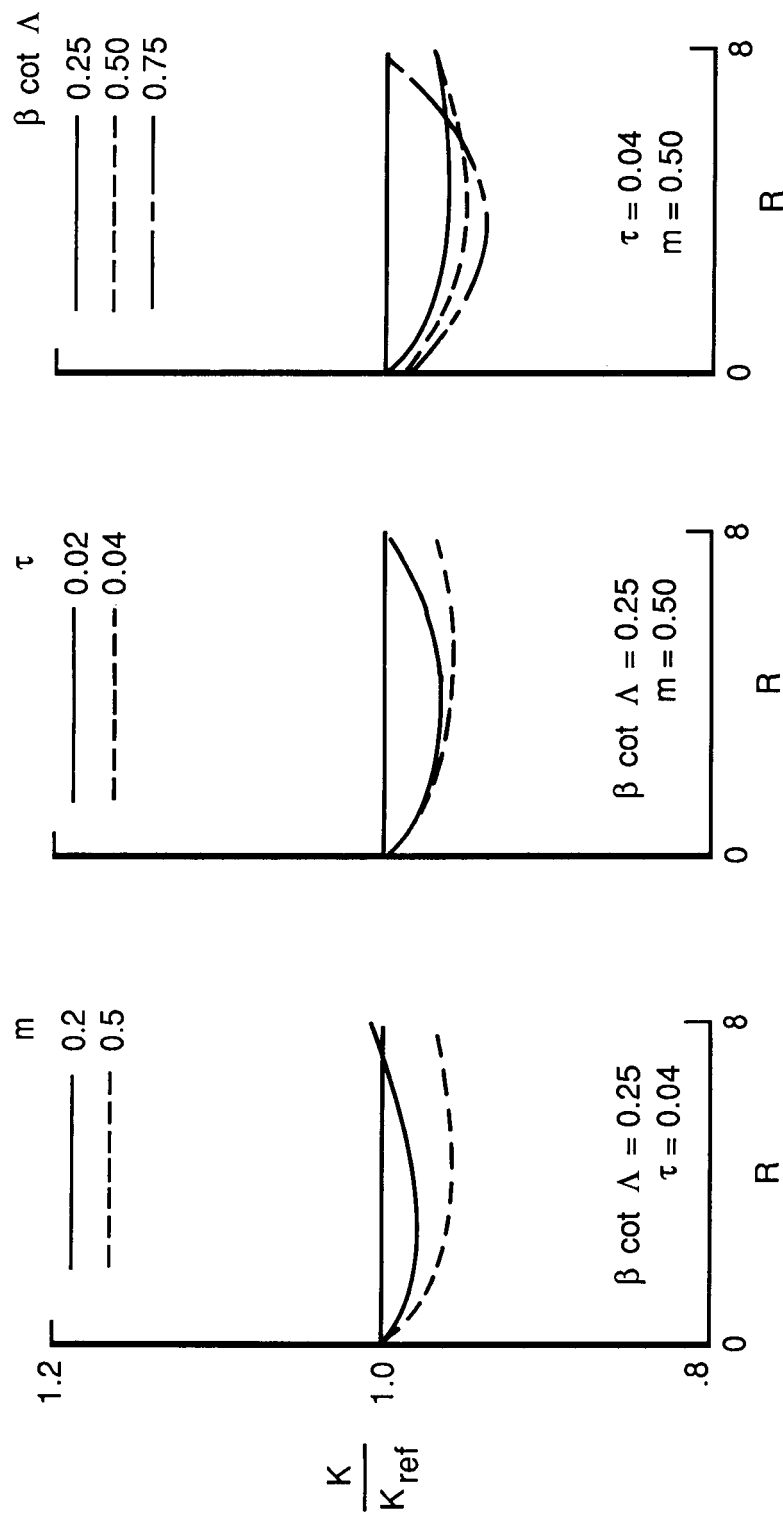


Figure 15. Nonlinear-theory-predicted effect of airfoil bluntness for delta wing with $A = 1.0$ and modified NACA four-digit-series airfoil.

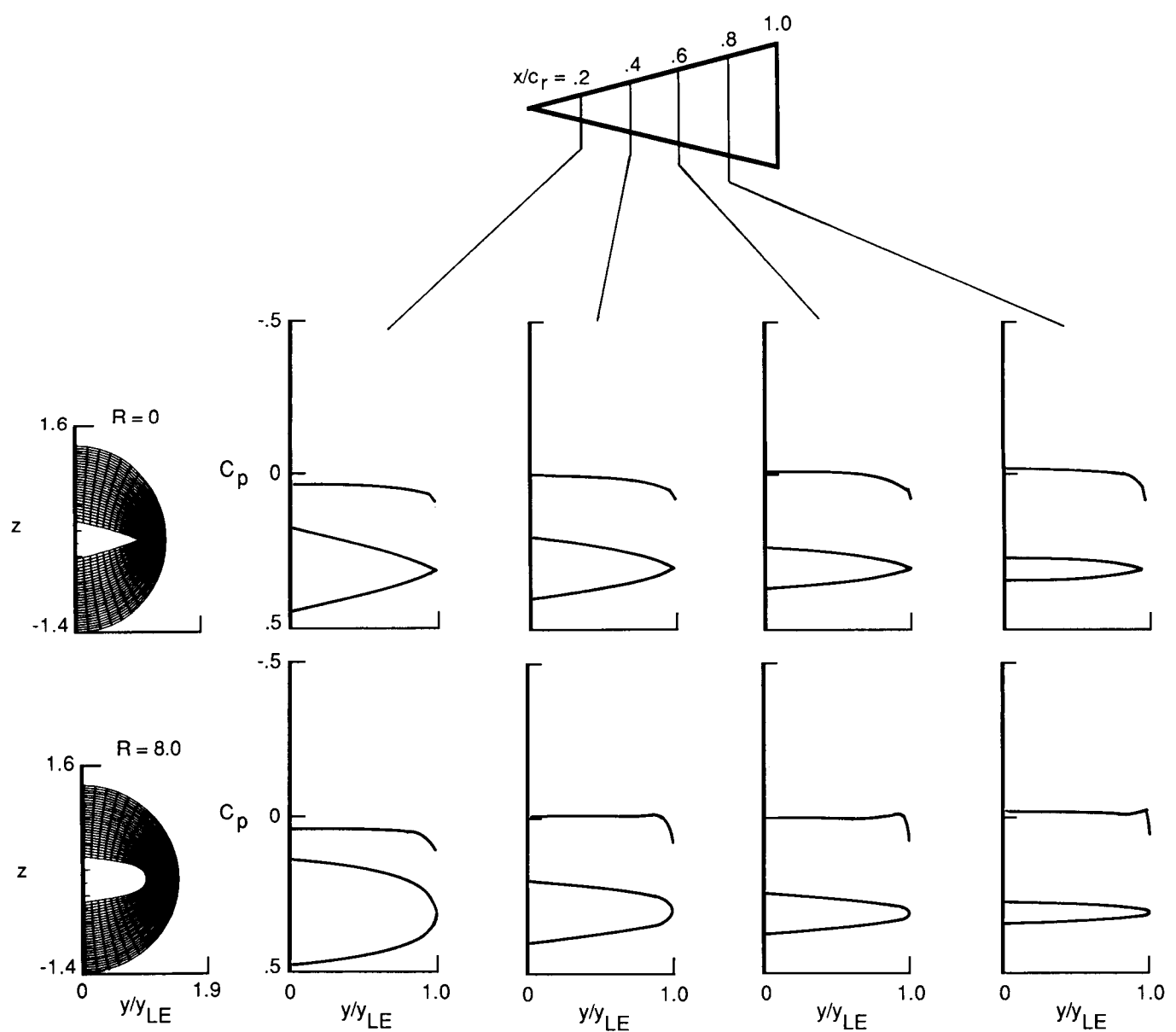


Figure 16. Effect of bluntness on spanwise surface pressure distributions predicted by nonlinear theory for delta wings with $A = 1.0$, $\tau = 0.04$, and $m = 0.5$ at $M = 3.16$.

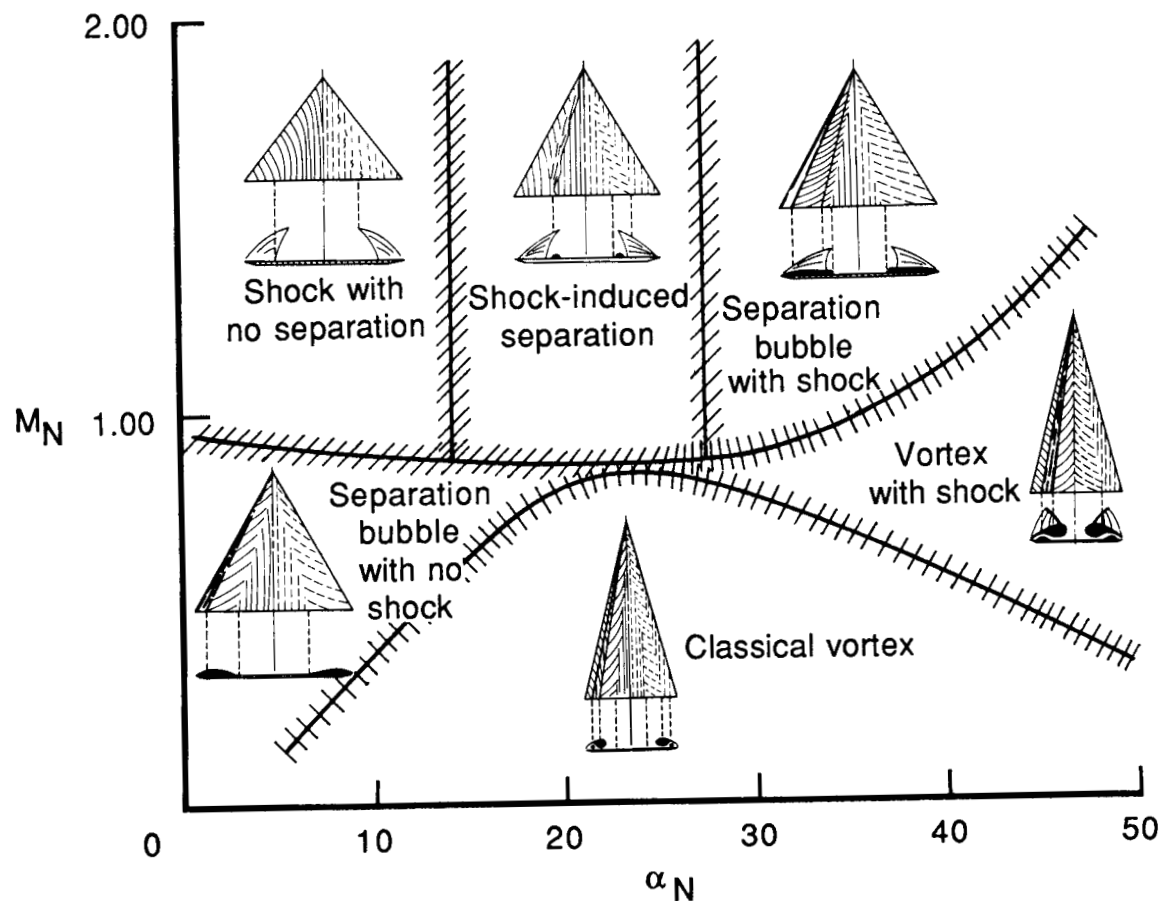


Figure 17. Lee-side flow classification chart for delta wings (ref. 29).

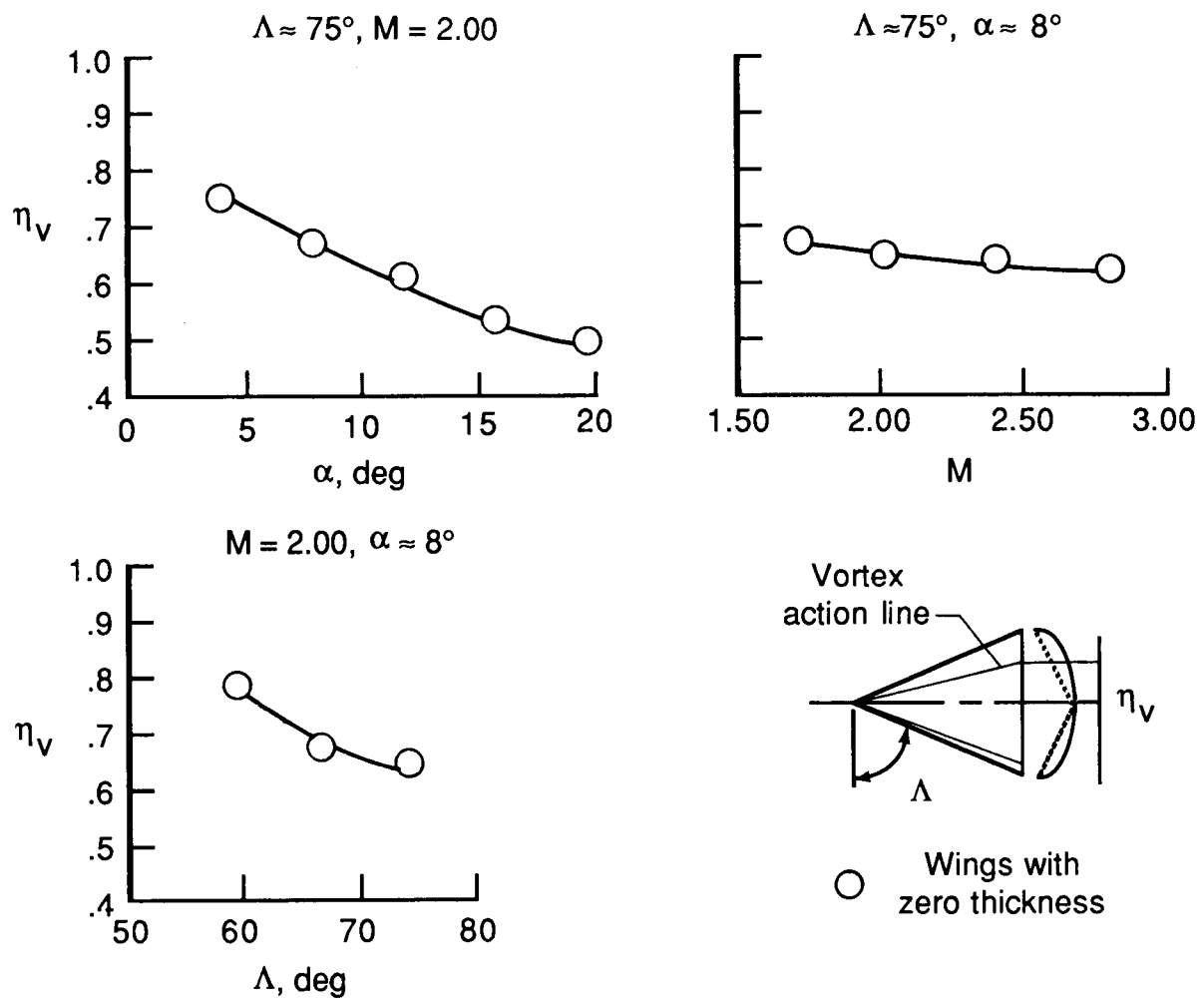


Figure 18. Location of vortex action line for zero-thick delta wings (ref. 31).

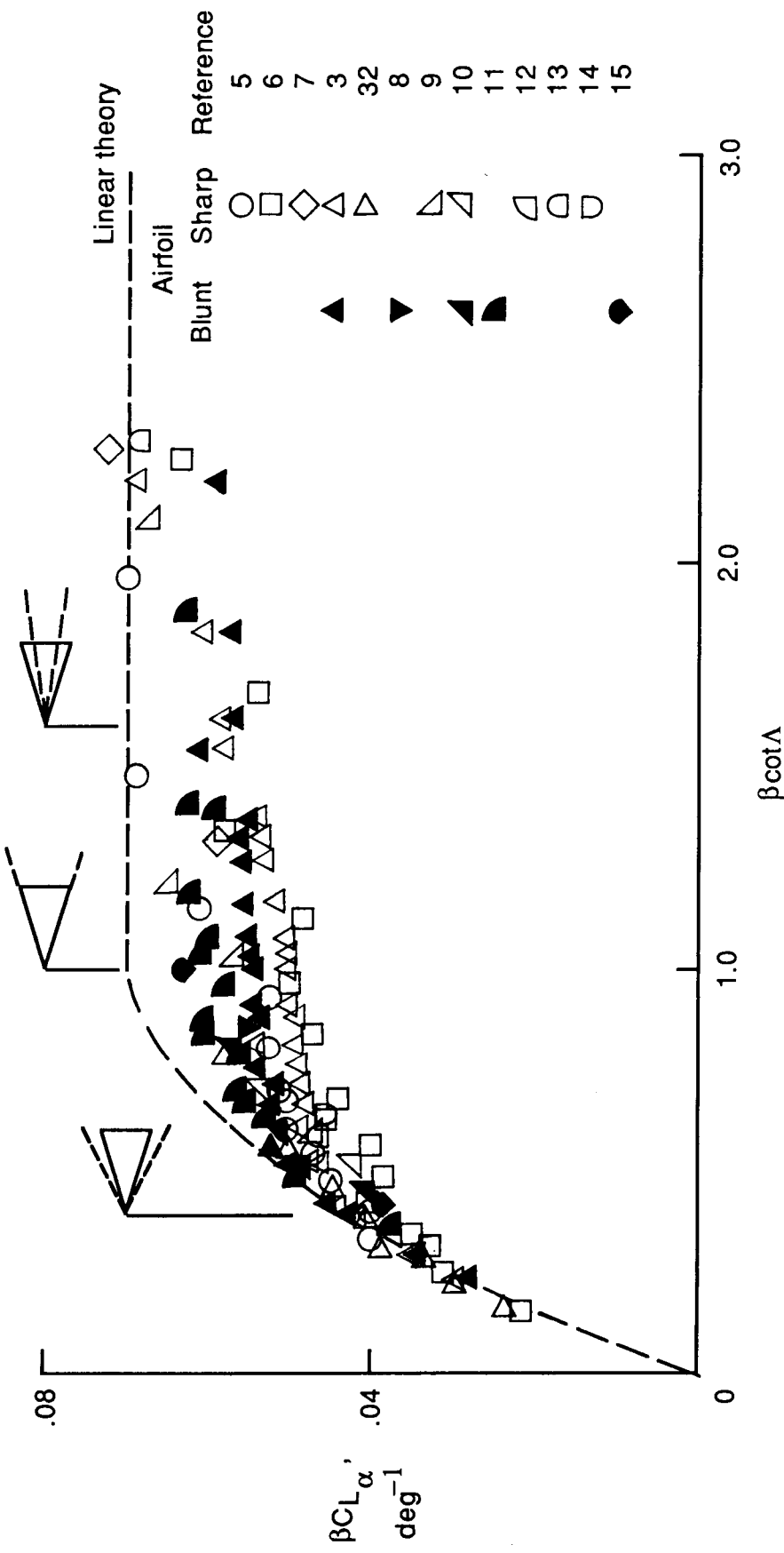


Figure 19. Lift characteristics of thin delta wings.

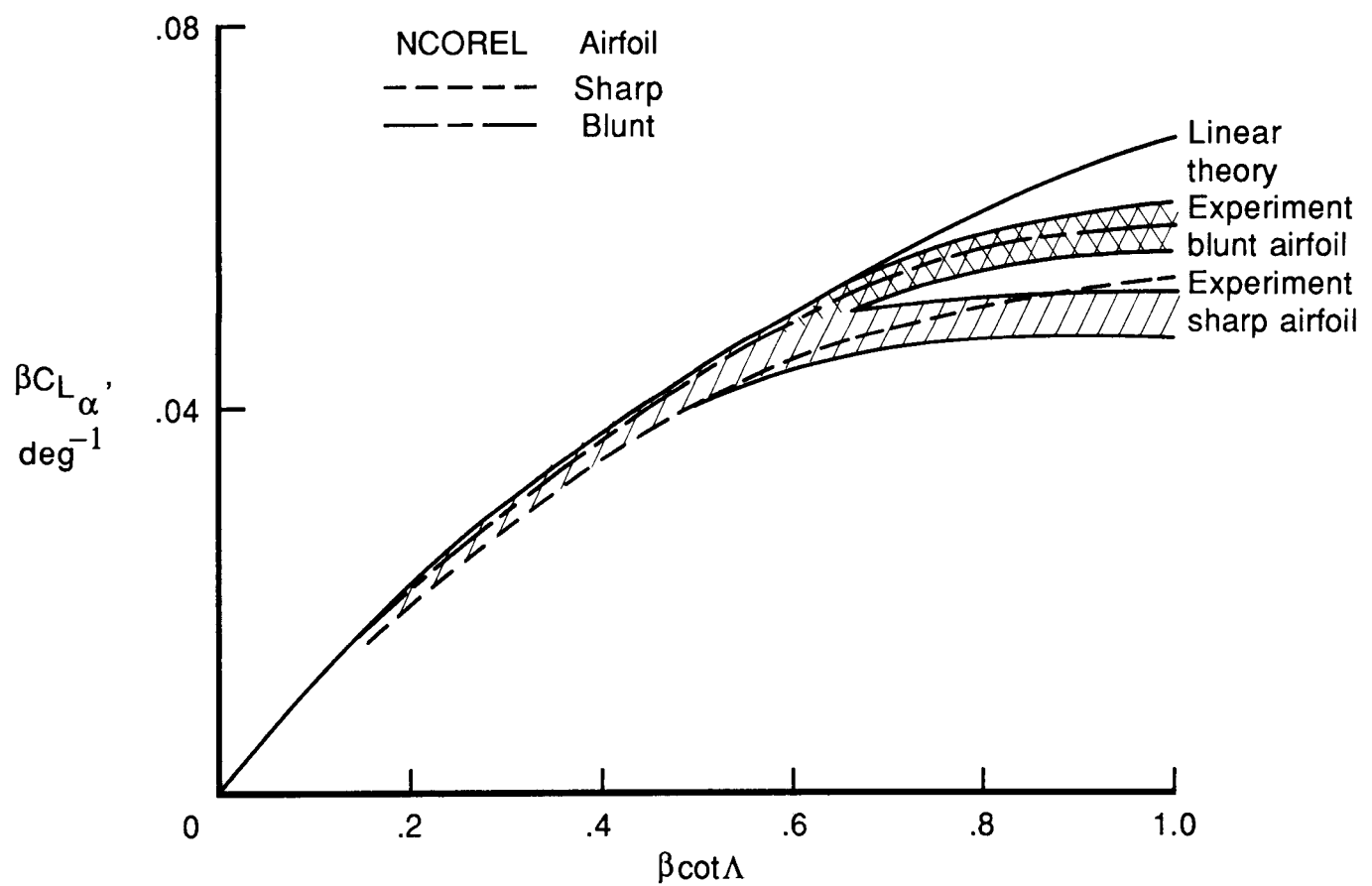


Figure 20. Nonlinear-theory-predicted lift characteristics of thin delta wings.

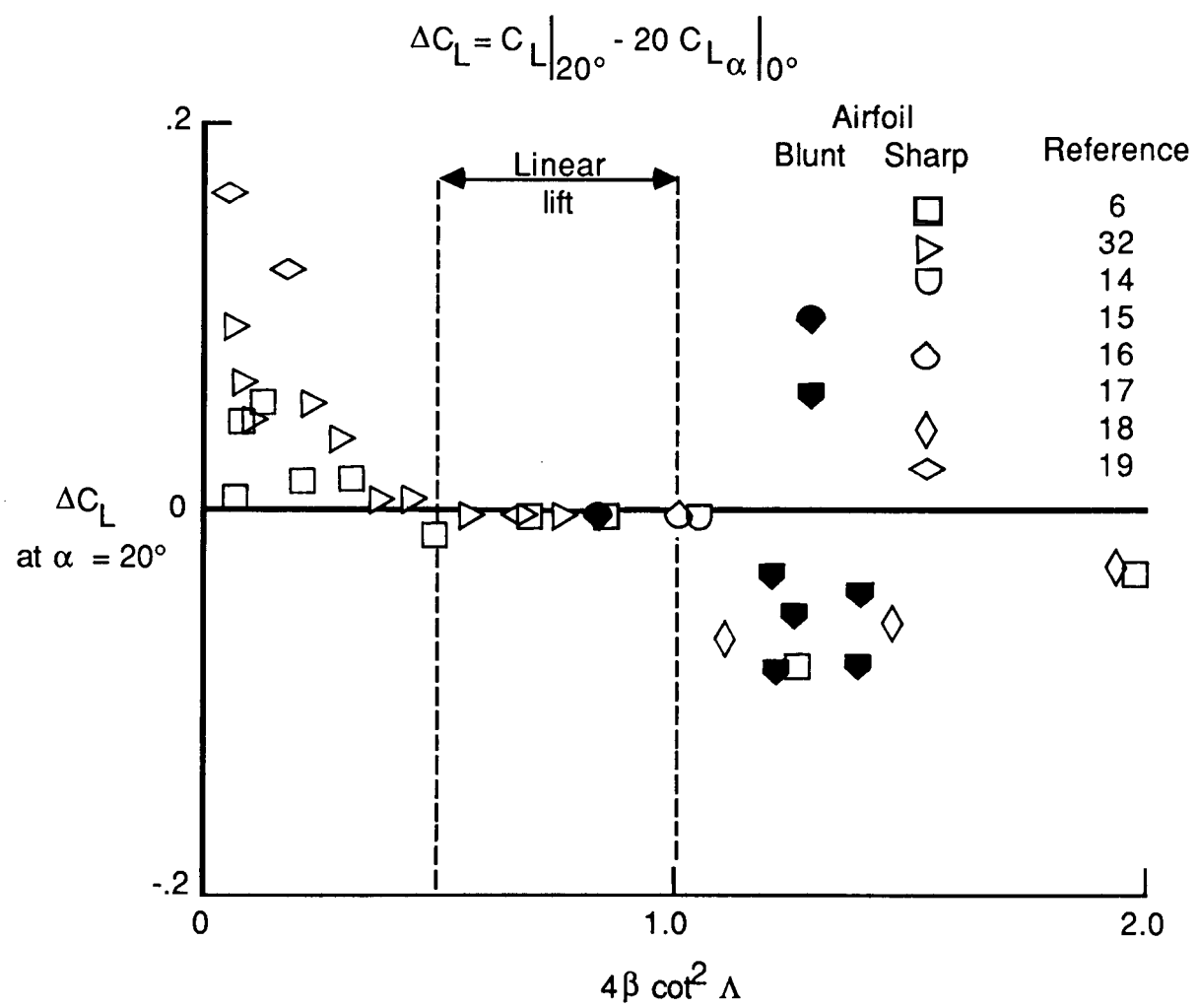


Figure 21. Nonlinear lift effects of thin delta wings.

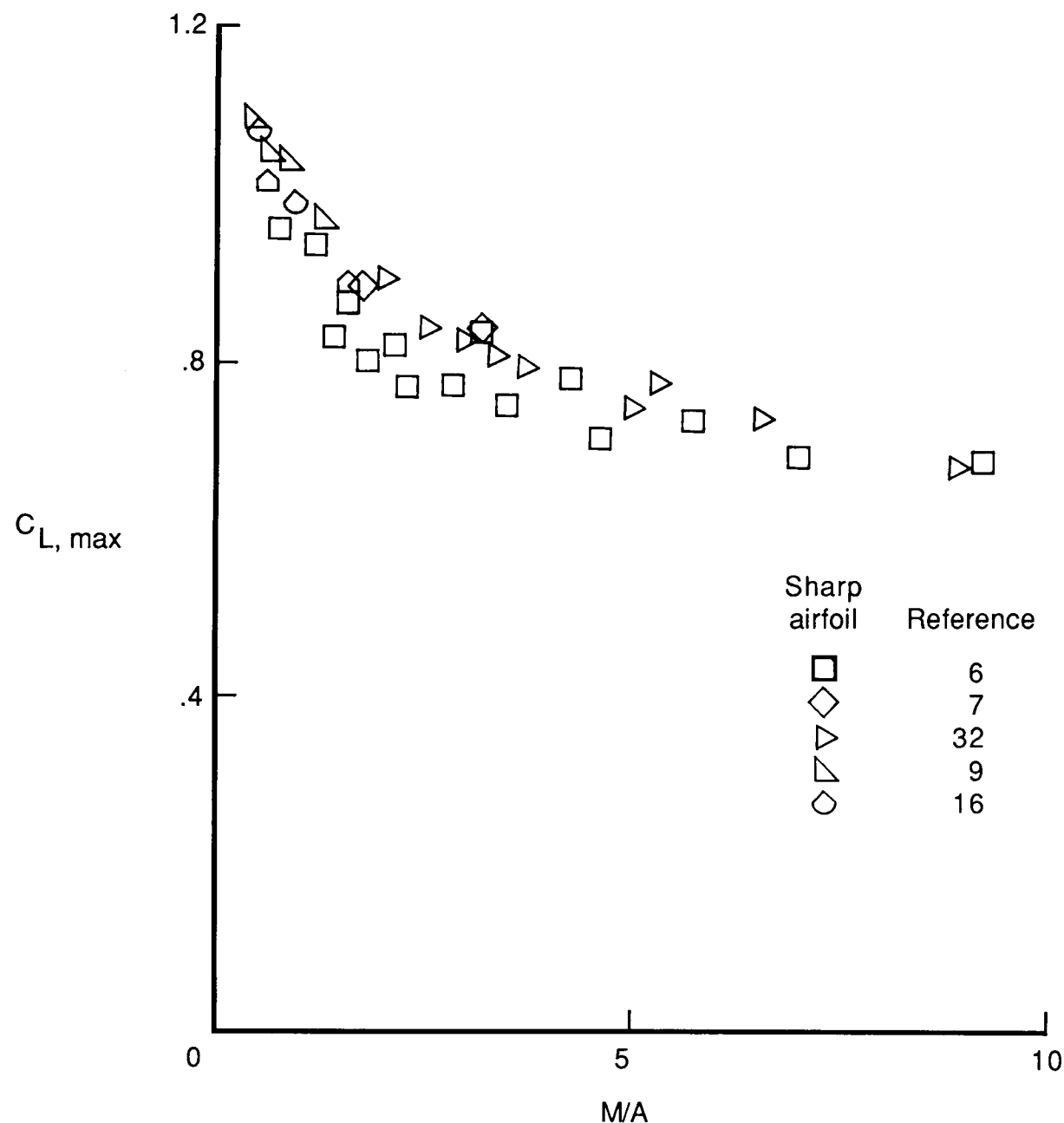


Figure 22. Maximum lift coefficient of thin delta wings.

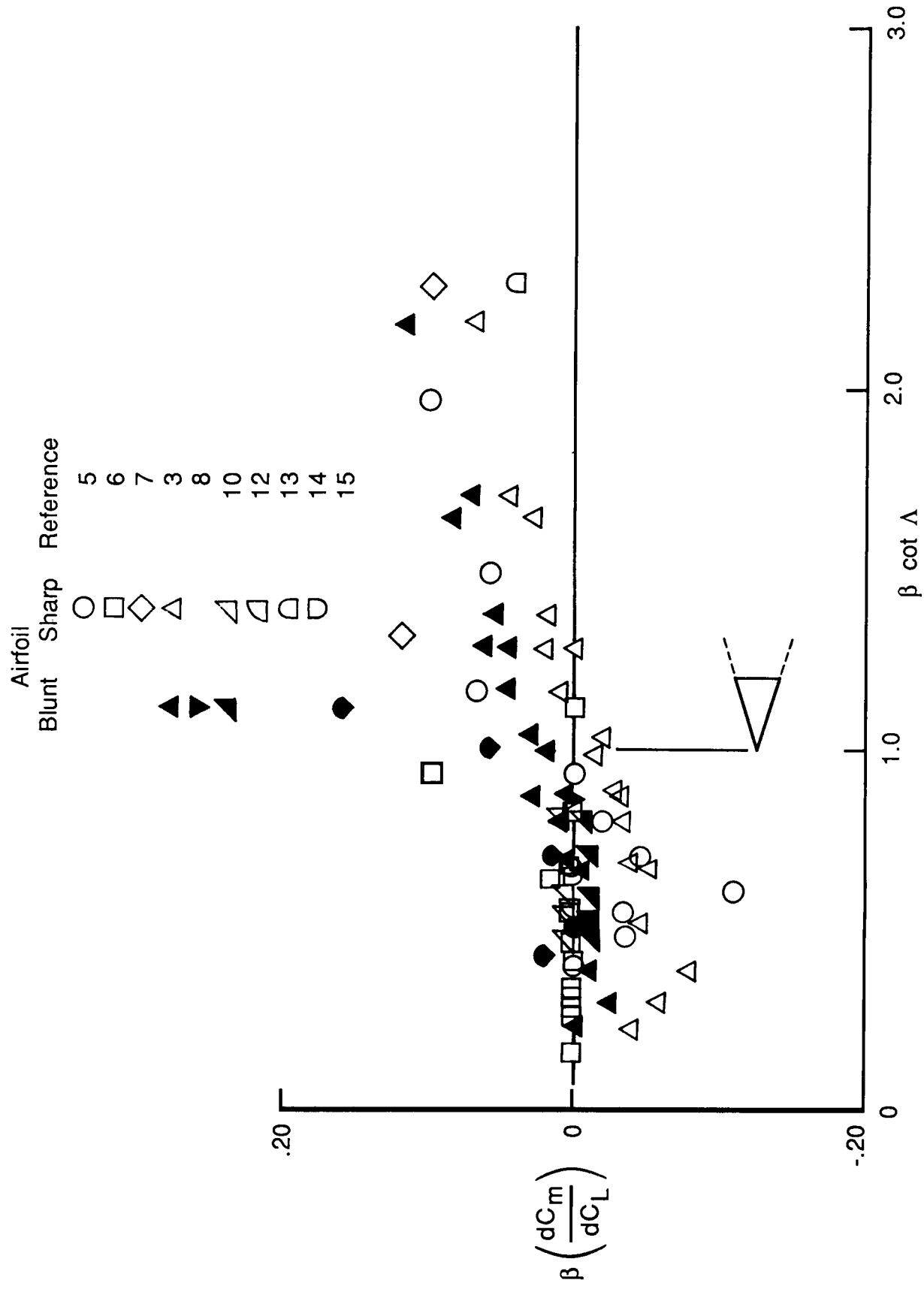


Figure 23. Longitudinal stability level of thin delta wings.

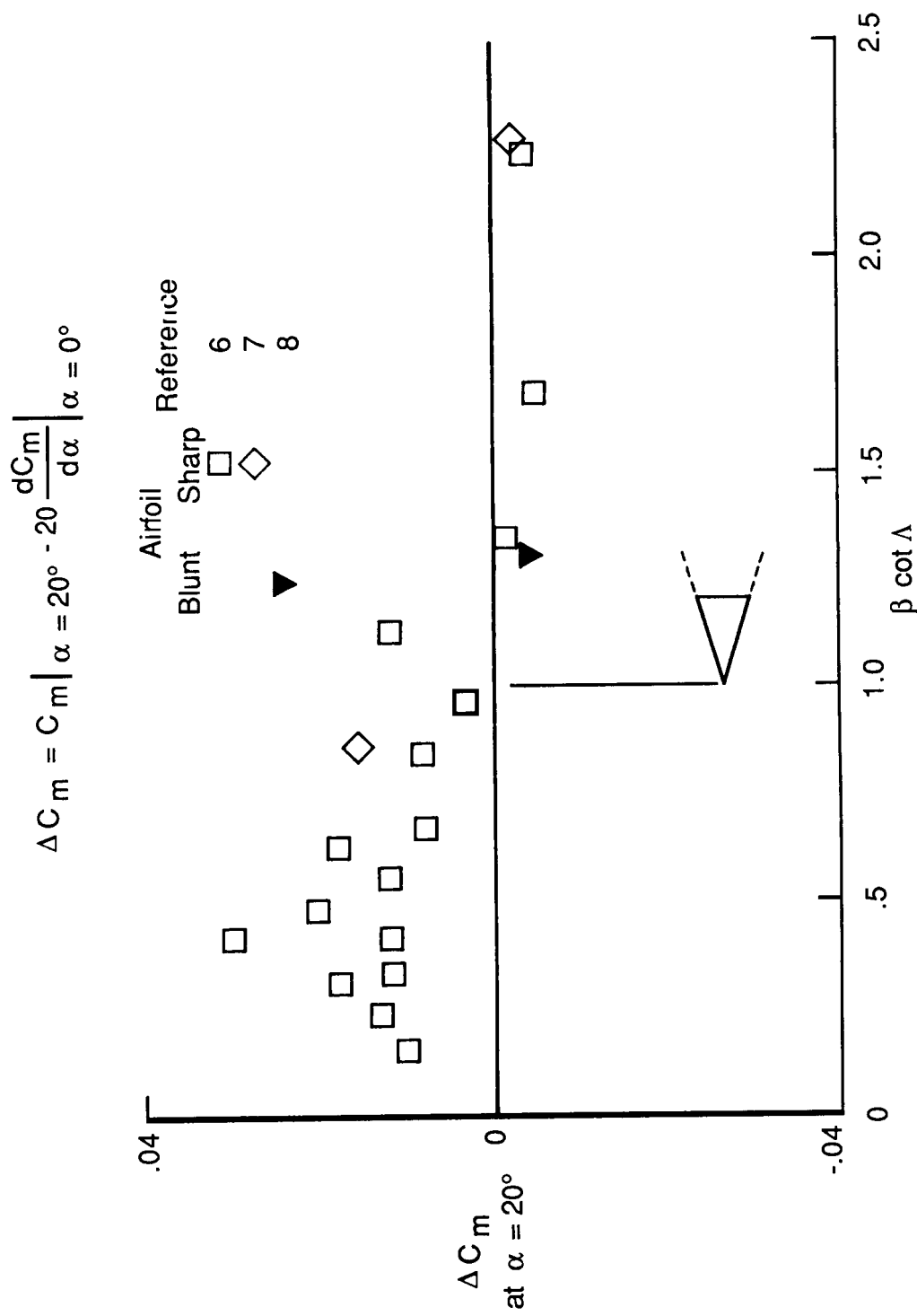
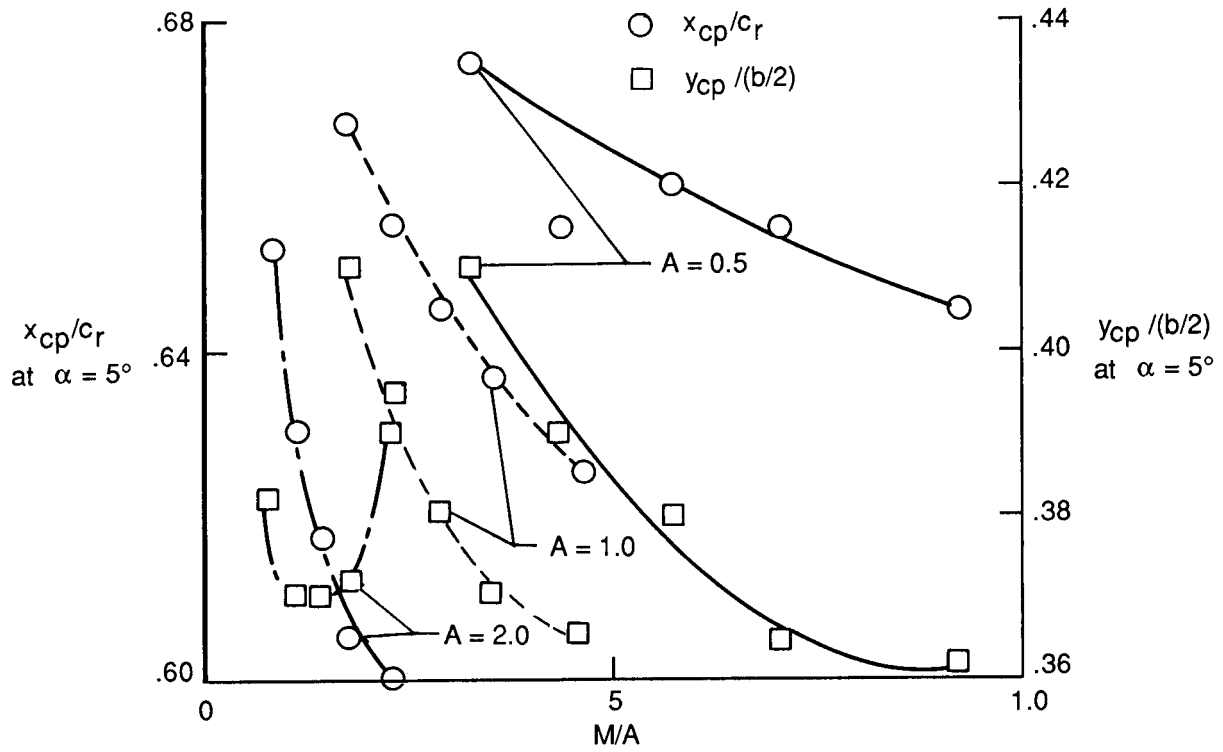
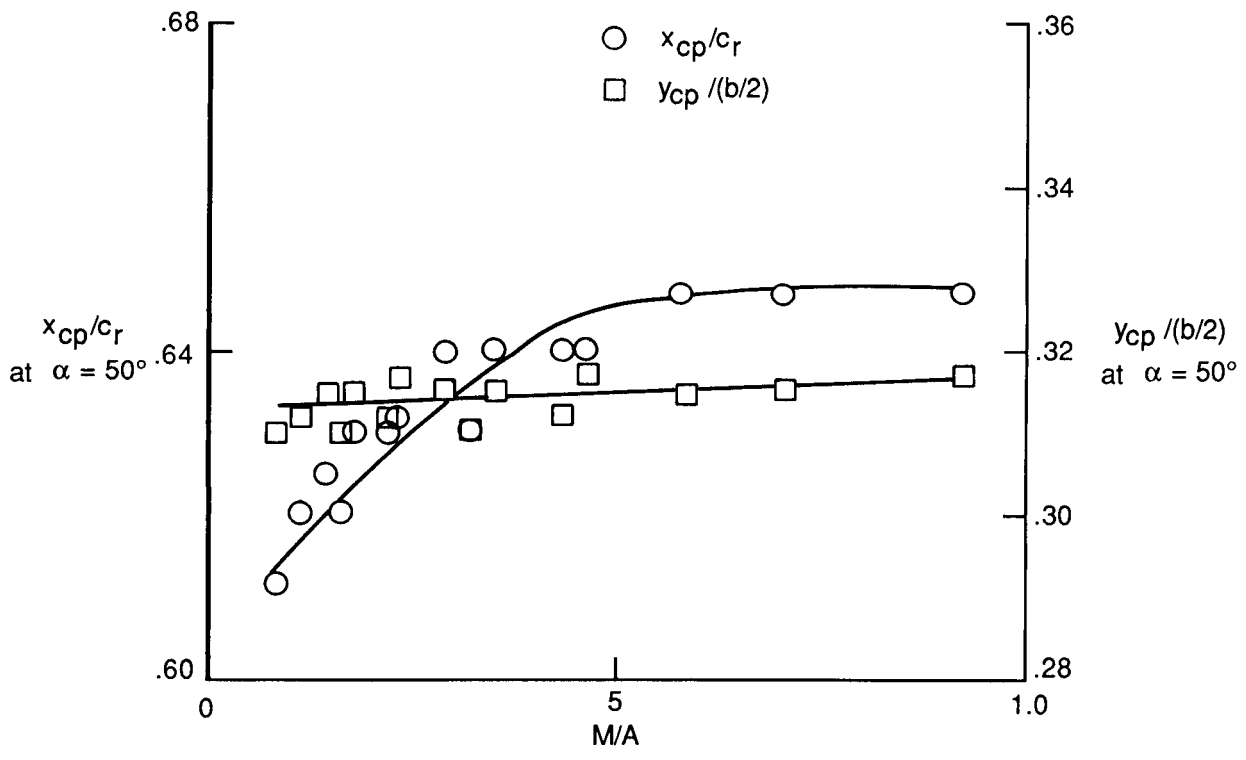


Figure 24. Nonlinear pitching-moment characteristics of thin delta wings.



(a) $\alpha = 5^\circ$.



(b) $\alpha = 50^\circ$.

Figure 25. Wing panel center-of-pressure location for thin delta wings (ref. 6).

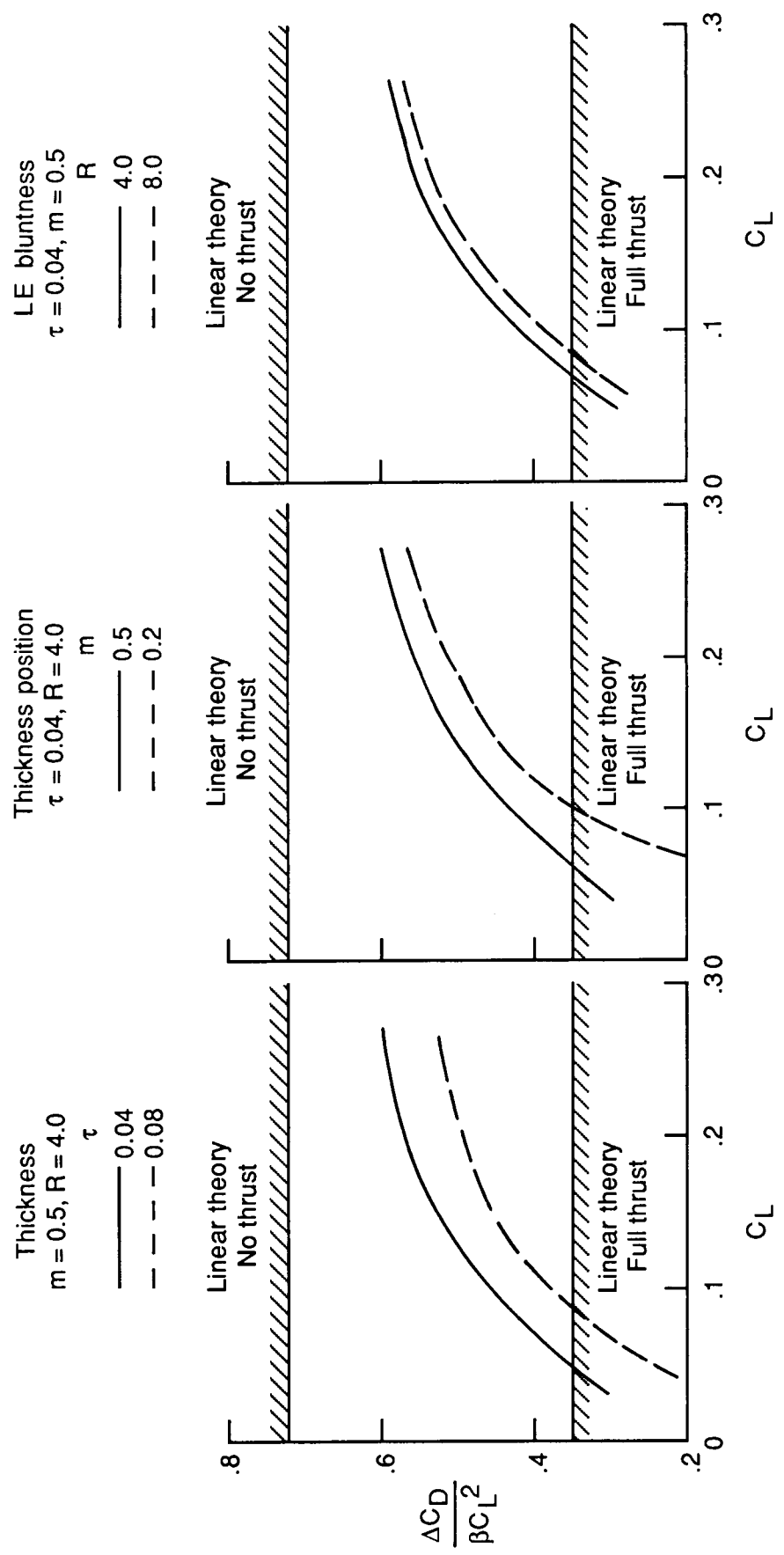


Figure 26. Nonlinear- and linear-theory-predicted drag-due-to-lift characteristics of delta wings with $A = 1.0$ and modified four-digit-series airfoils at $M = 1.41$.

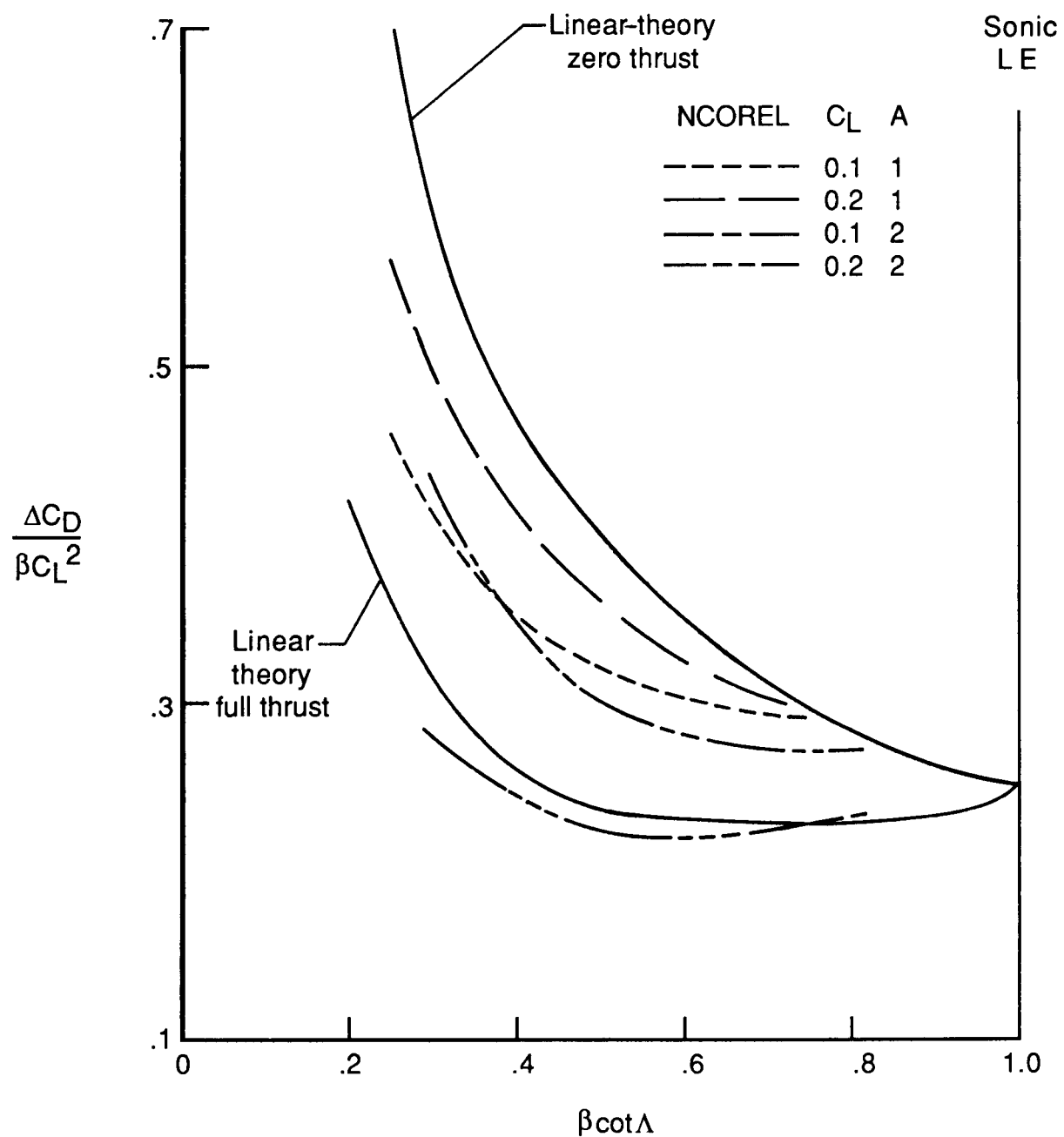
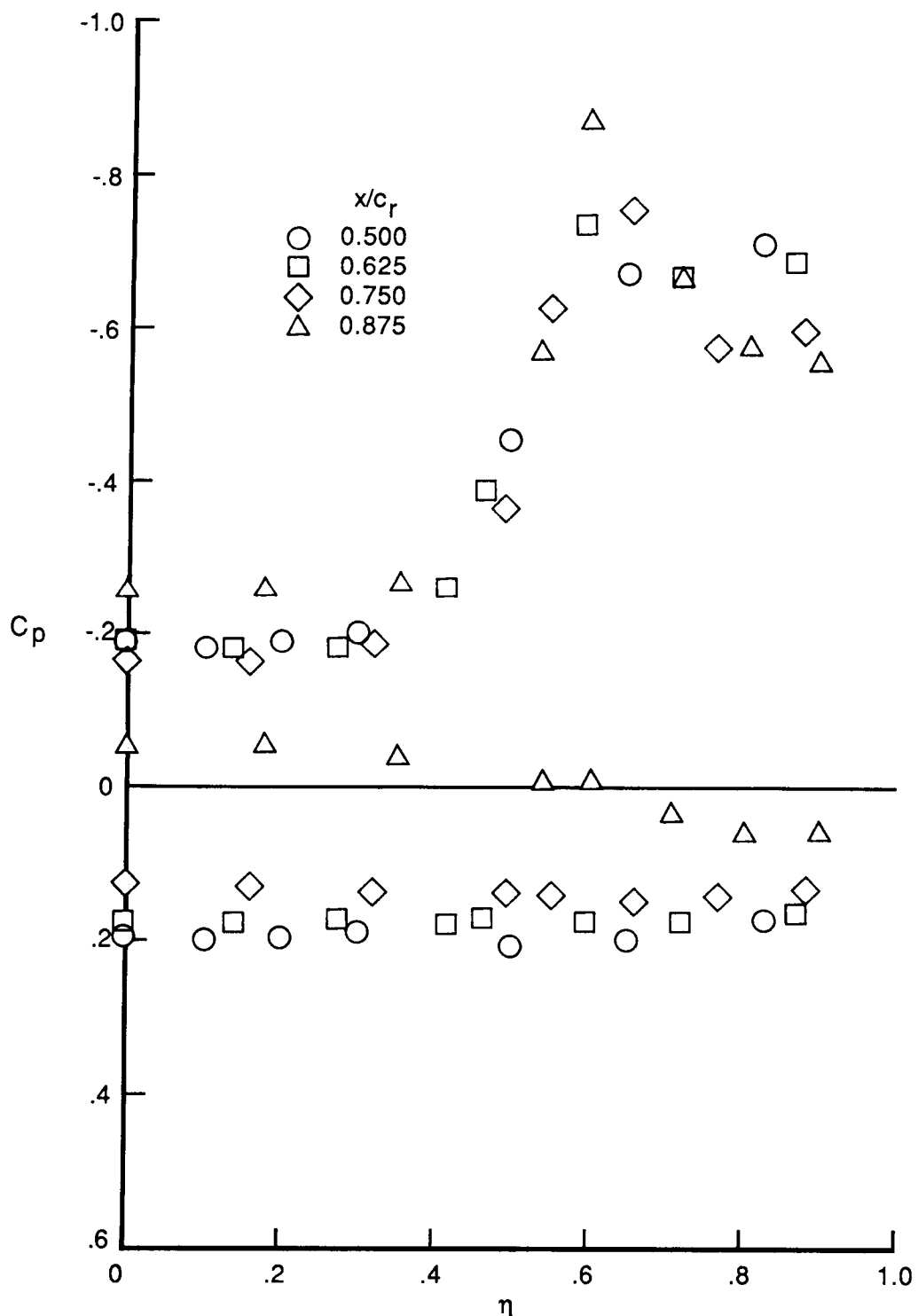
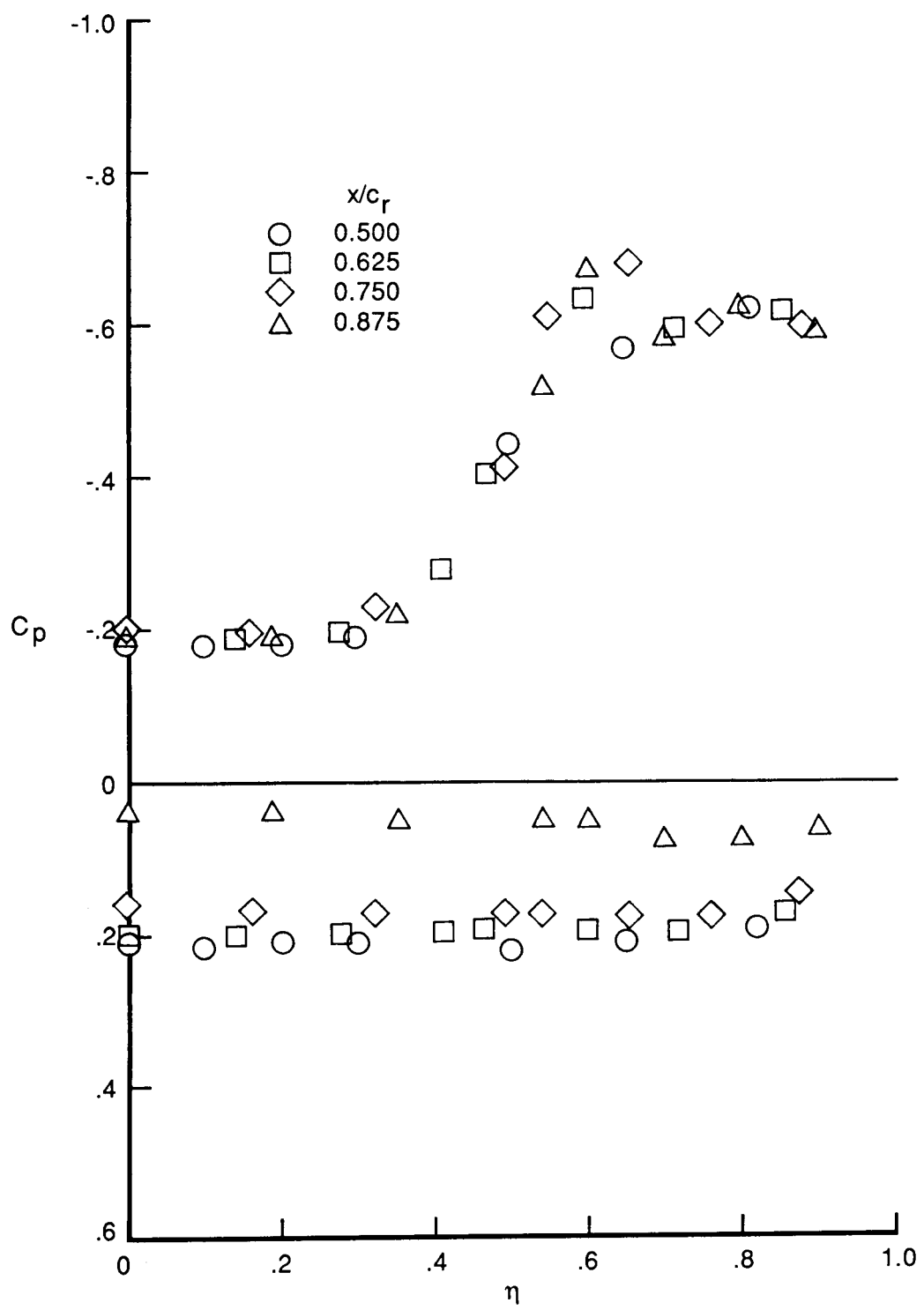


Figure 27. Nonlinear- and linear-theory-predicted drag-due-to-lift characteristics of delta wings.



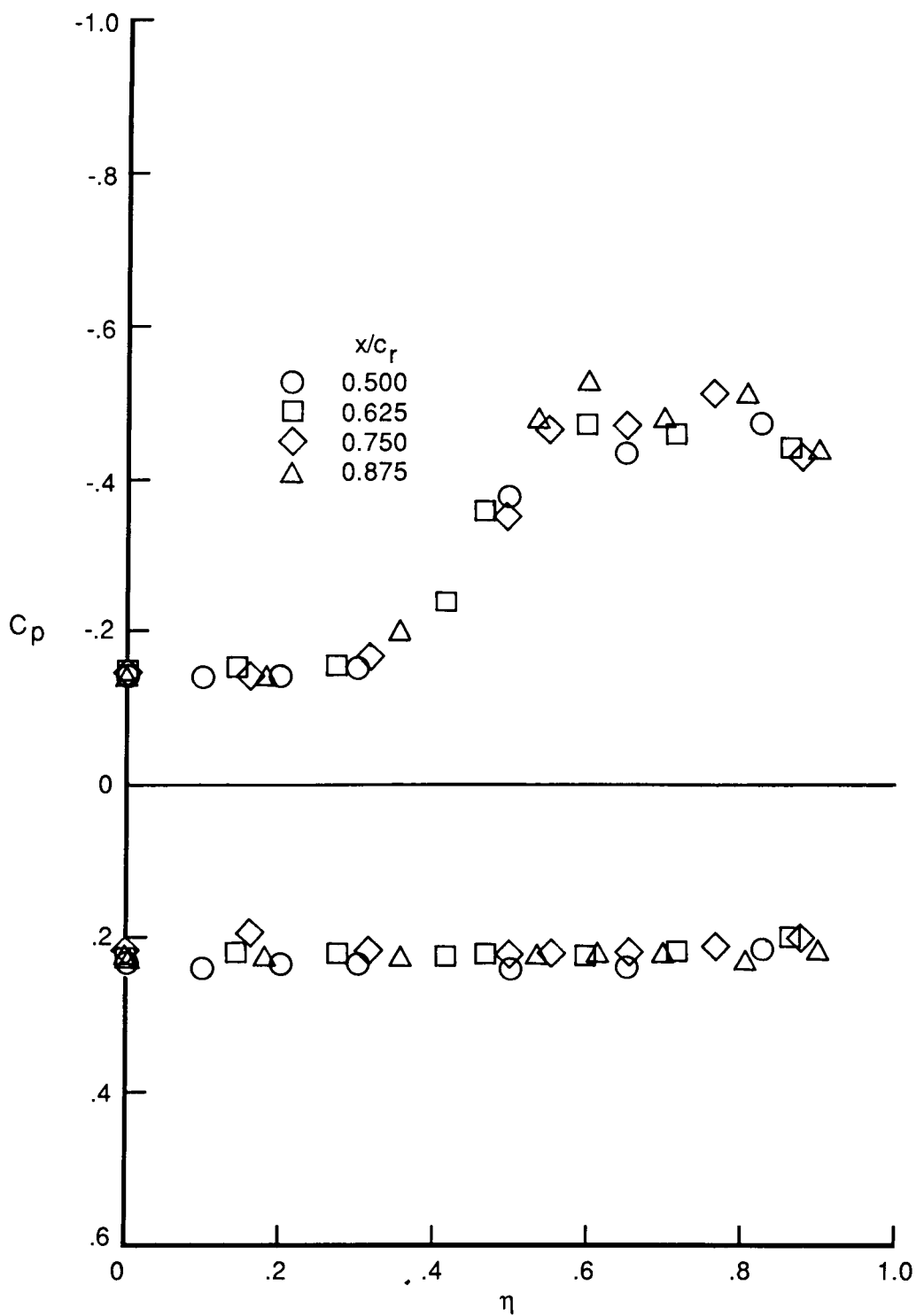
(a) $M = 0.60$ (ref. 19).

Figure 28. Spanwise pressure distributions of delta wing with $A = 1.0$ at $\alpha = 15^\circ$.



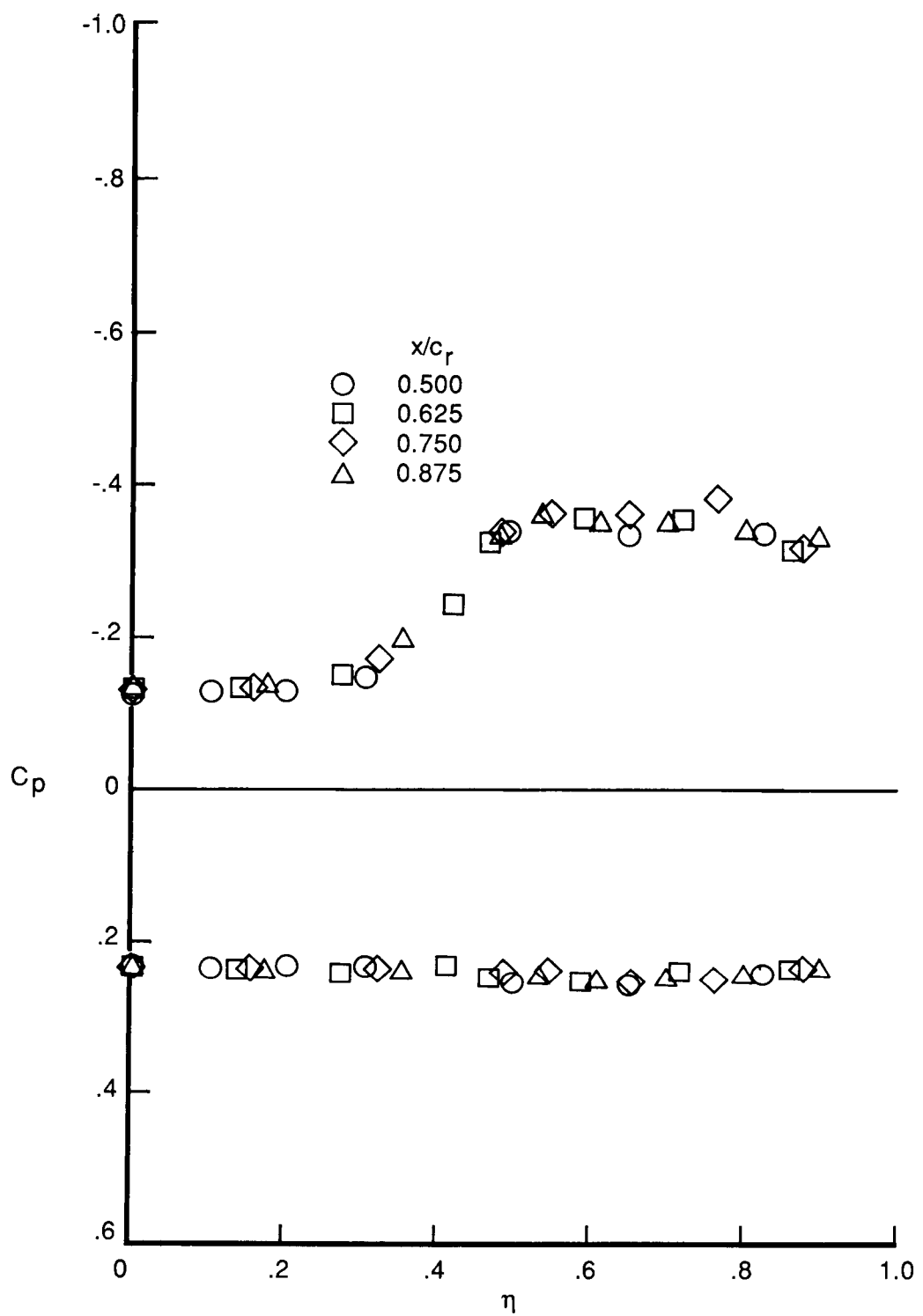
(b) $M = 0.90$ (ref. 19).

Figure 28. Continued.



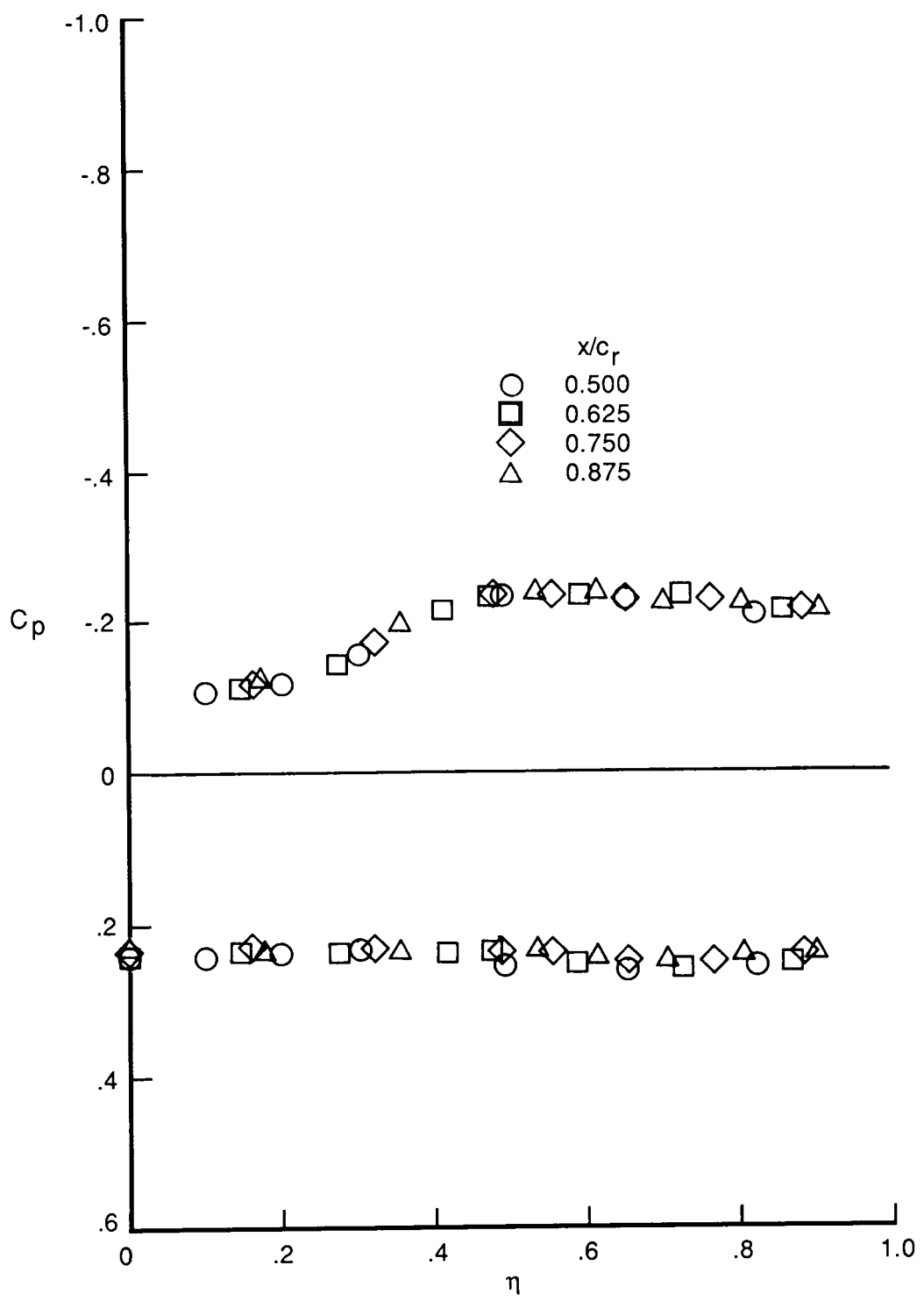
(c) $M = 1.20$ (ref. 19).

Figure 28. Continued.



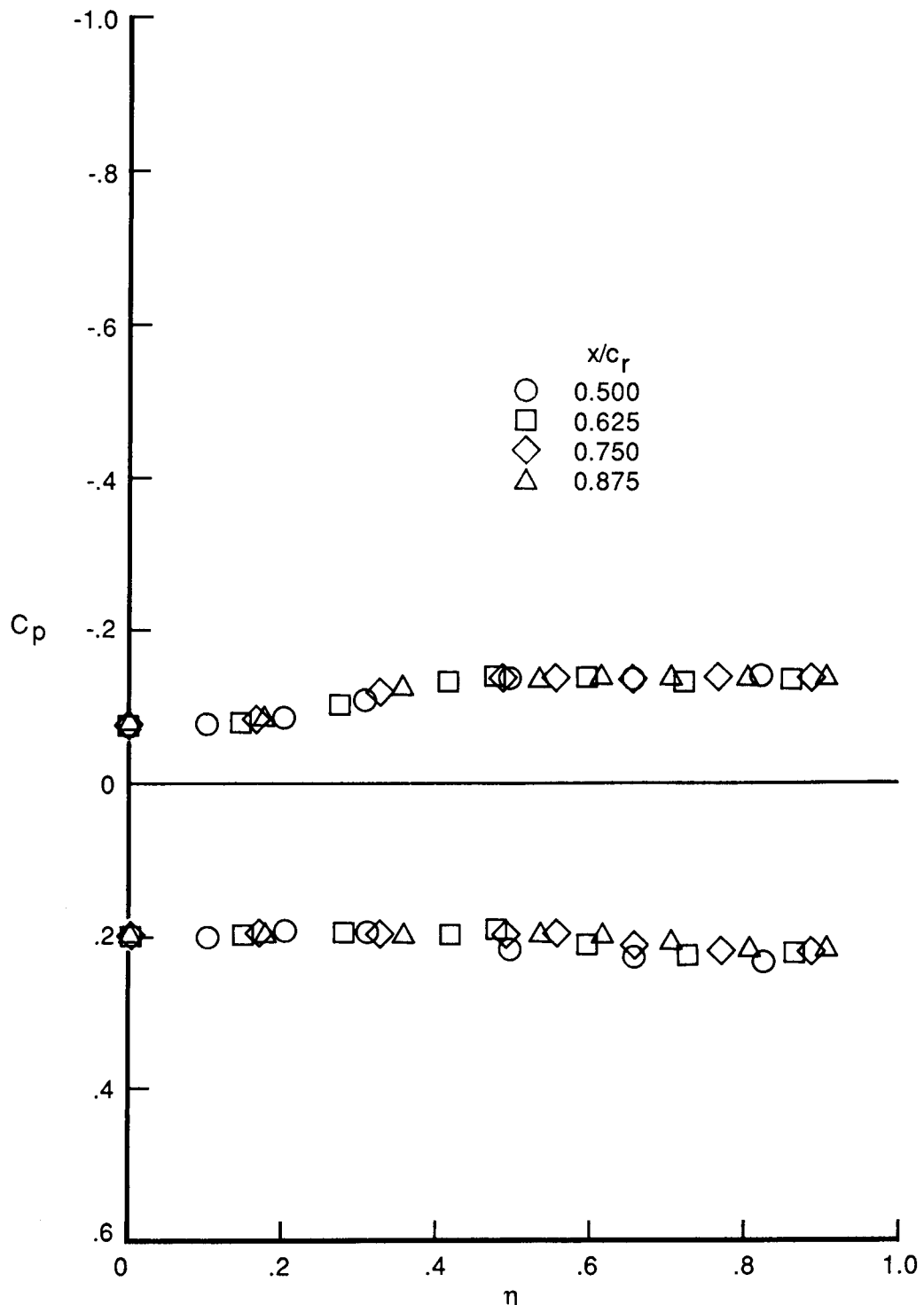
(d) $M = 1.60$ (ref. 6).

Figure 28. Continued.



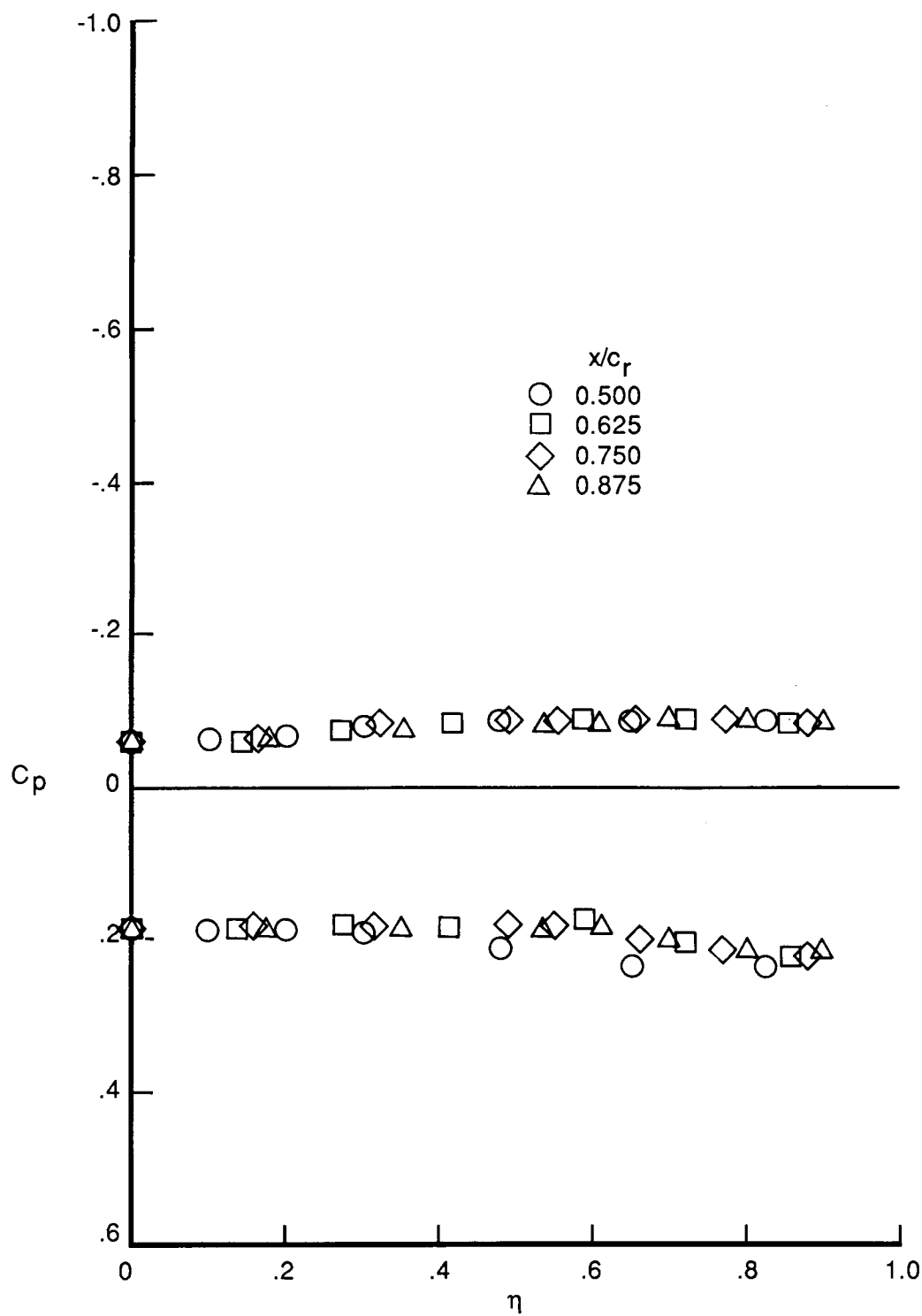
(e) $M = 2.16$ (ref. 6).

Figure 28. Continued.



(f) $M = 2.86$ (ref. 6).

Figure 28. Continued.



(g) $M = 3.50$ (ref. 6).

Figure 28. Concluded.

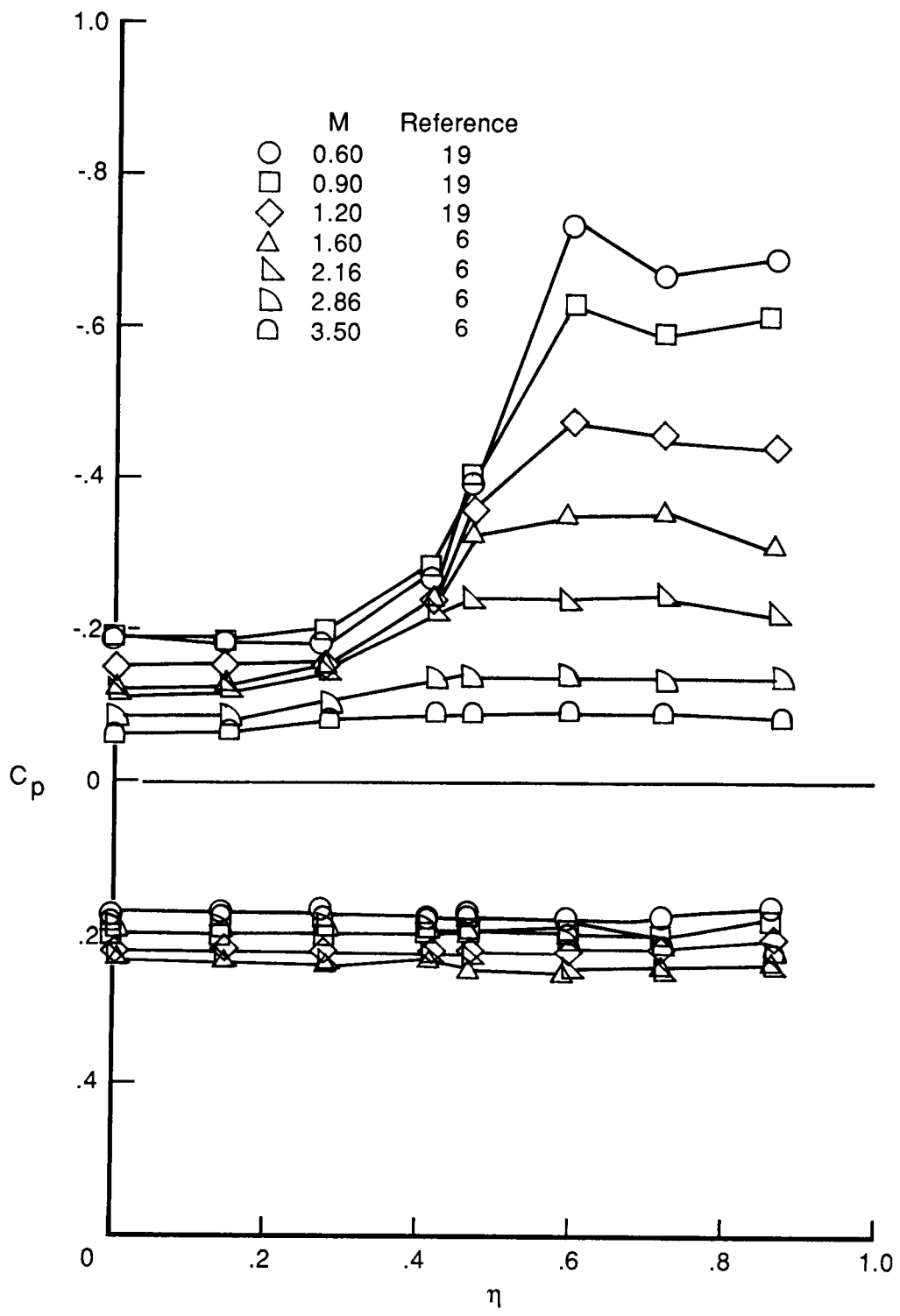


Figure 29. Effect of Mach number on spanwise pressure distributions of delta wing with $A = 1.0$ at $\alpha = 15^\circ$ and $x/c_r = 0.625$.

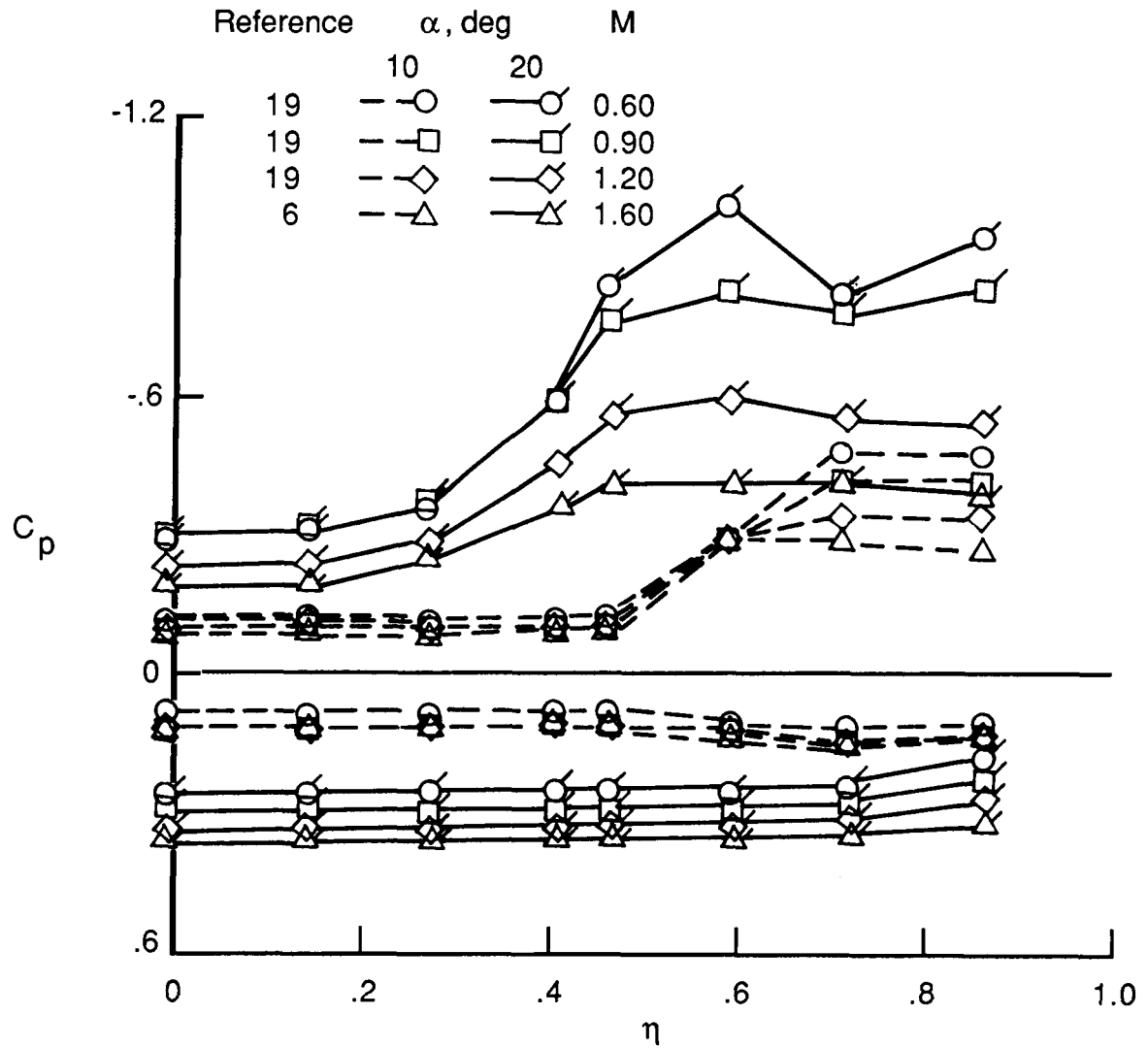


Figure 30. Effect of angle of attack on spanwise surface pressure distributions of delta wing with $A = 1.0$ for $x/c_r = 0.625$.

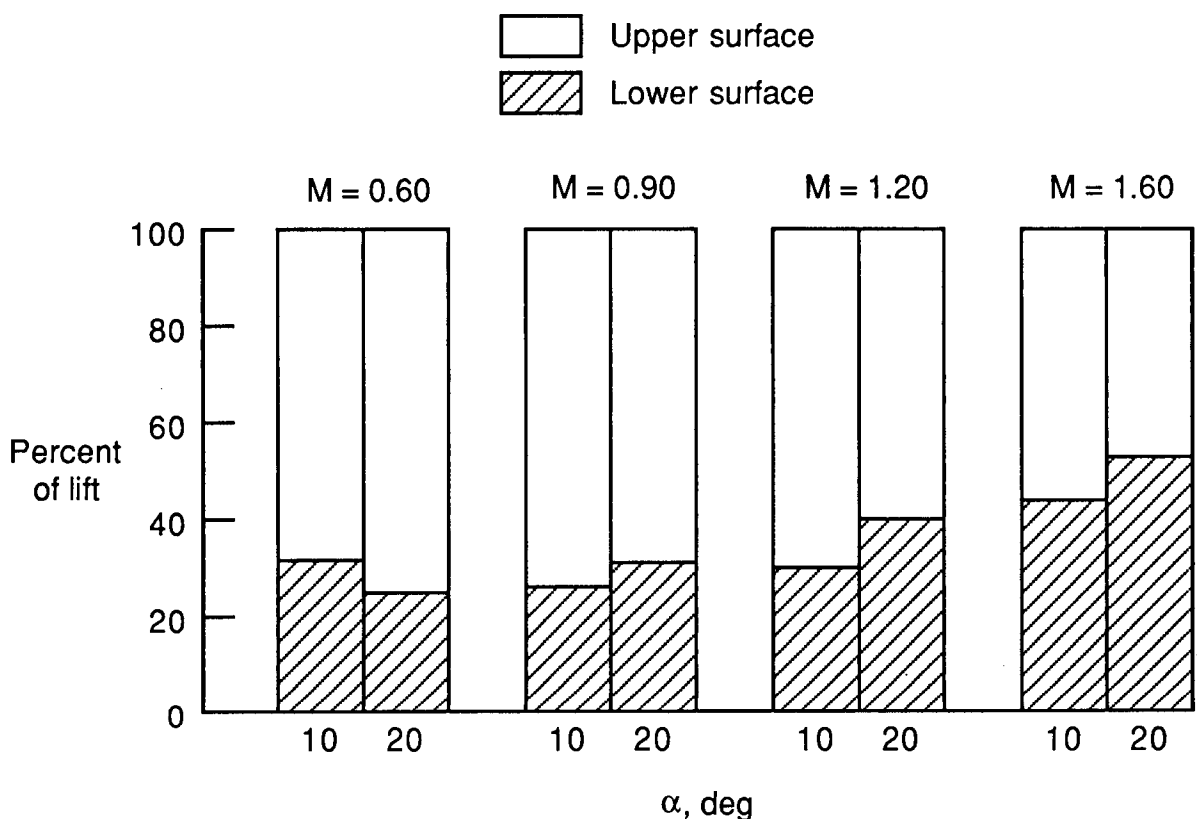
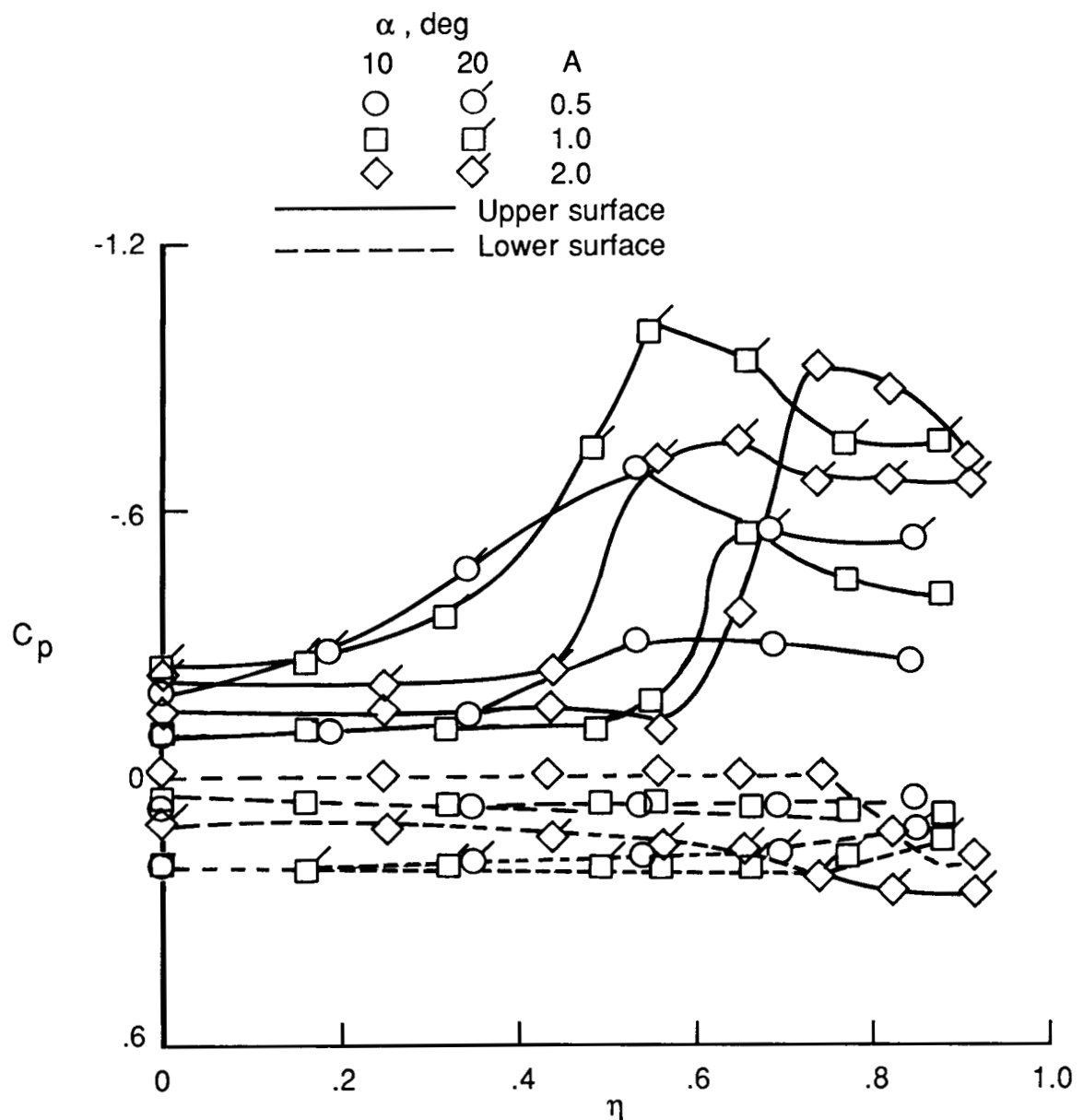
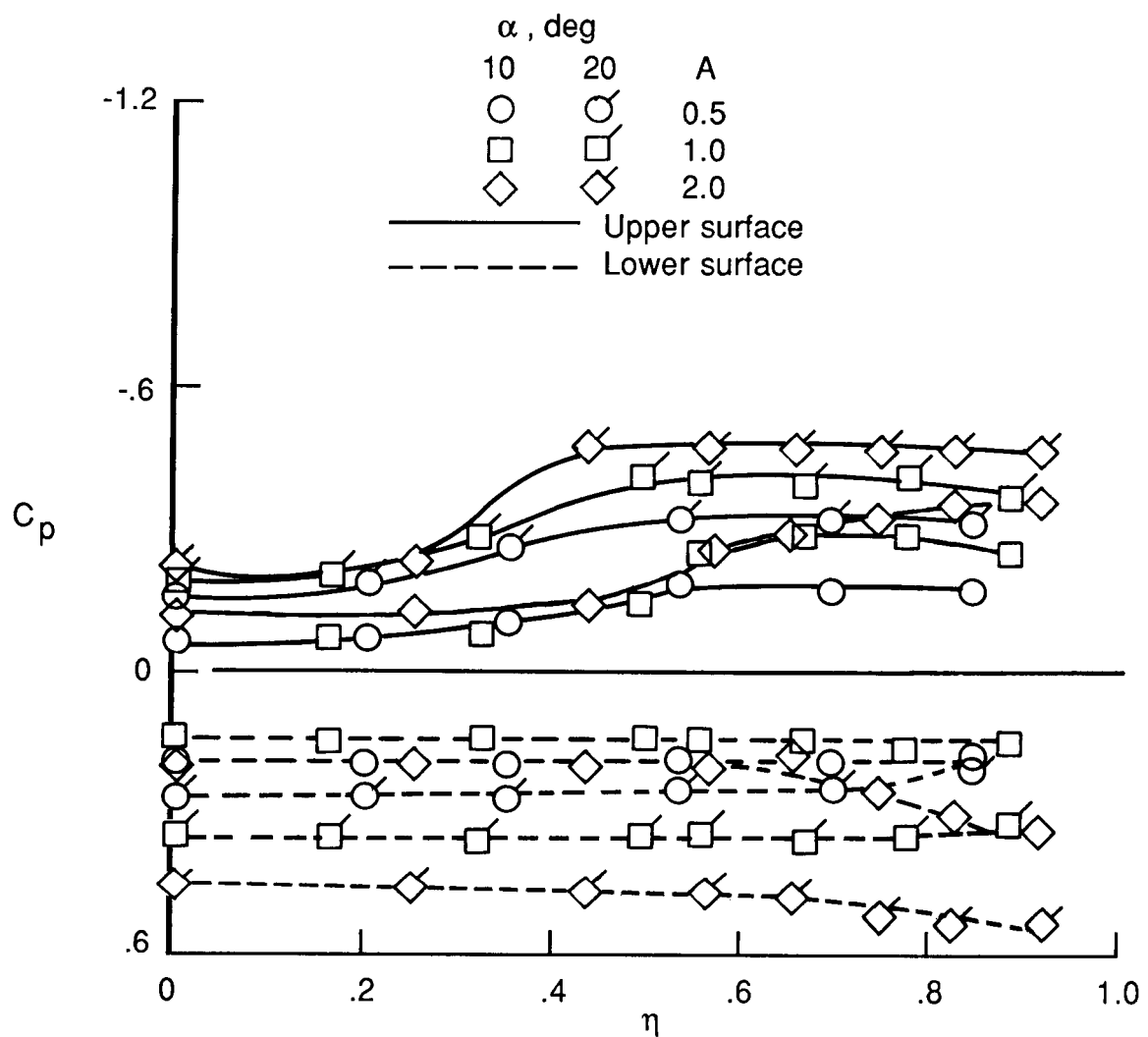


Figure 31. Distribution of lift for delta wing with $A = 10$.



(a) $M = 0.60$ (ref. 19).

Figure 32. Effect of A on spanwise surface pressure distributions of delta wings at $x/c_r = 0.750$.



(b) $M = 1.60$ (ref. 6).

Figure 32. Concluded.

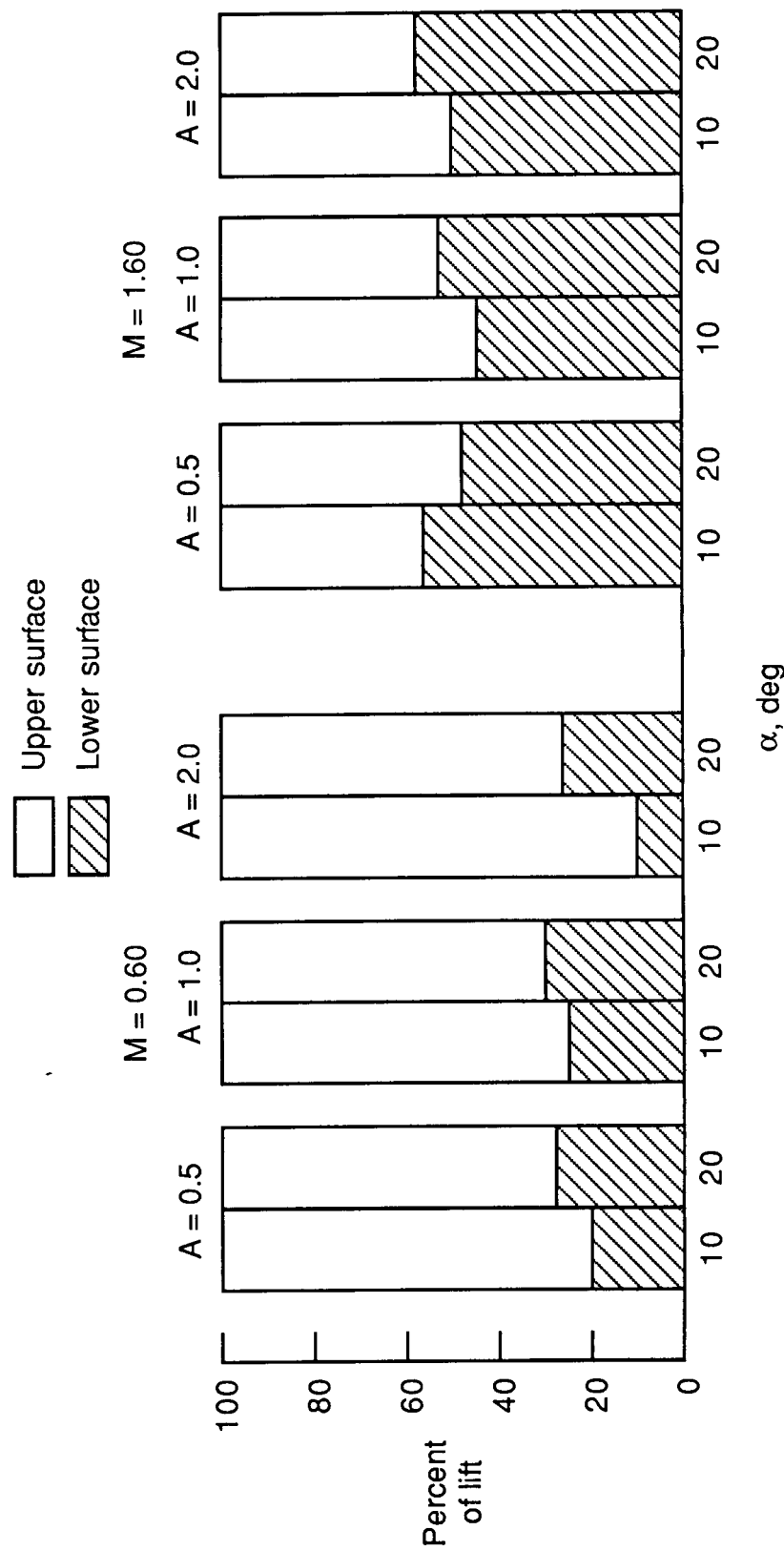
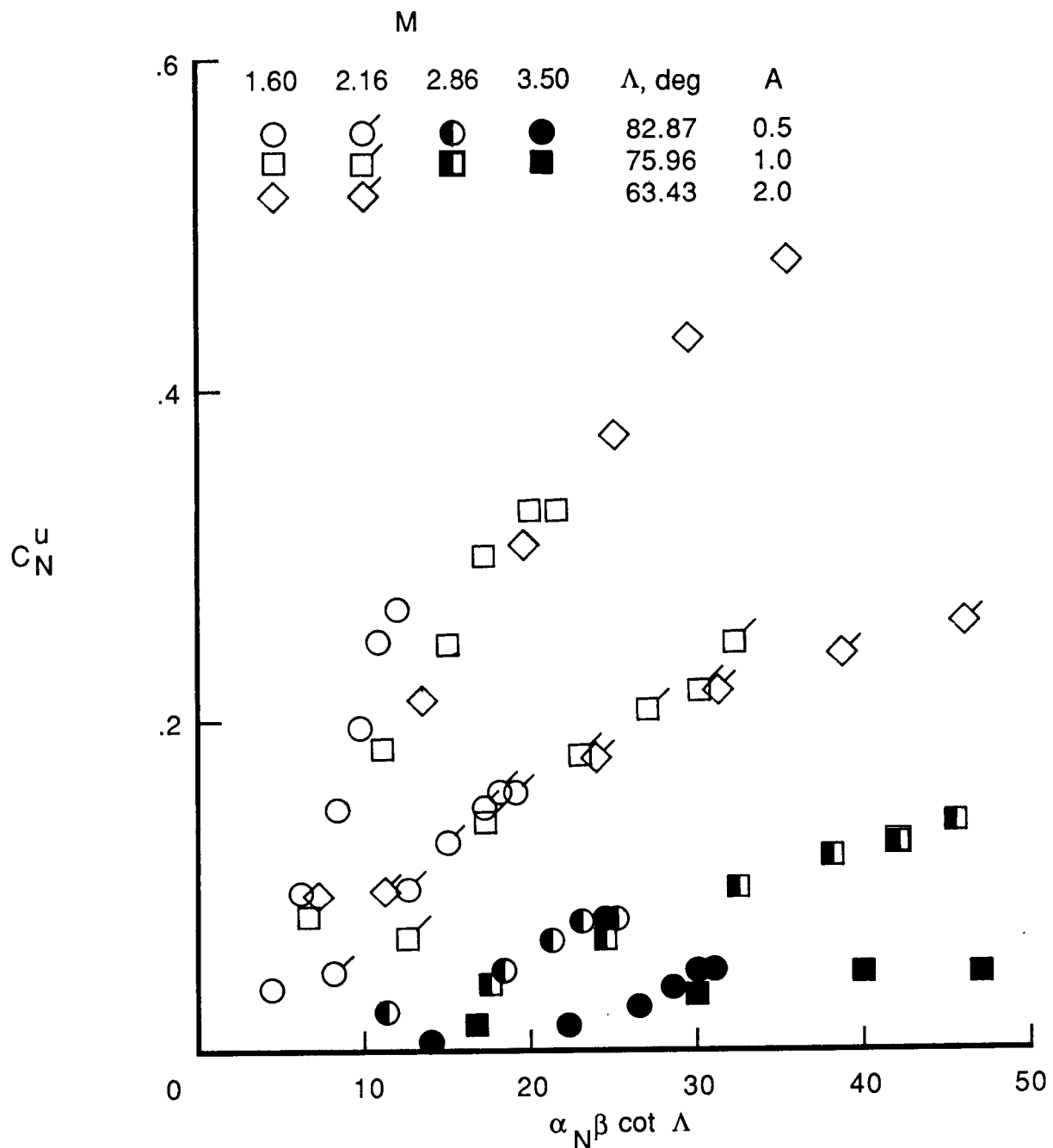
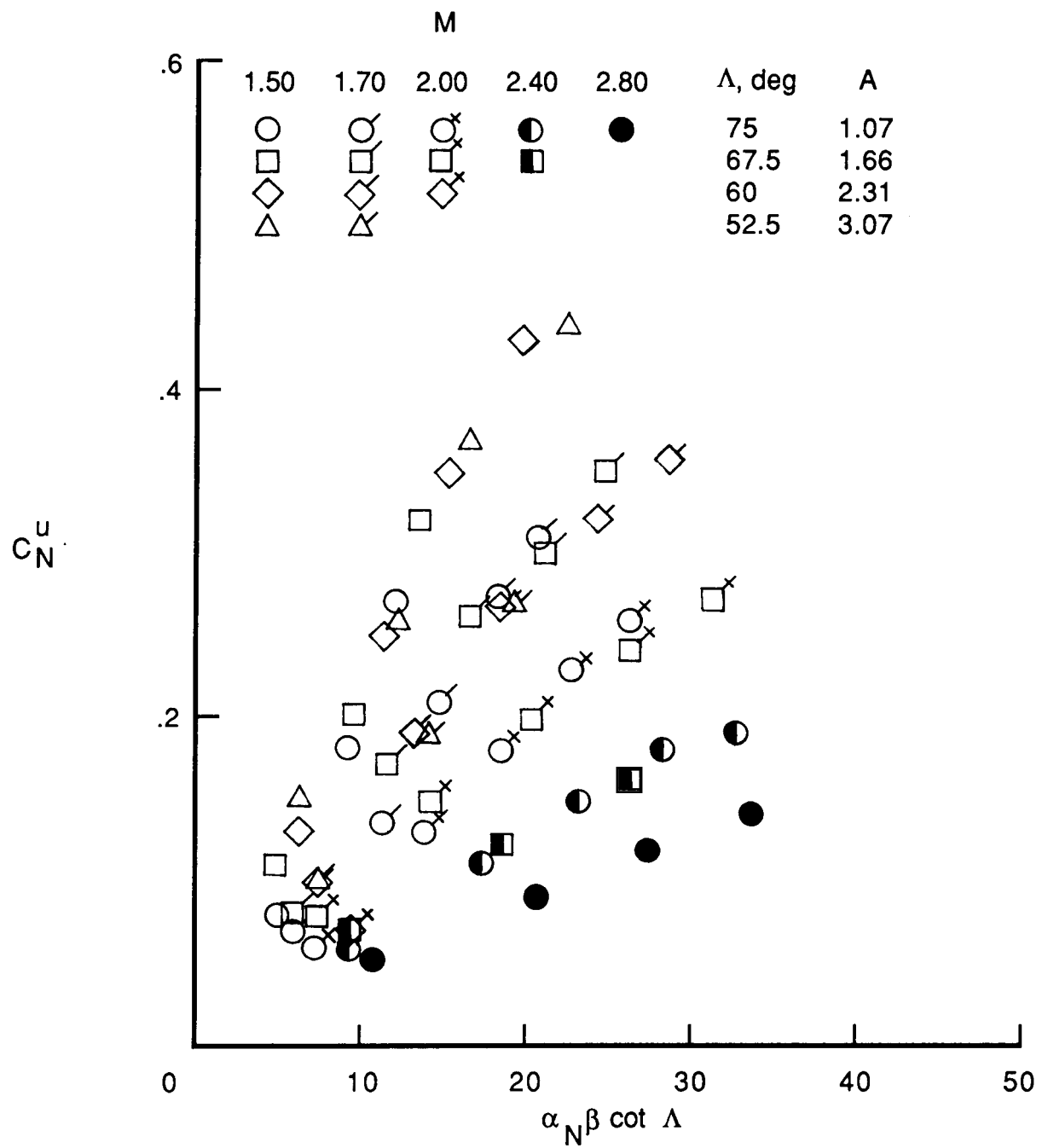


Figure 33. Effect of M and A on the distribution of lift for delta wings.



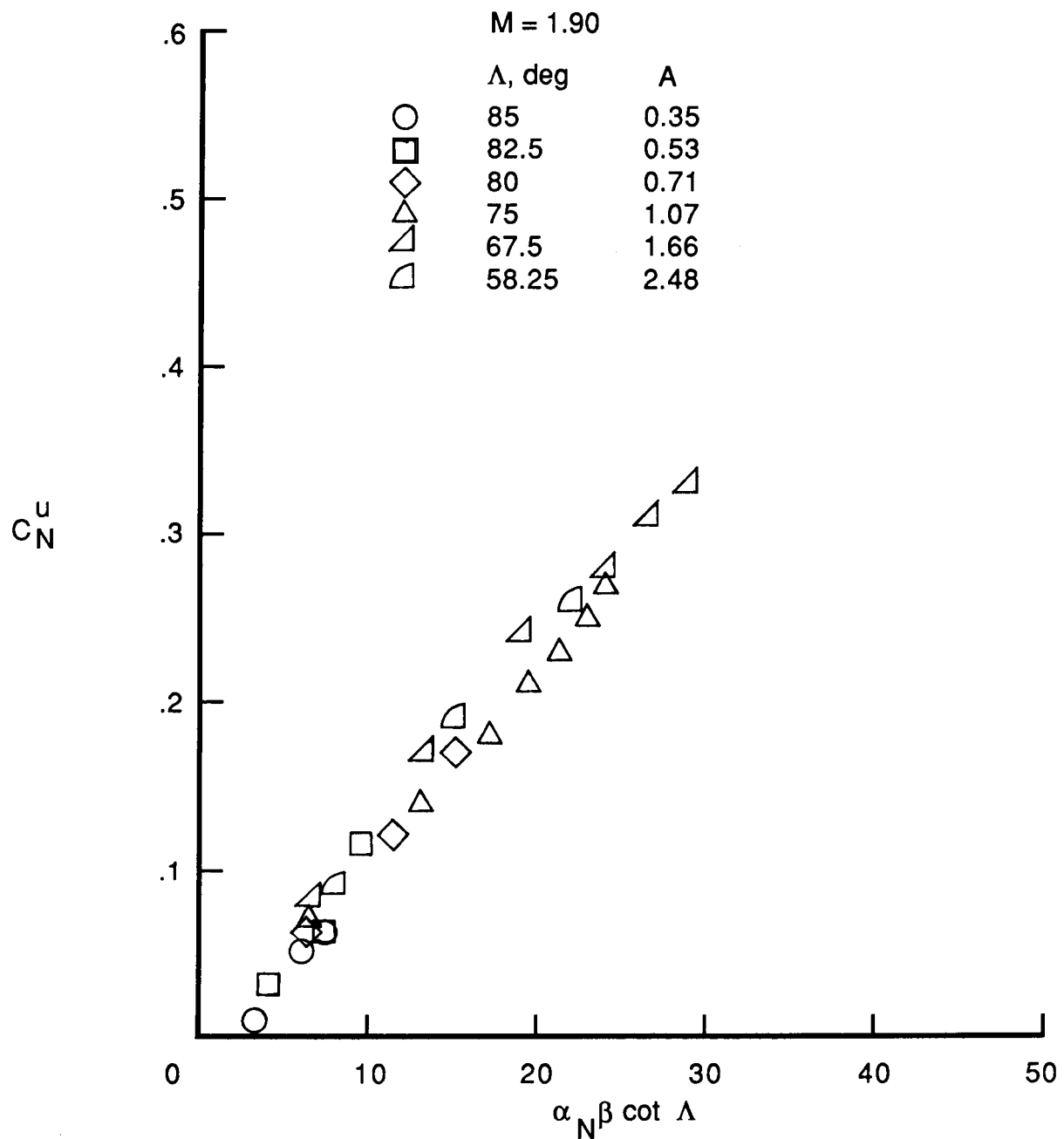
(a) Reference 6.

Figure 34. Wing upper surface normal-force coefficient for thin delta wings.



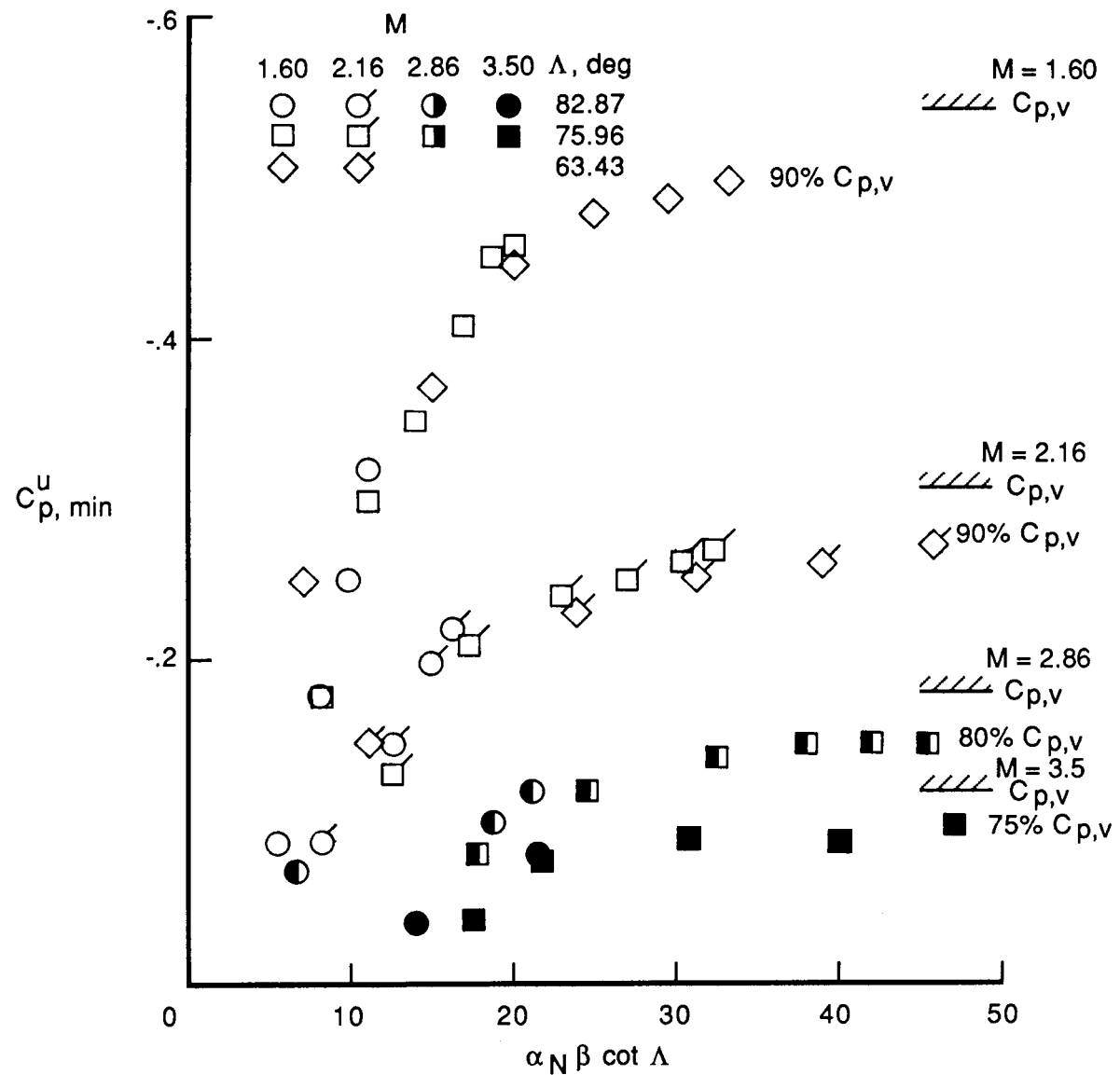
(b) Reference 21.

Figure 34. Continued.



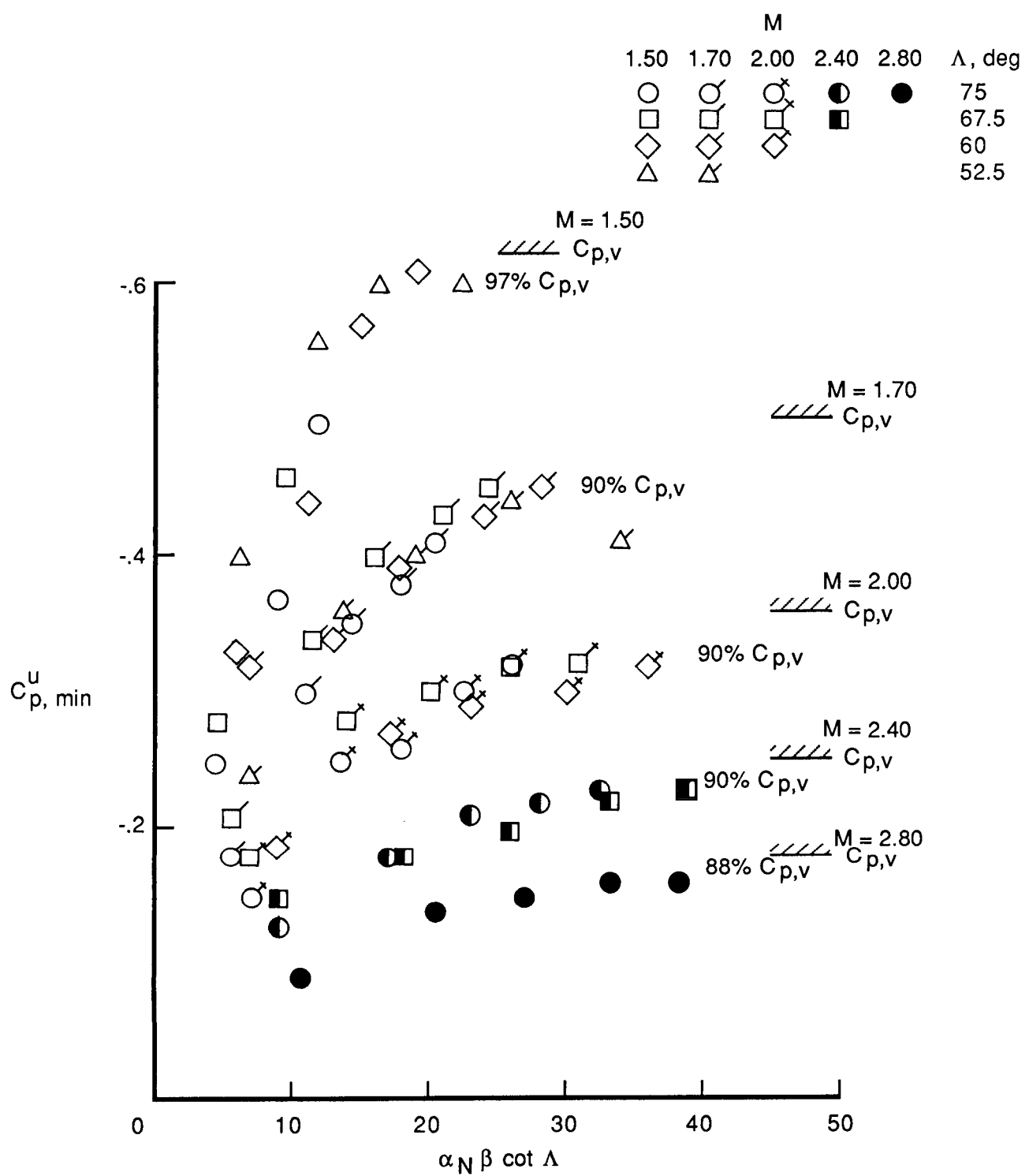
(c) Reference 20.

Figure 34. Concluded.



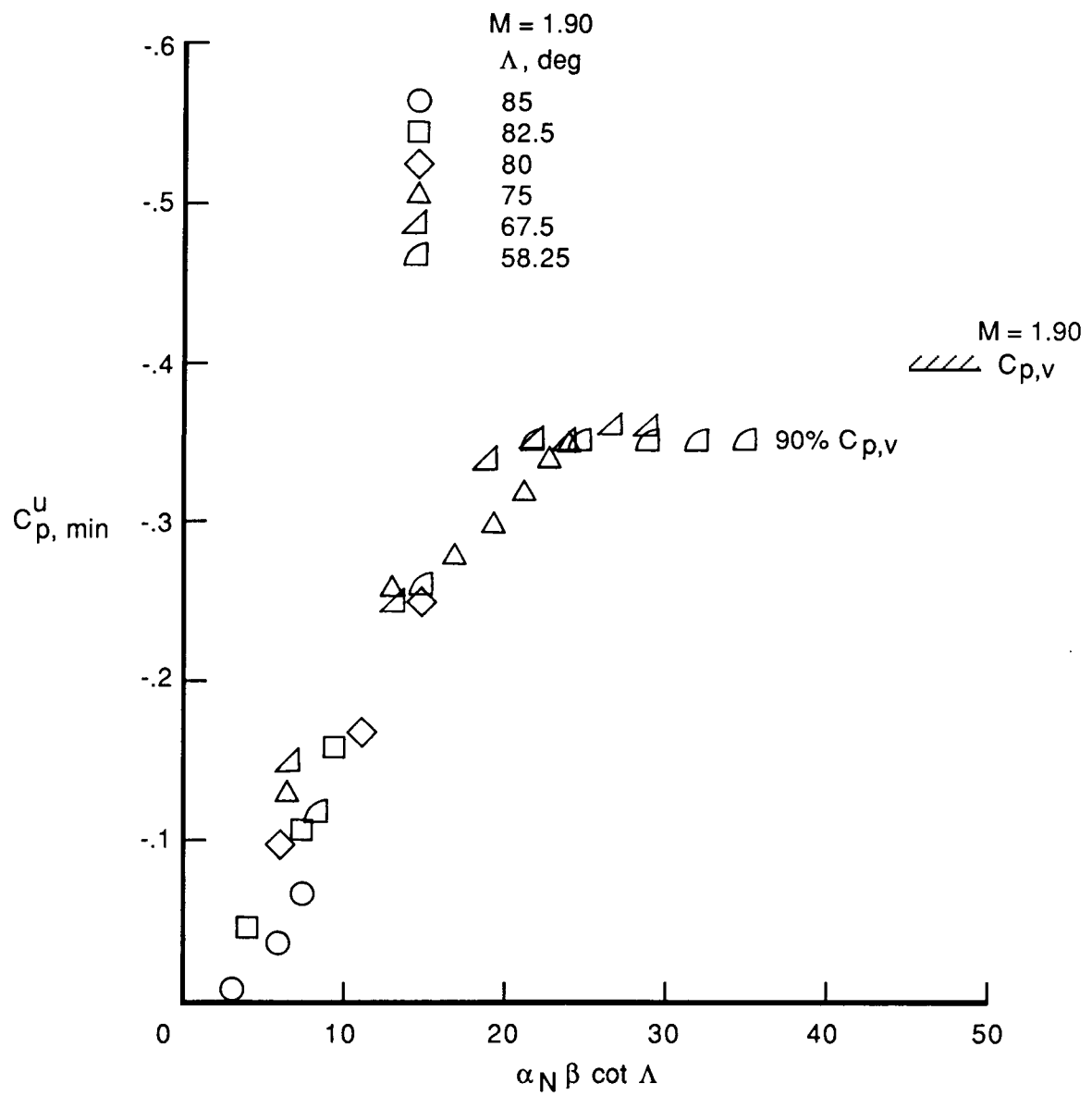
(a) Reference 6.

Figure 35. Minimum upper surface pressure coefficient for thin delta wings.



(b) Reference 21.

Figure 35. Continued.



(c) Reference 20.

Figure 35. Concluded.

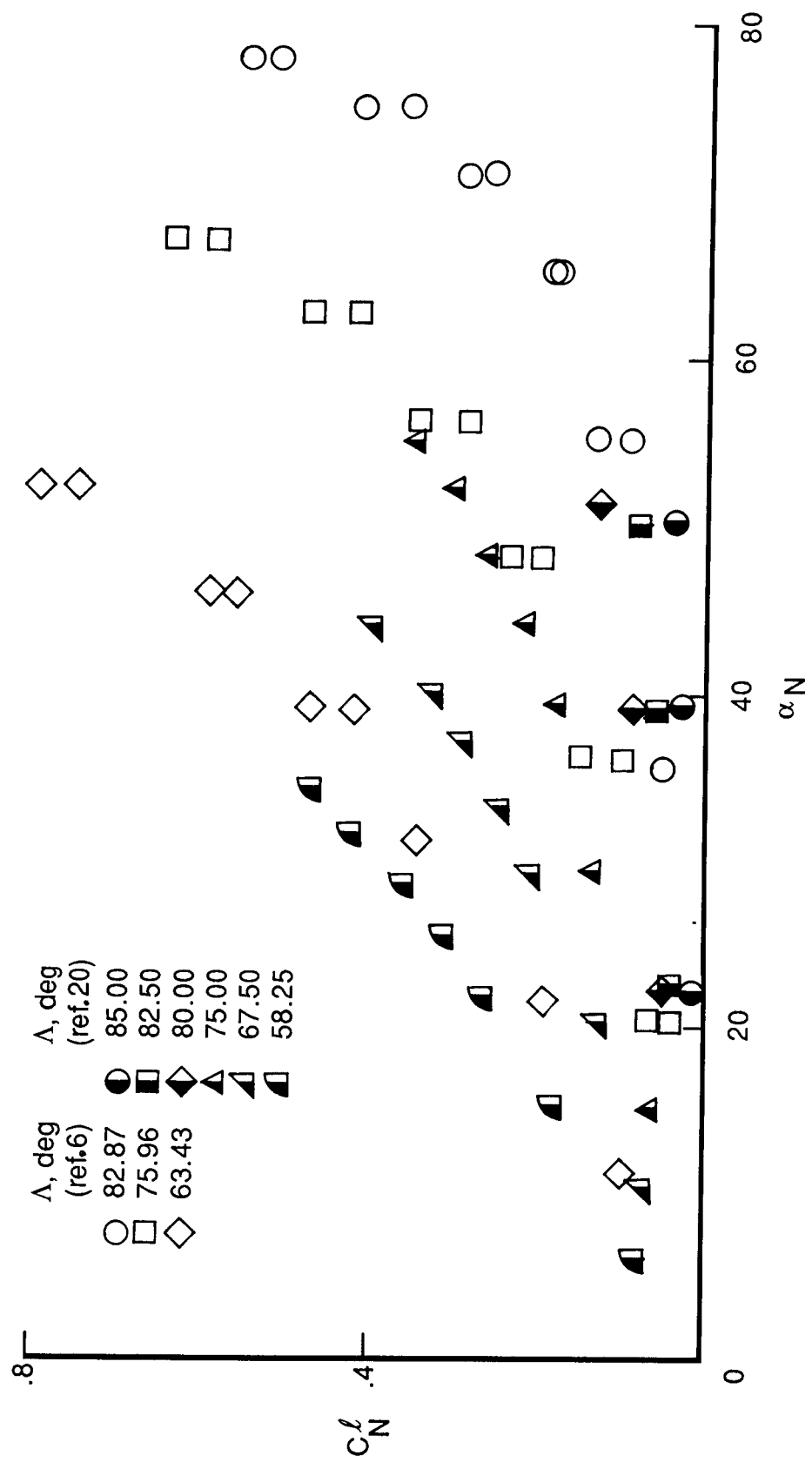
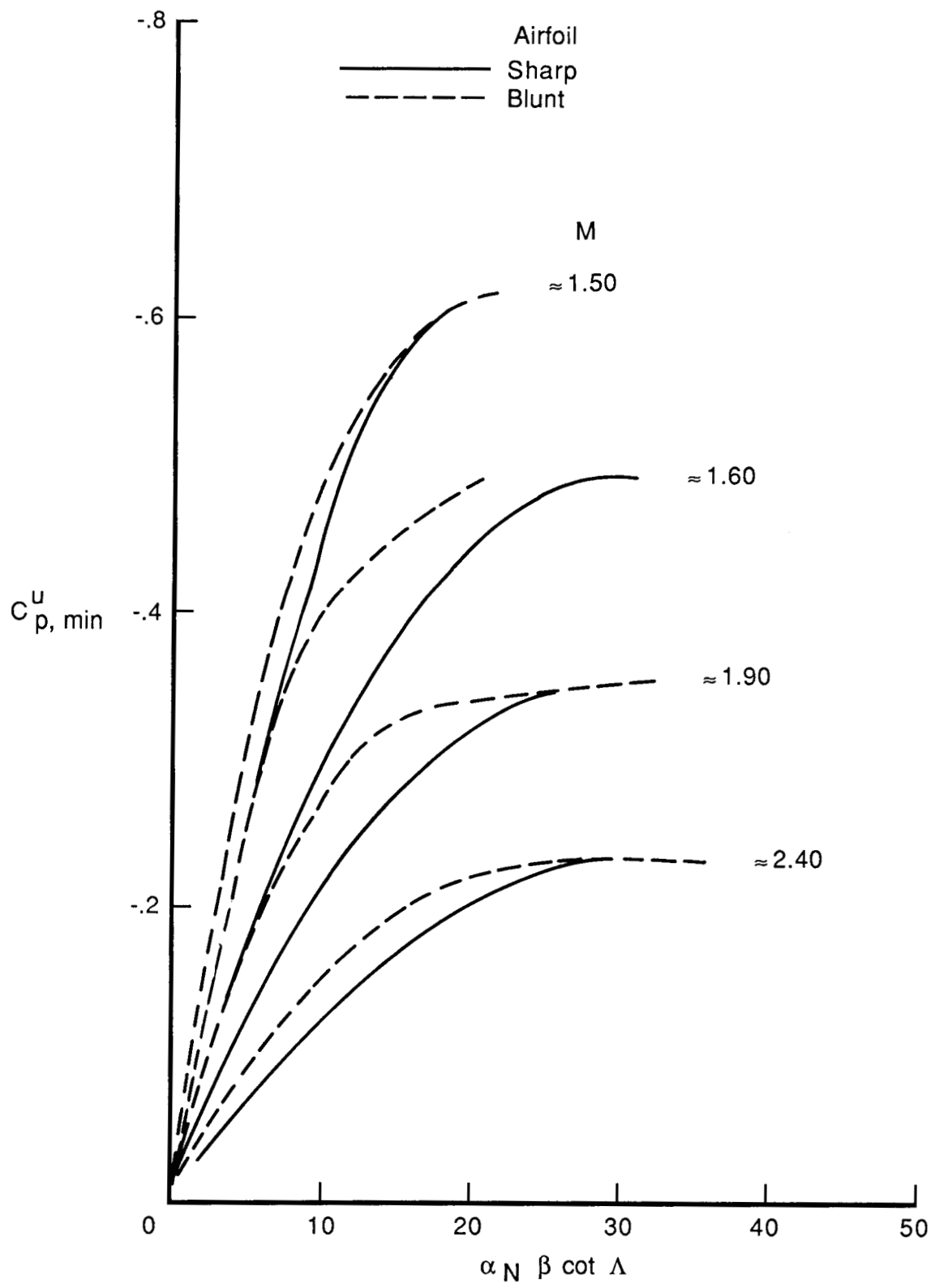
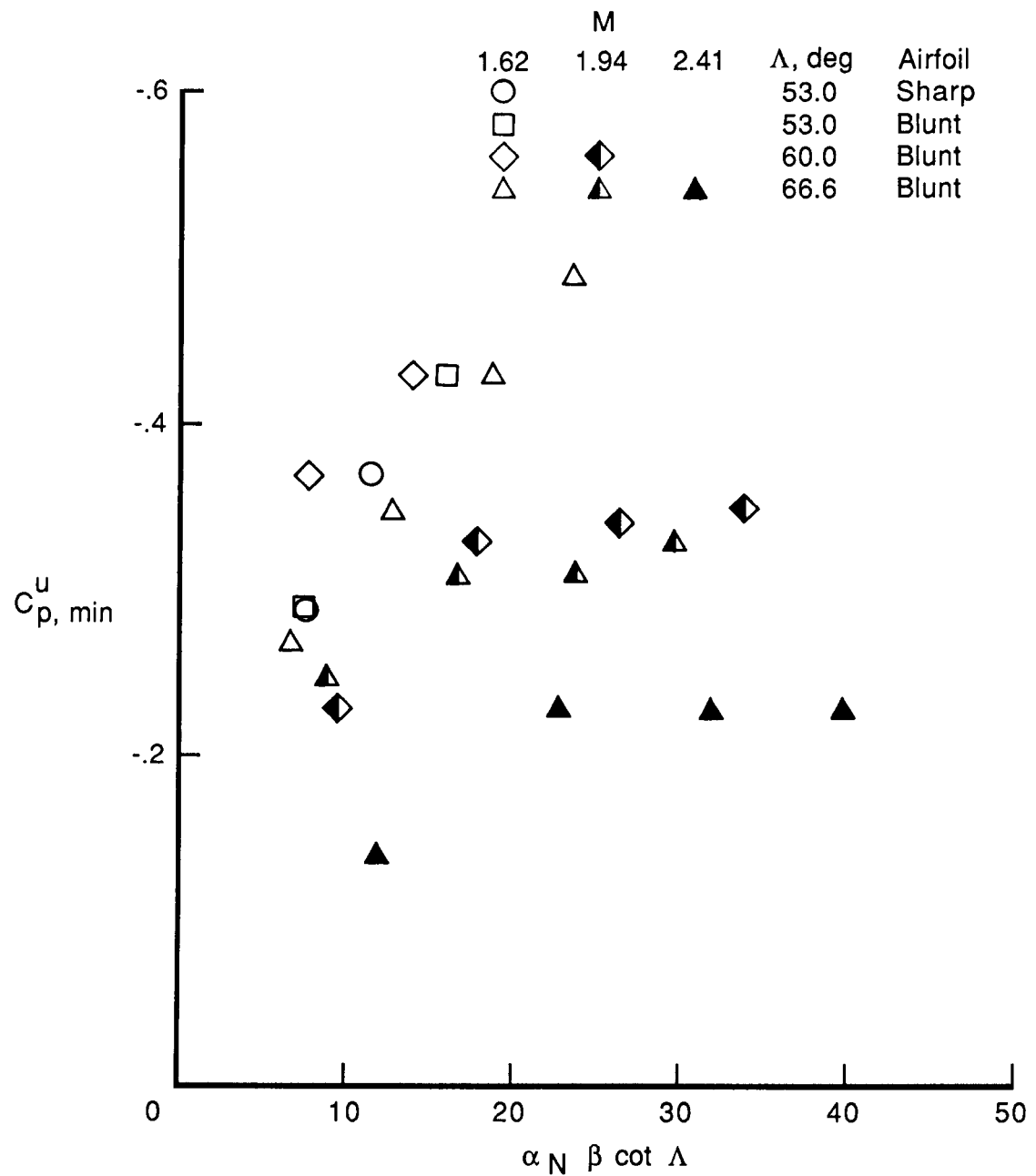


Figure 36. Lower surface normal-force coefficient for delta wings.



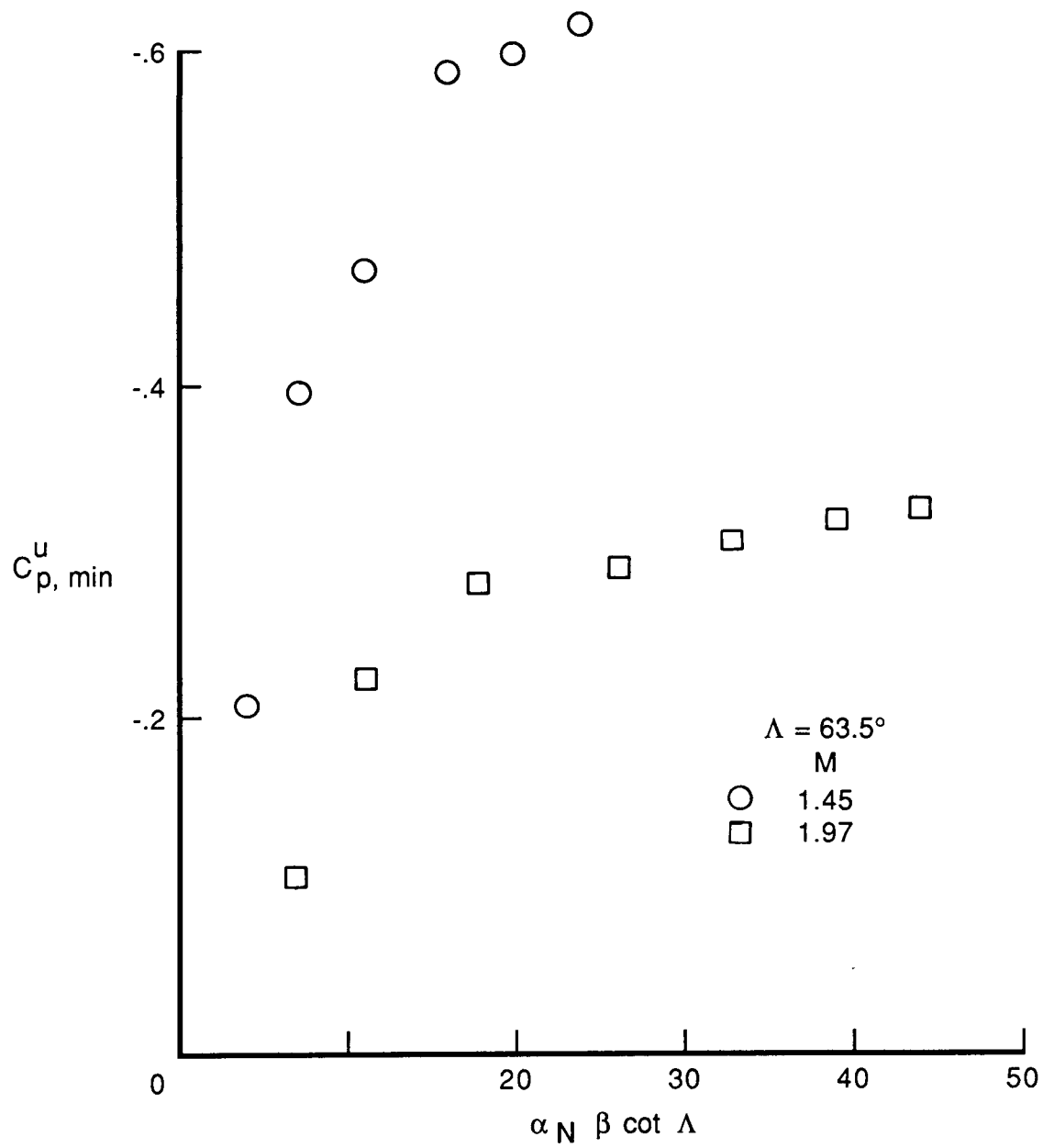
(a) Summary plot.

Figure 37. Effect of wing leading-edge bluntness on C_p^u, min for delta wings.



(b) Reference 18.

Figure 37. Continued.



(c) Reference 16.

Figure 37. Concluded.

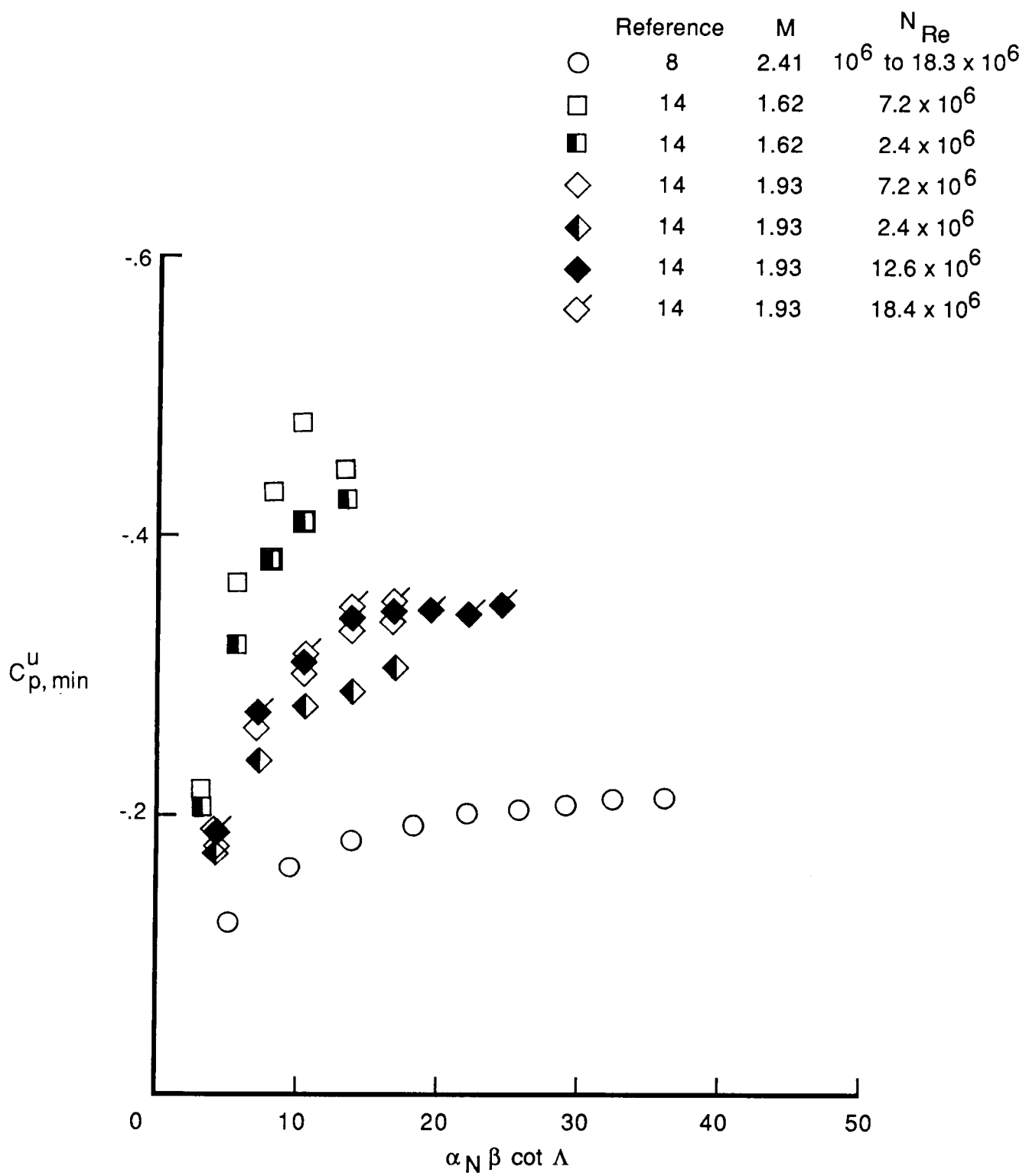


Figure 38. Effect of N_{Re} on $C_{p,\min}^u$ for delta wings with $\Lambda = 68.6^\circ$.

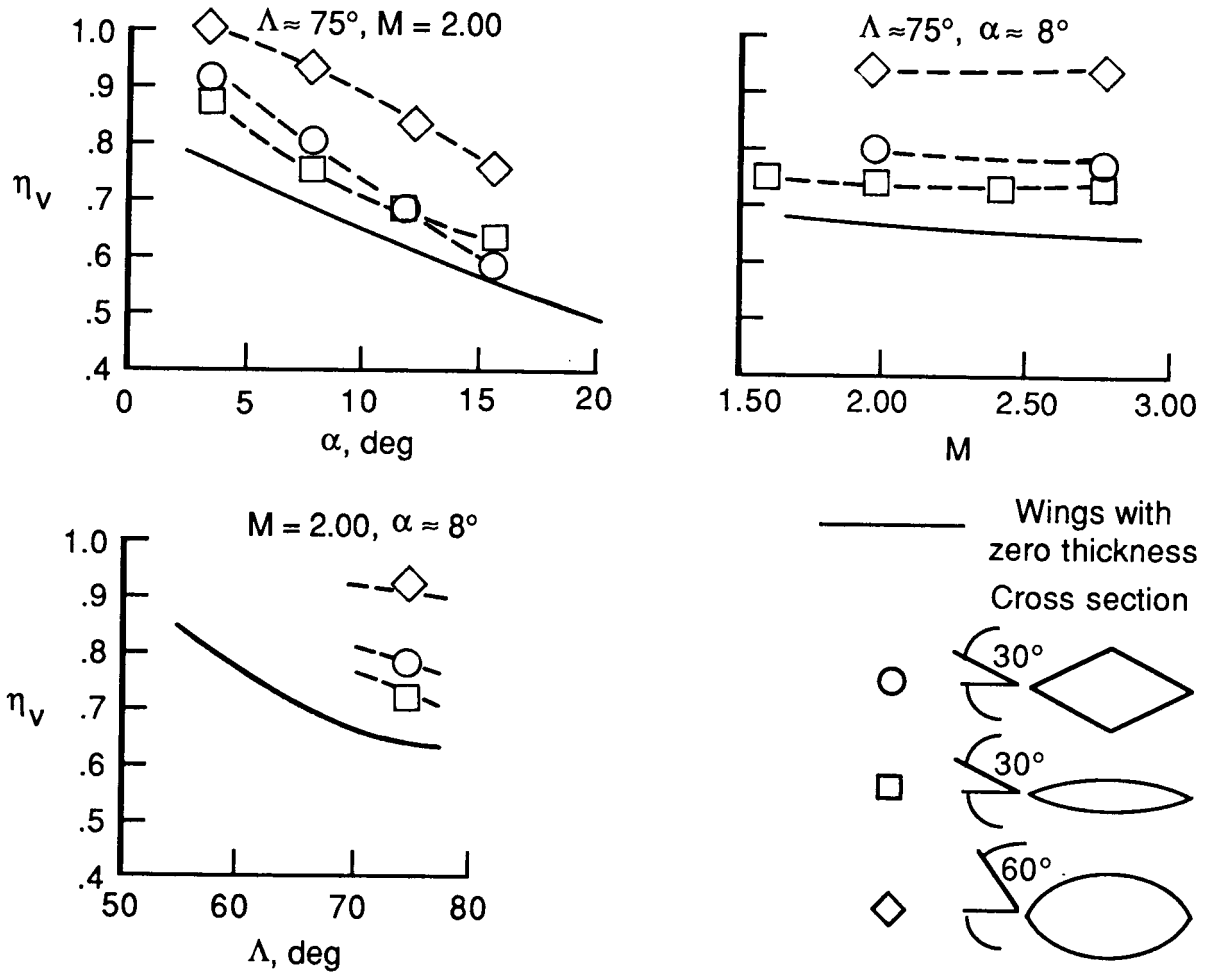


Figure 39. Location of vortex action line for thick delta wings (ref. 23).

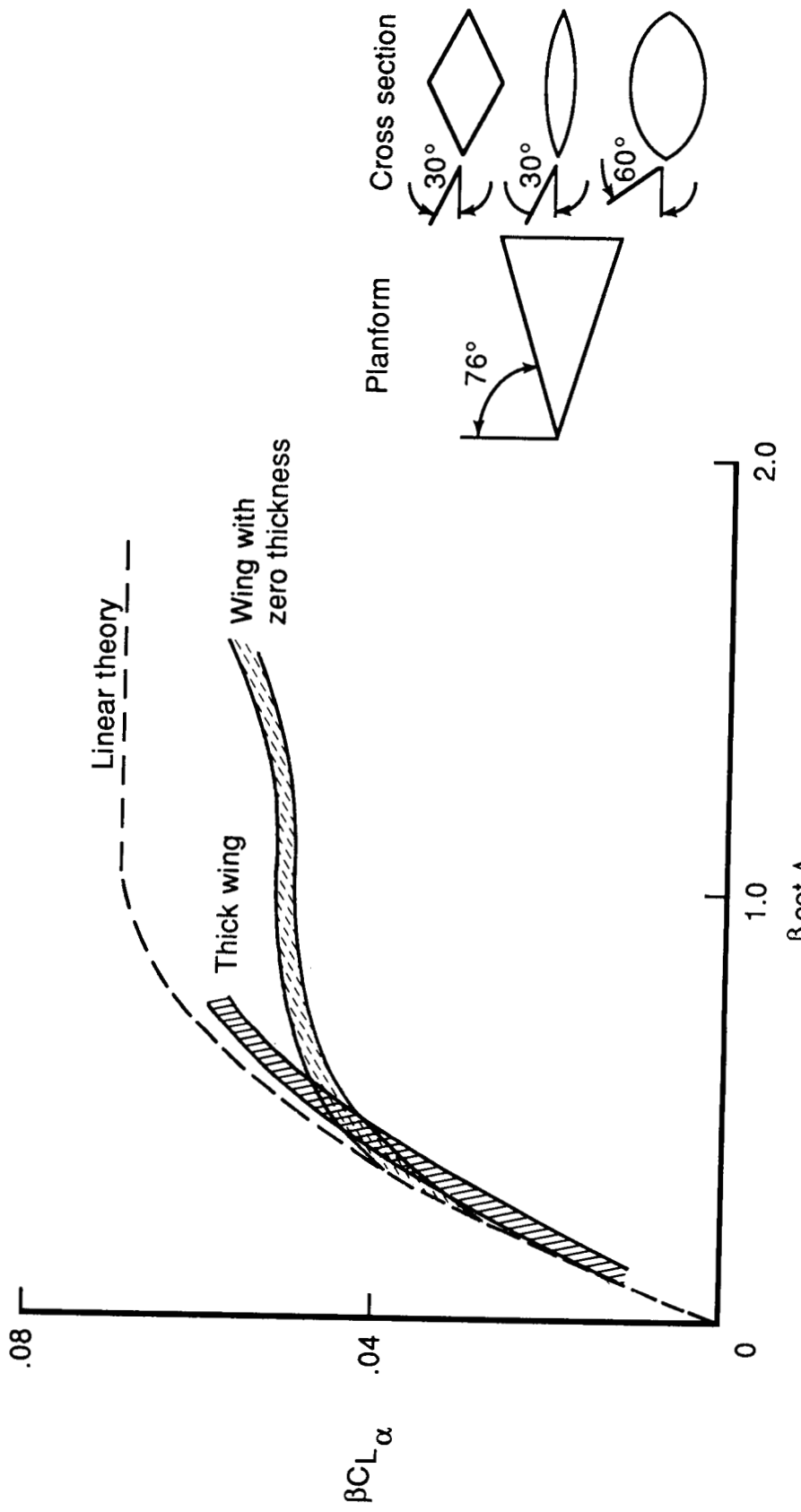


Figure 40. Lifting characteristics of thick and thin delta wings (ref. 23).

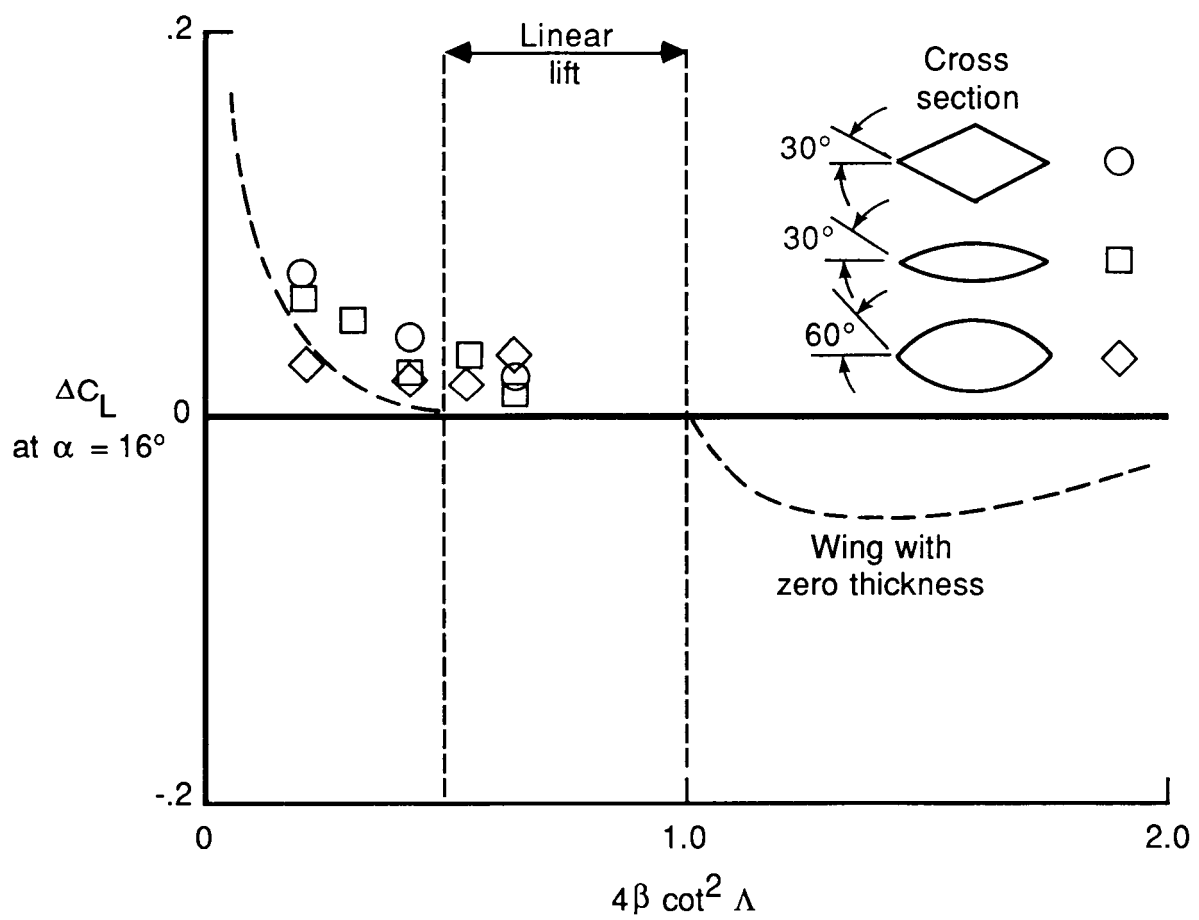


Figure 41. Nonlinear lift effects of thick delta wings (ref. 23).

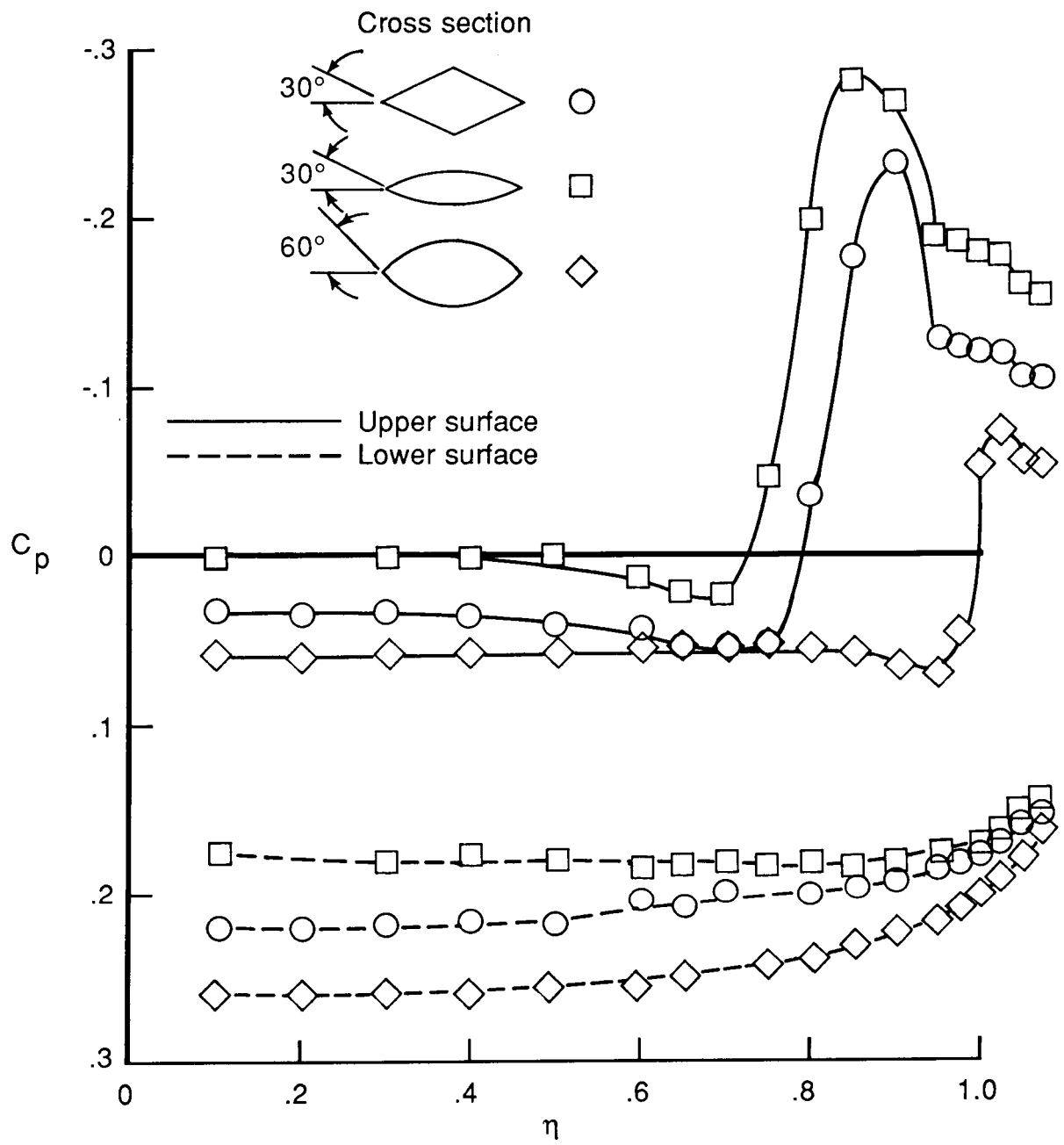


Figure 42. Effect of thickness on spanwise pressure distributions of thick delta wings at $M = 1.30$ and $\alpha = 8.0^\circ$ (ref. 23).

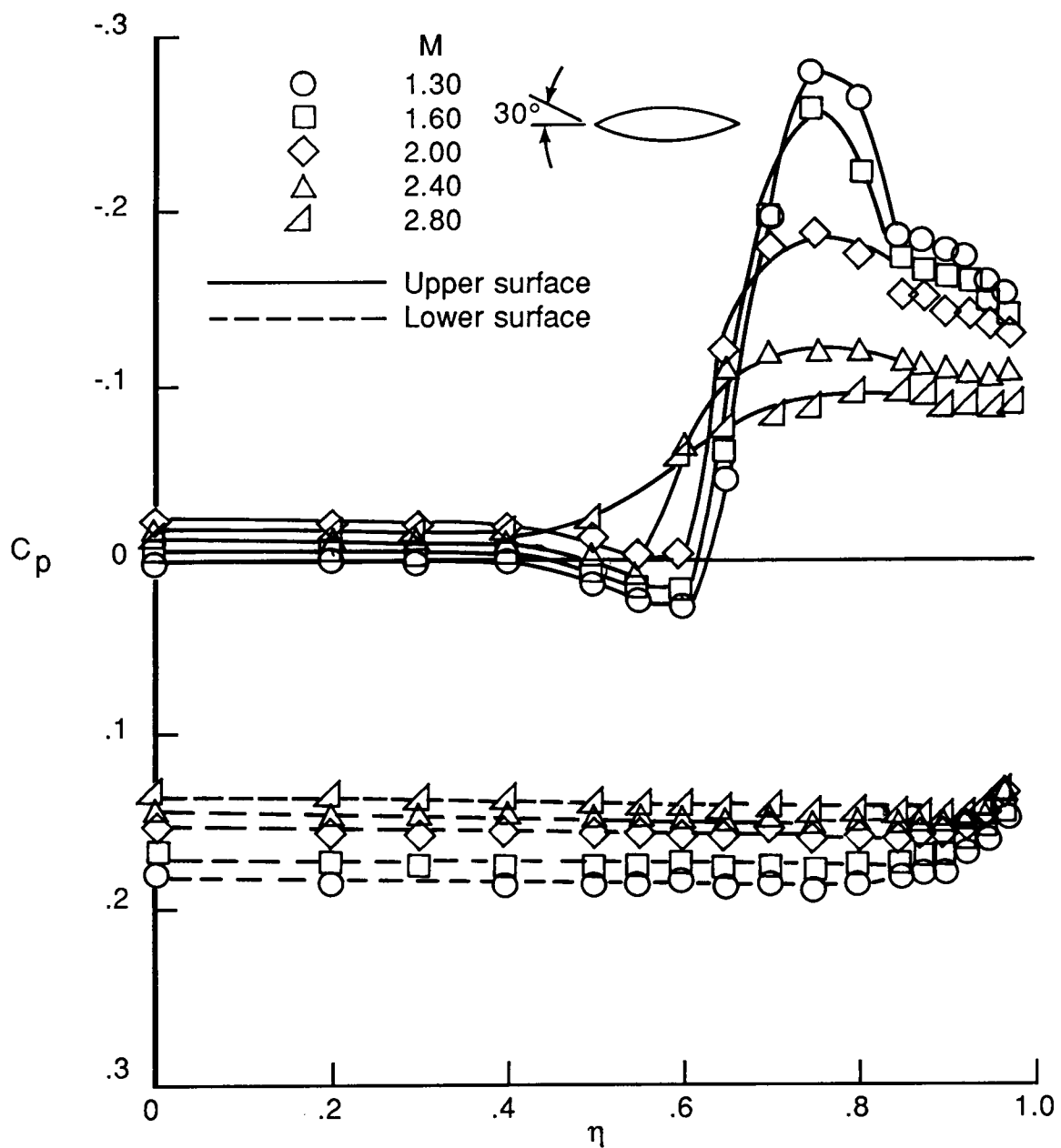


Figure 43. Effect of Mach number on spanwise surface pressure distributions for thick delta wings at $\alpha = 8.0^\circ$ (ref. 23).

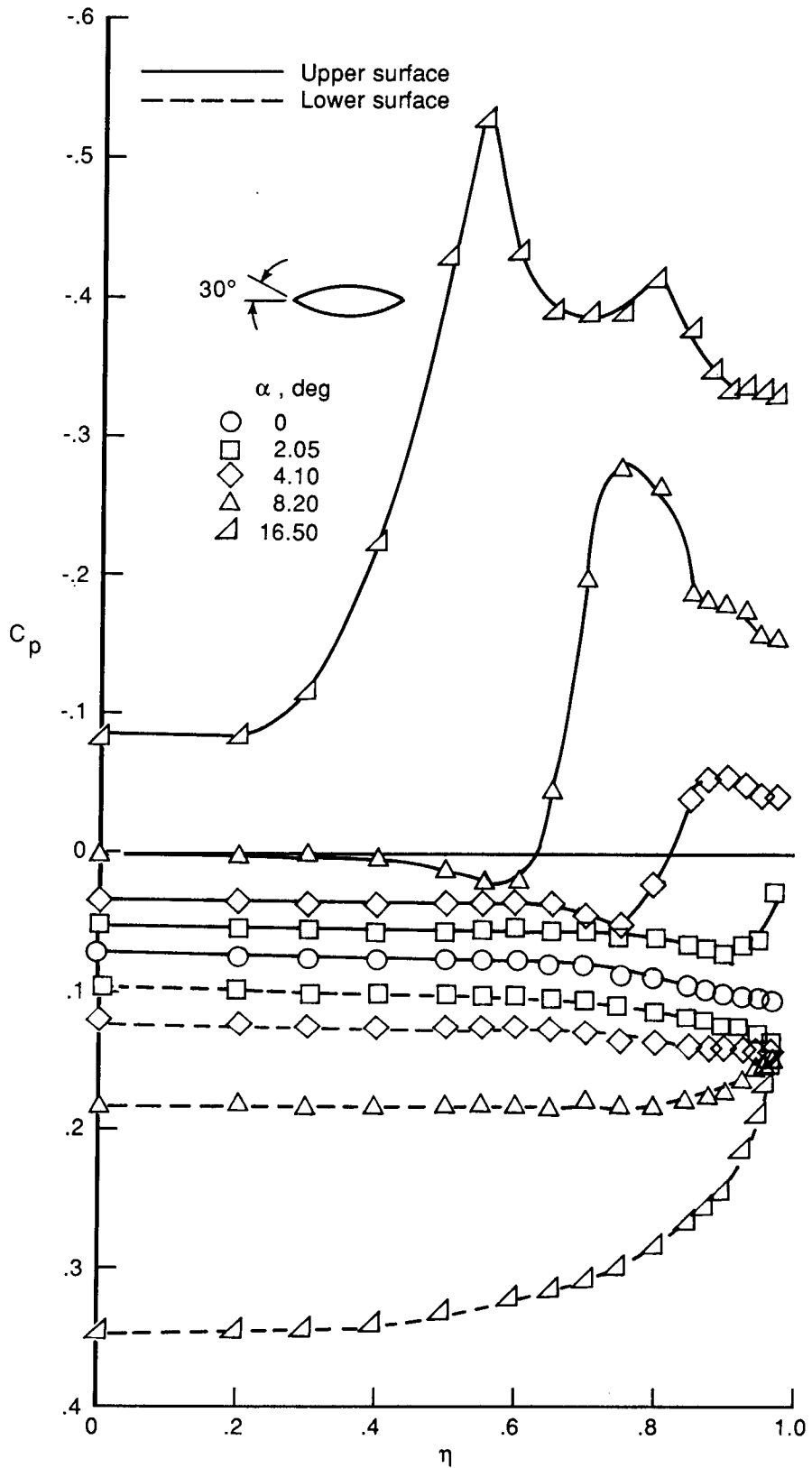


Figure 44. Effect of angle of attack on spanwise surface pressure distributions of thick delta wings at $M = 1.30$ (ref. 23).

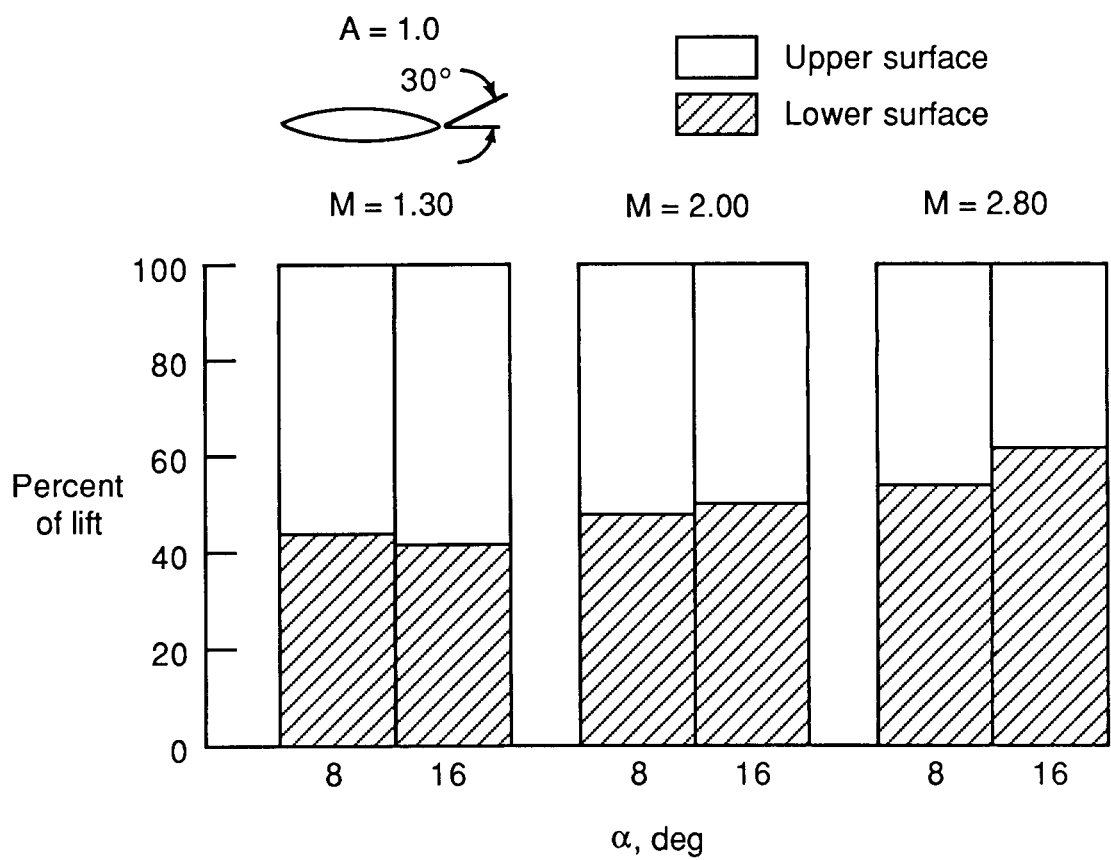


Figure 45. Distribution of lift for thick delta wings (ref. 23).

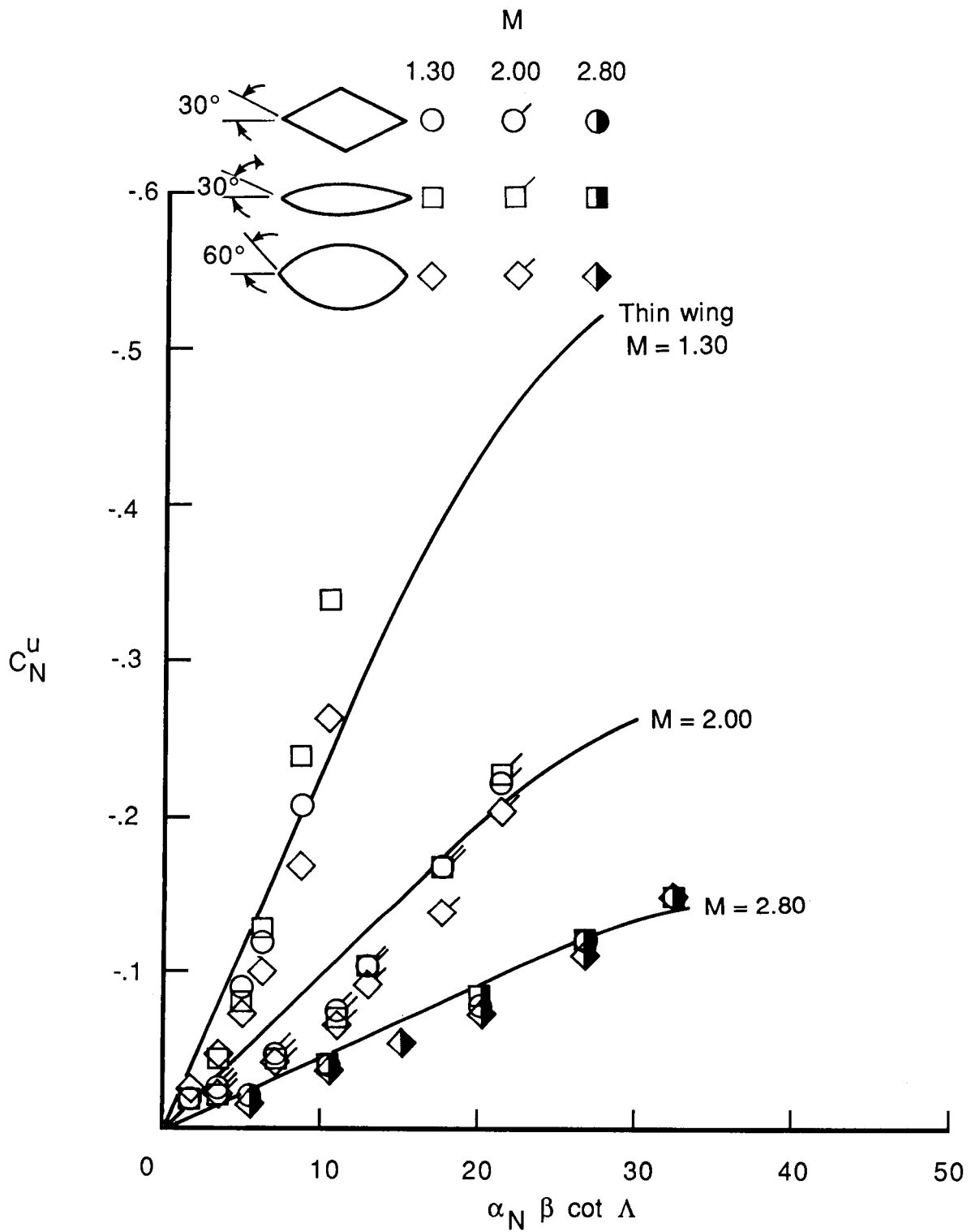


Figure 46. Comparison of upper surface normal-force characteristics on thin and thick delta wings (ref. 23).

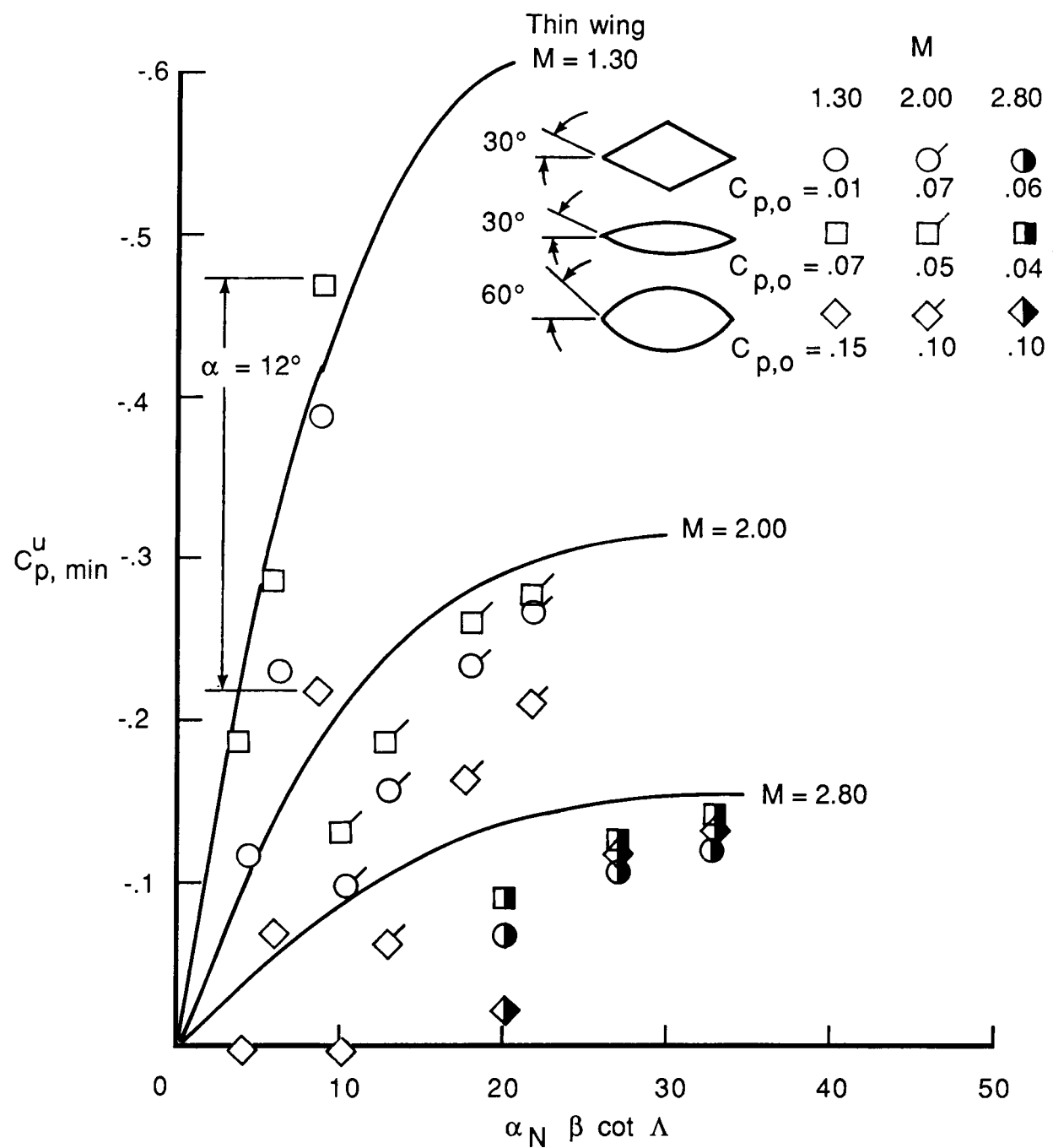


Figure 47. Comparison of upper surface minimum pressure coefficient on thin and thick delta wings (ref. 23).

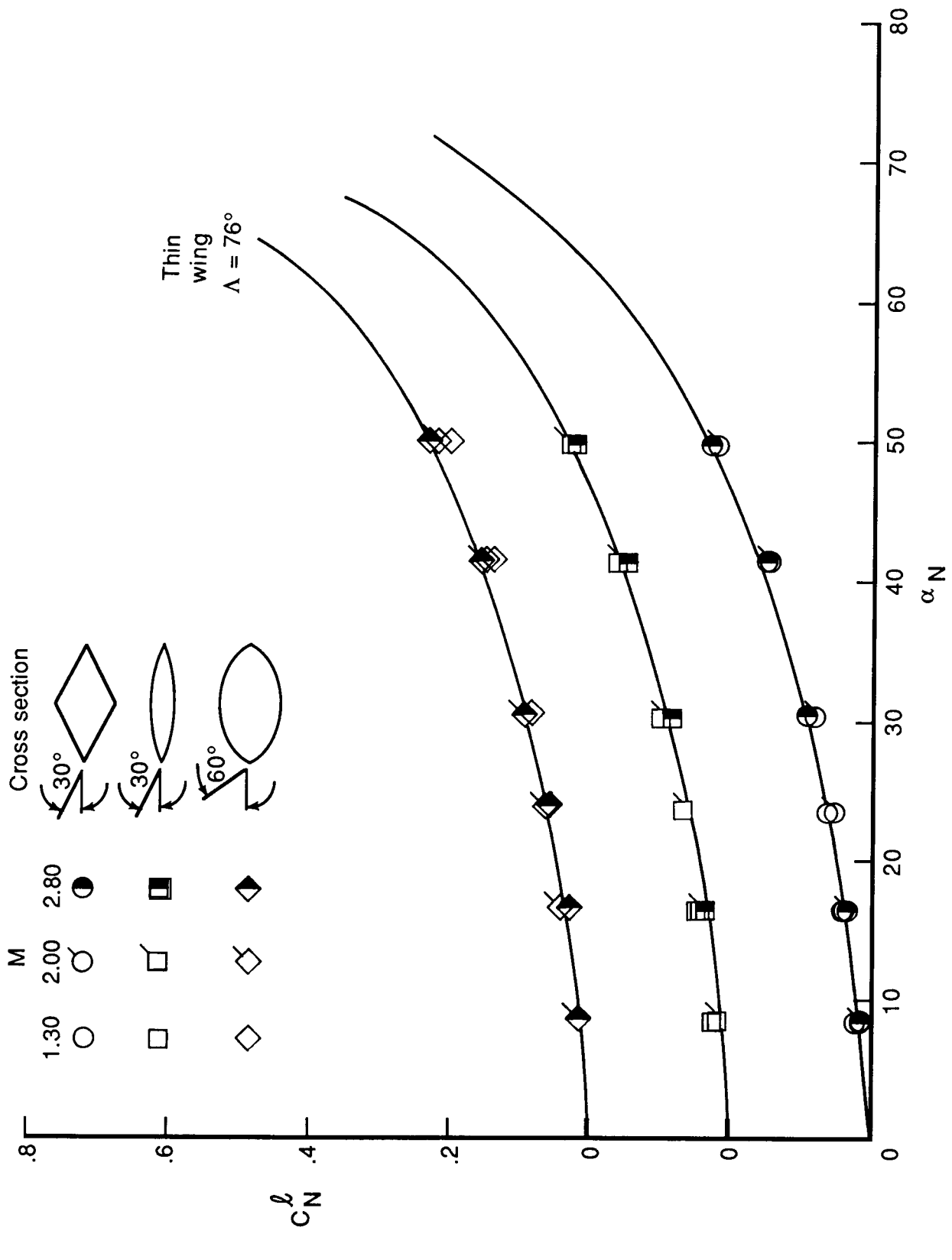


Figure 48. Comparison of lower surface normal-force coefficient for thin and thick delta wings (ref. 23).

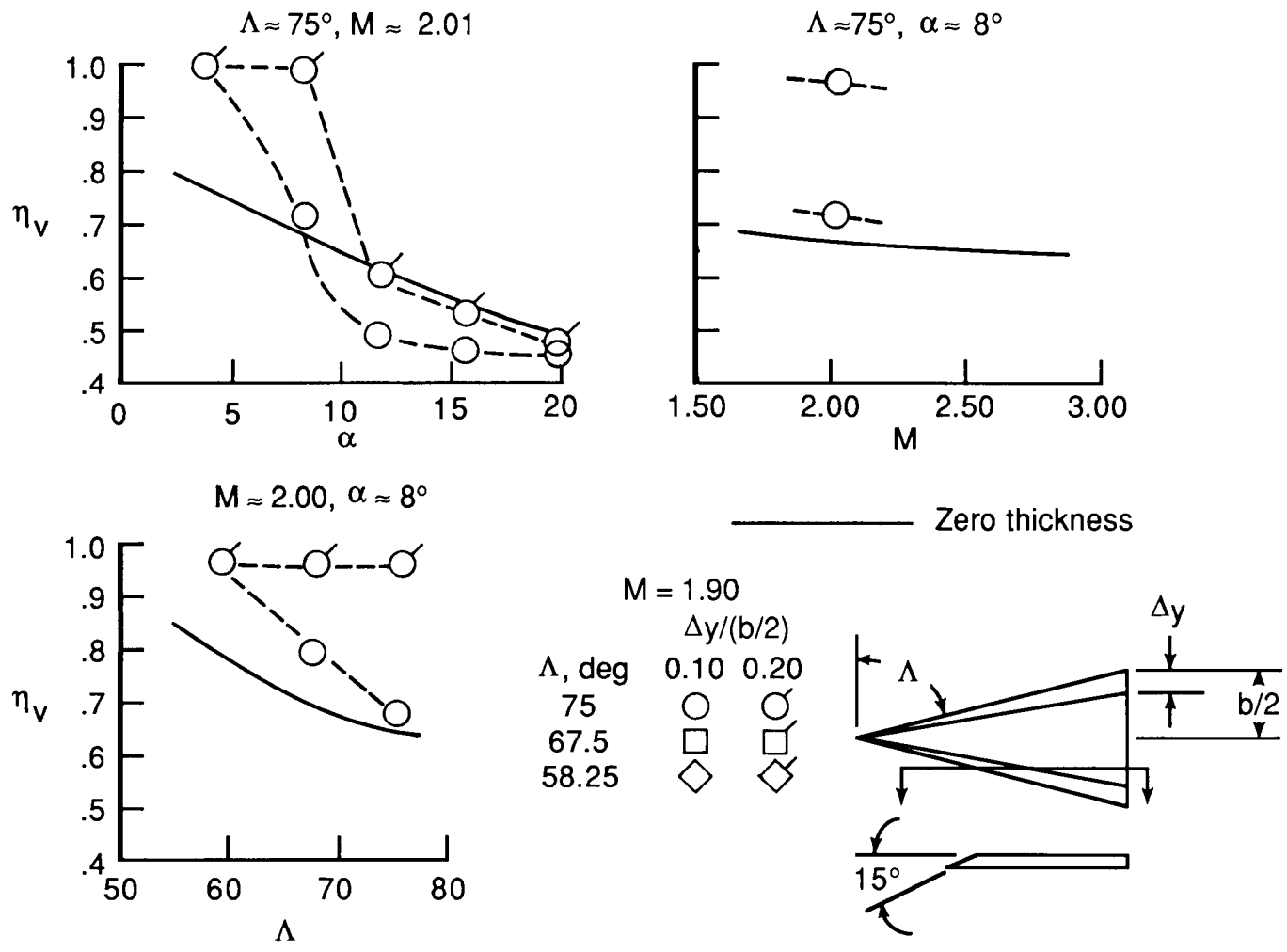


Figure 49. Location of vortex action line for cambered delta wings (ref. 24).

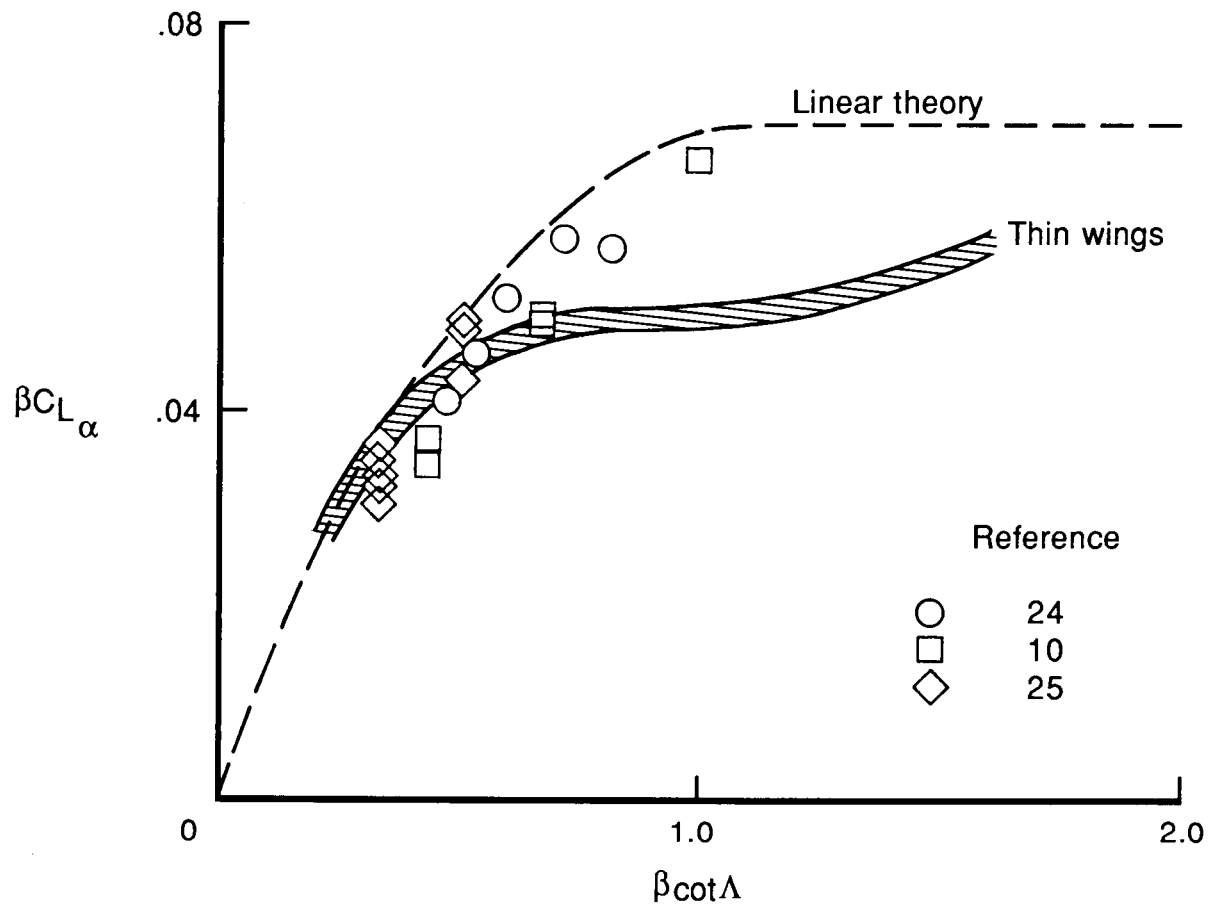


Figure 50. Lifting characteristics of cambered delta wings.

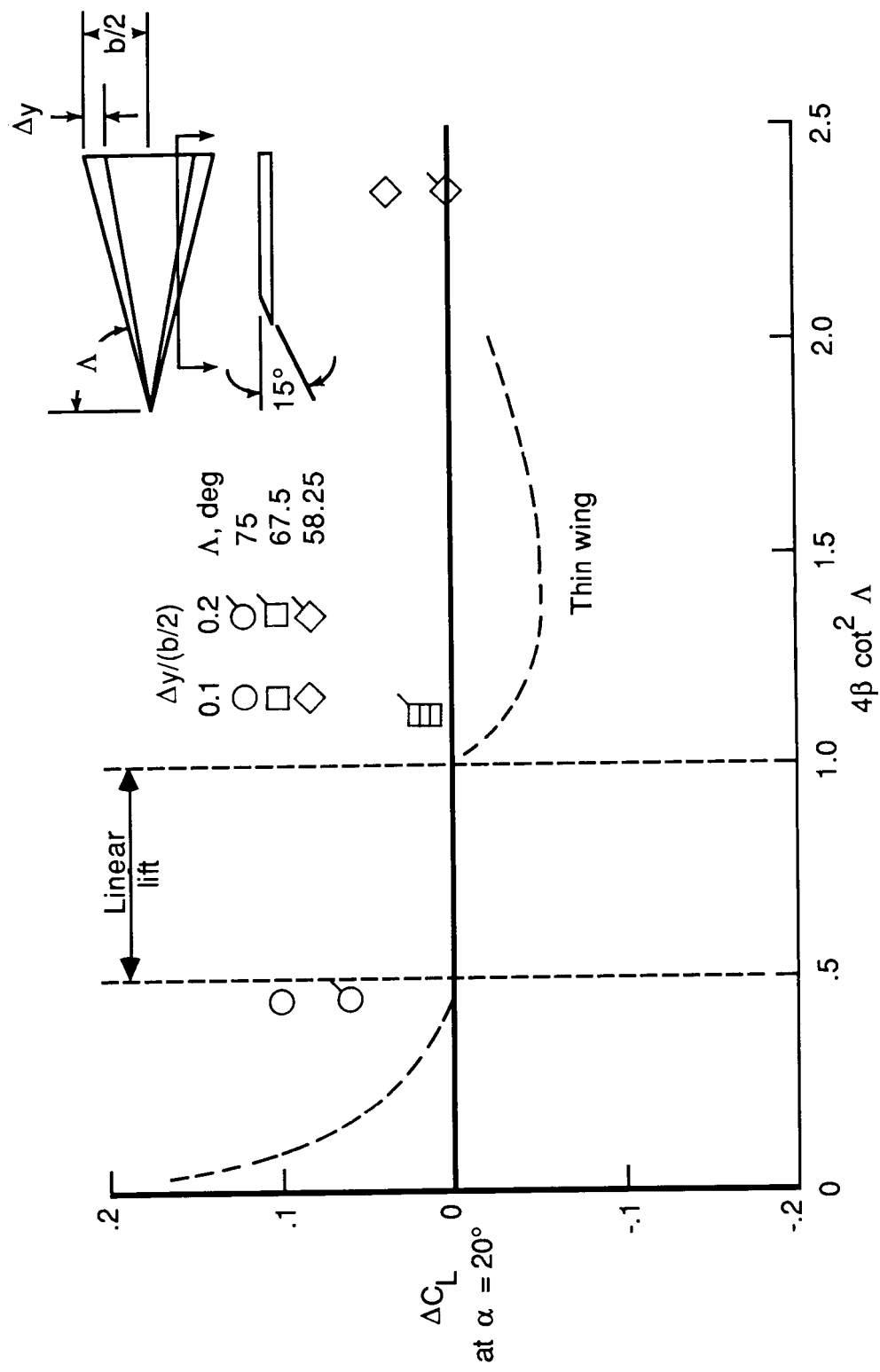


Figure 51. Nonlinear lift effects of cambered delta wings at $M = 1.90$ (ref. 24).

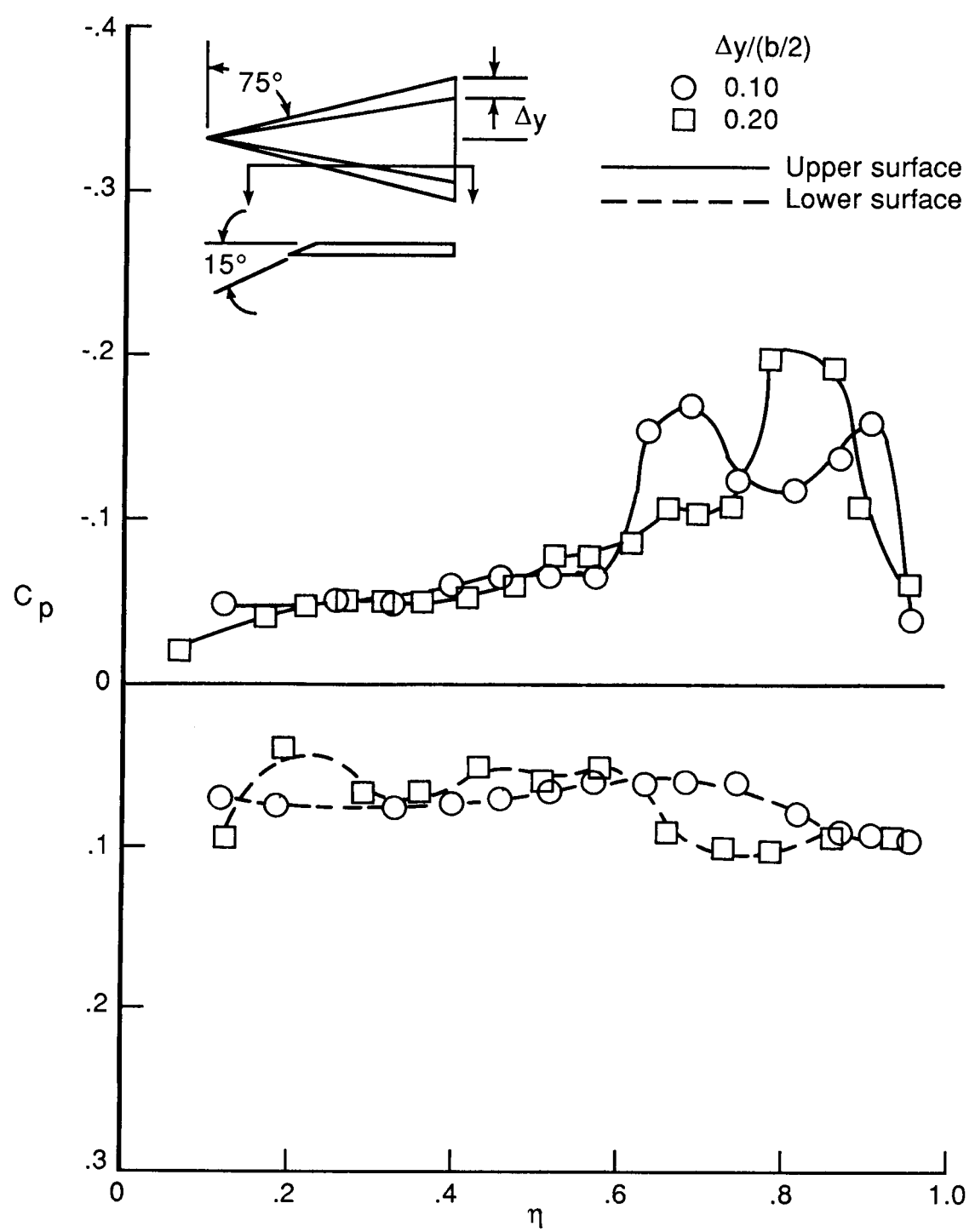


Figure 52. Effect of wing camber on spanwise surface pressure distributions for delta wings at $M = 1.40$ and $\alpha = 8^\circ$ (ref. 24).

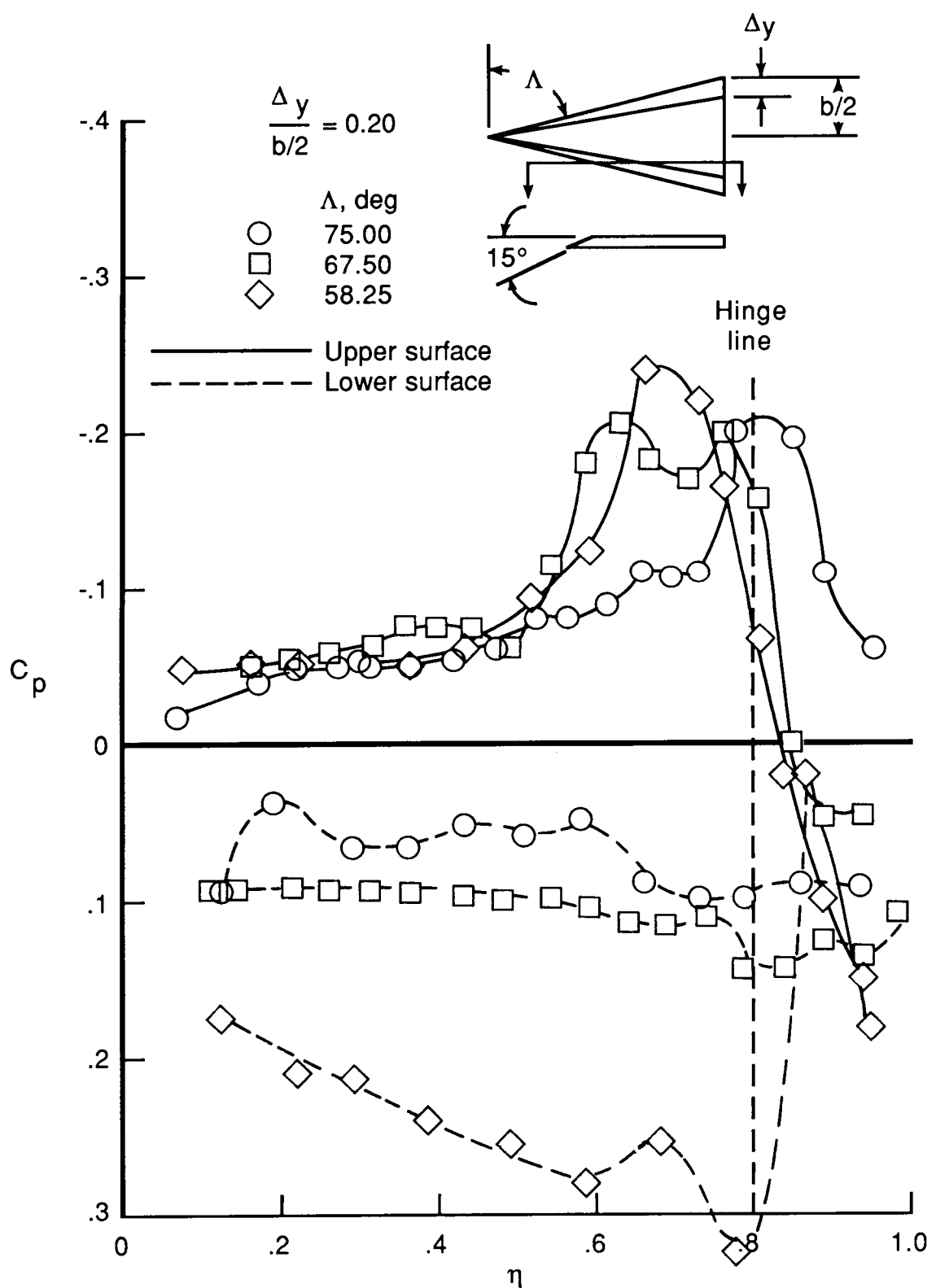


Figure 53. Effect of Λ on spanwise surface pressure distributions for cambered delta wings at $M = 1.90$ and $\alpha = 8^\circ$ (ref. 24).

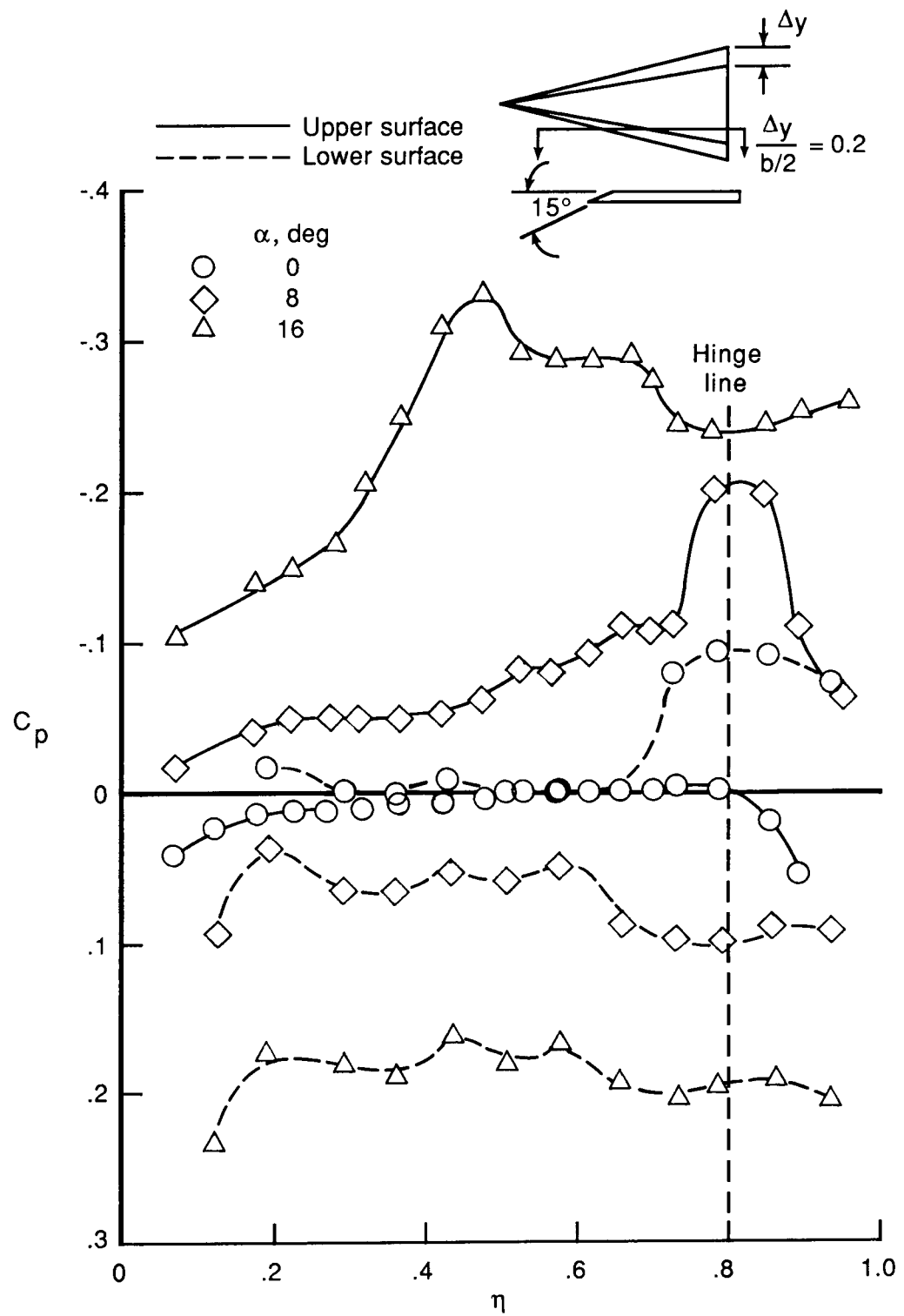


Figure 54. Effect of α on spanwise surface pressure distributions for cambered delta wings at $M = 1.90$ (ref. 24).

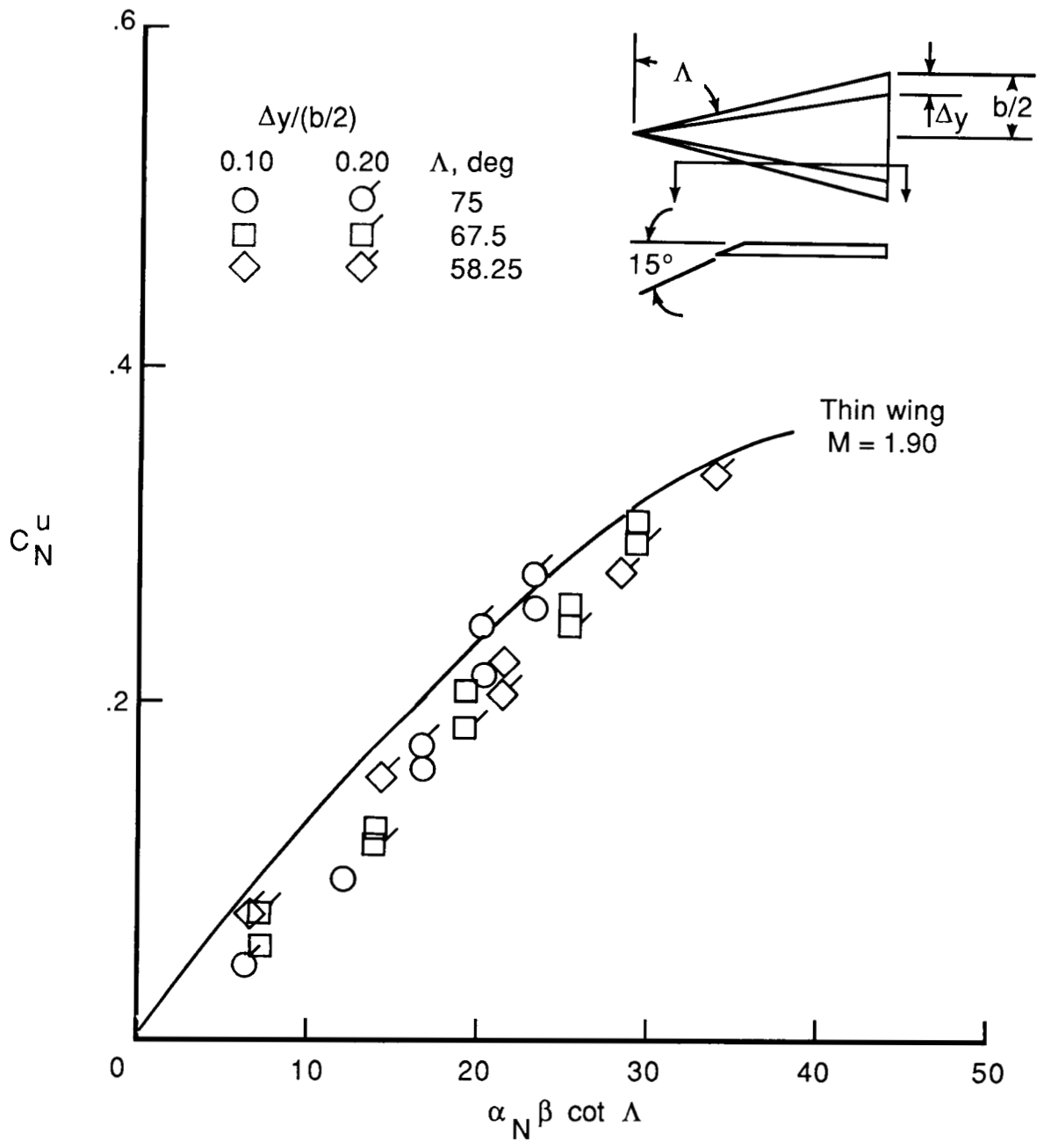


Figure 55. Upper surface normal-force coefficient for cambered delta wings (ref. 24).

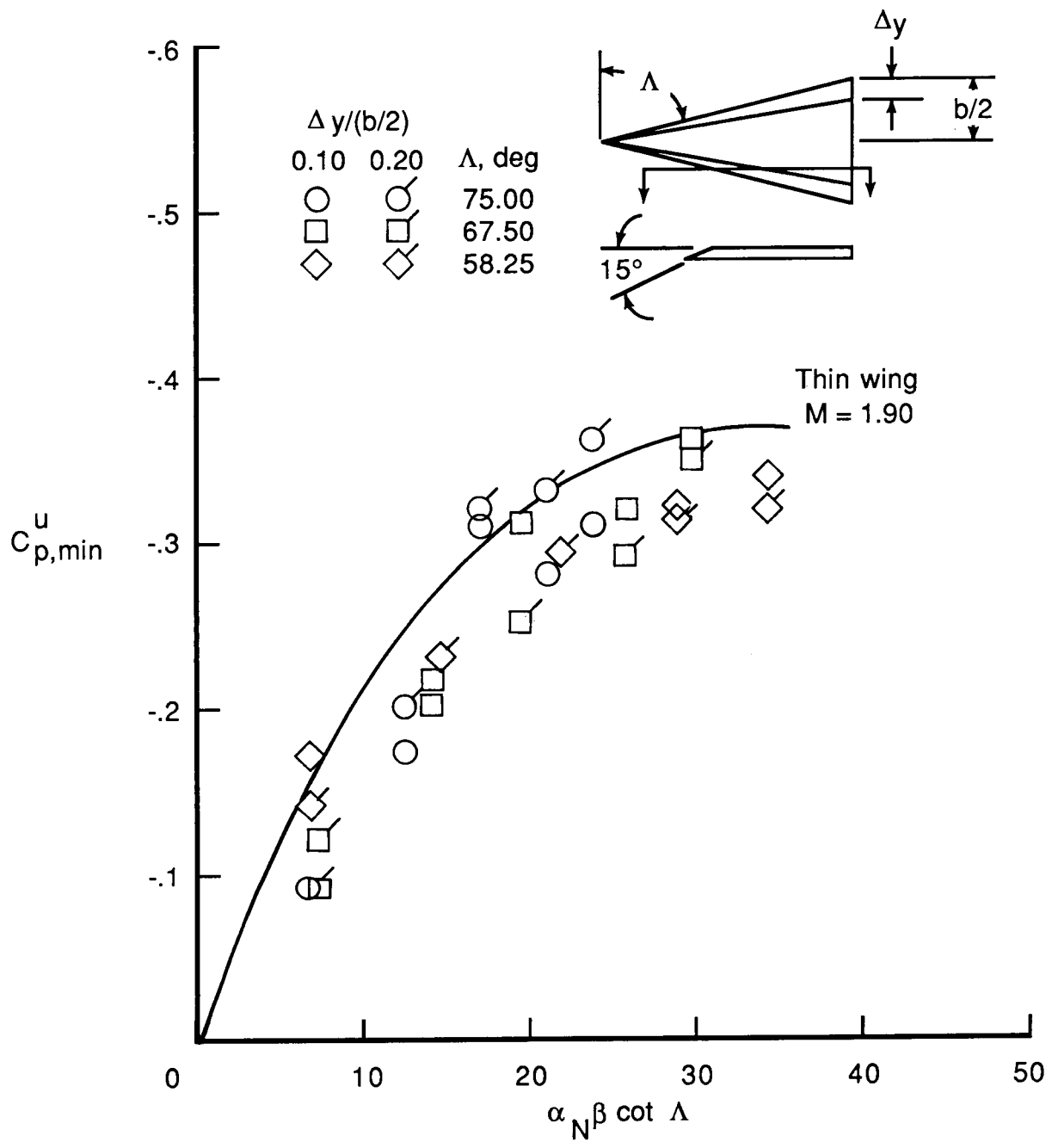


Figure 56. Upper surface minimum pressure coefficient for cambered delta wings (ref. 24).

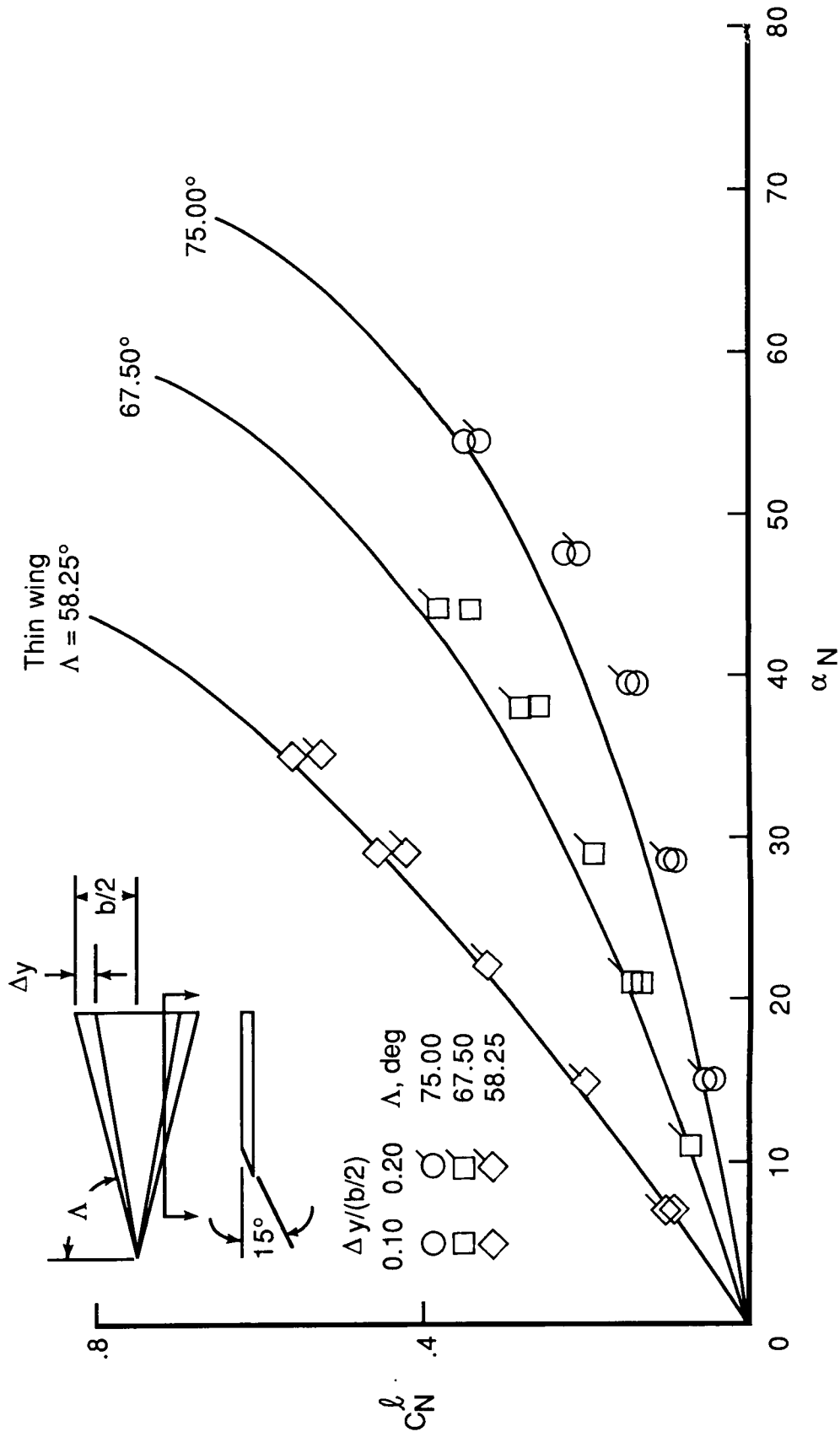


Figure 57. Lower surface normal-force coefficient for cambered delta wings (ref. 24).

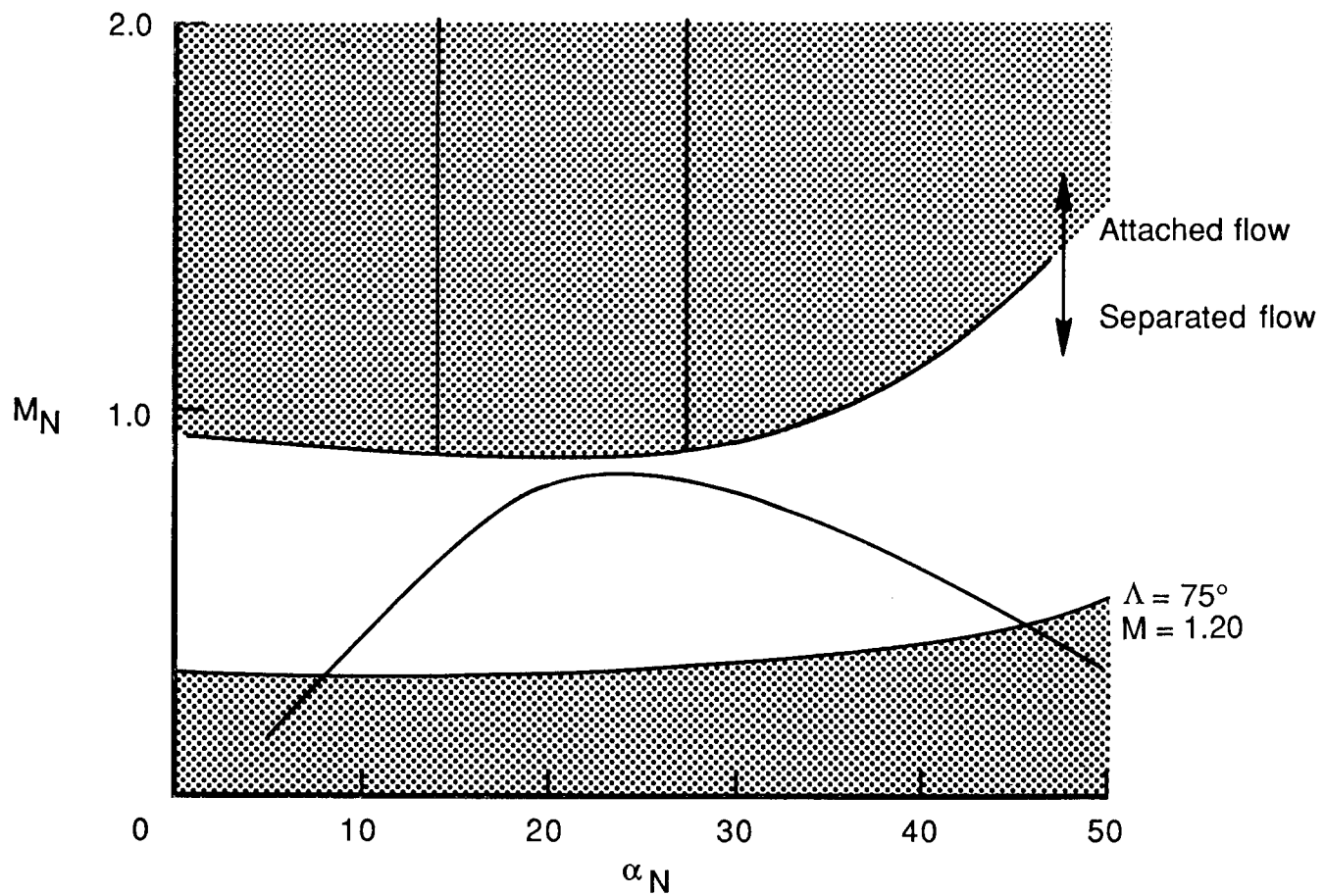


Figure 58. Influence of minimum M , maximum wing sweep, and separated flow restriction on design space.

$C - \alpha$

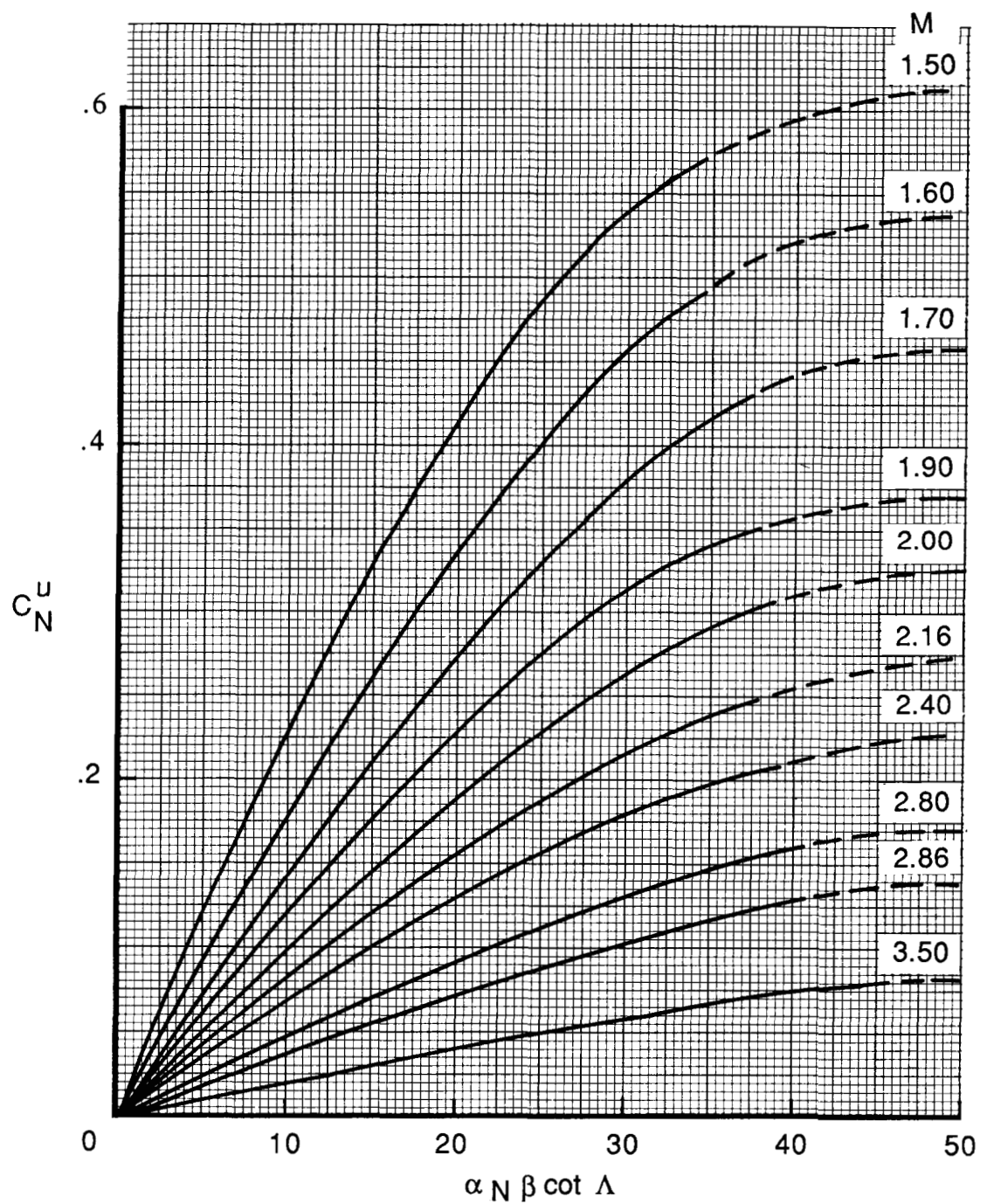


Figure 59. Delta wing upper surface normal-force coefficient design curves.

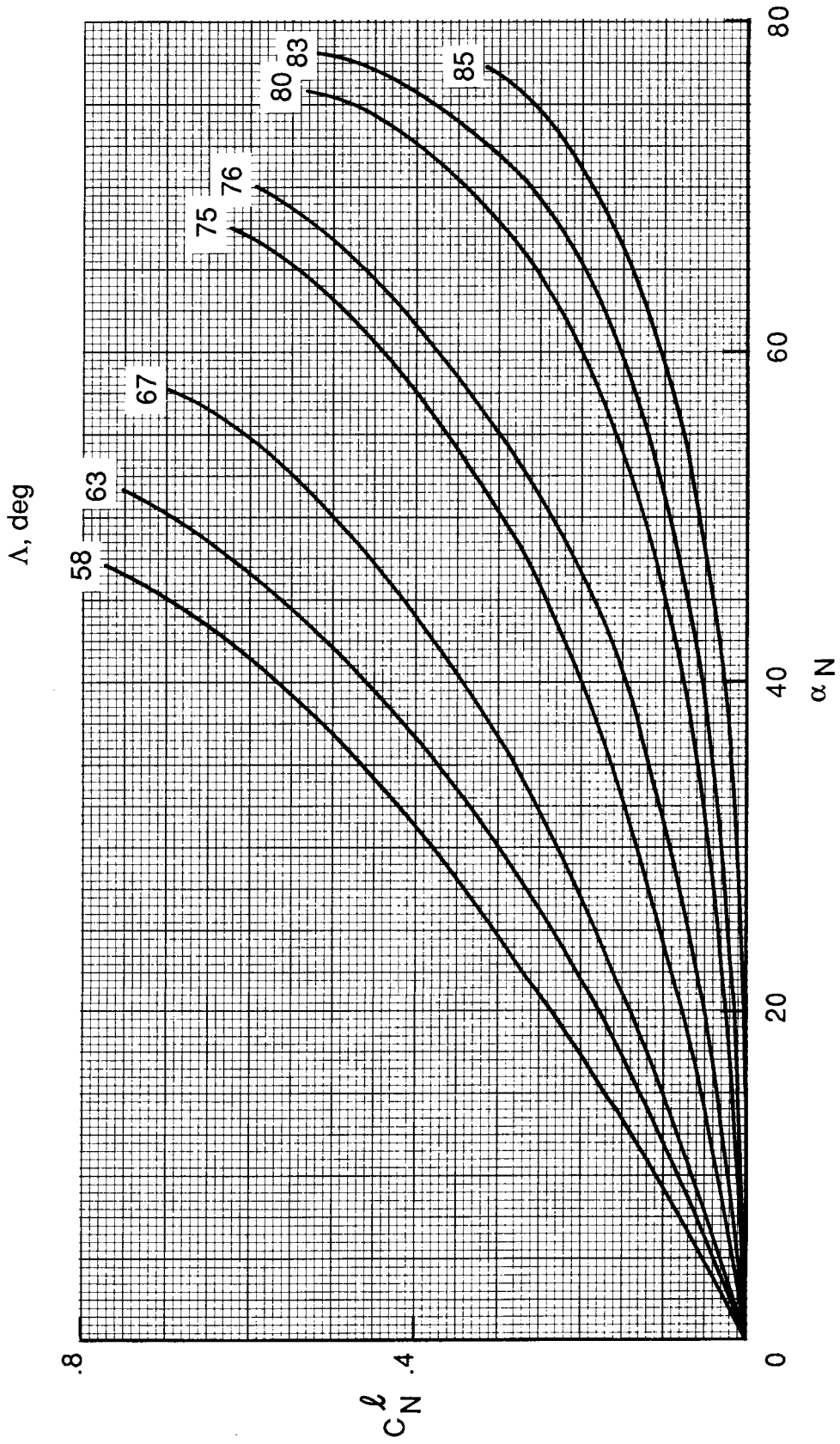


Figure 60. Delta wing lower surface normal-force coefficient design curves.

$$M_N = M \cos \Lambda (1 + \sin^2 \alpha + \tan^2 \Lambda)^{1/2}$$

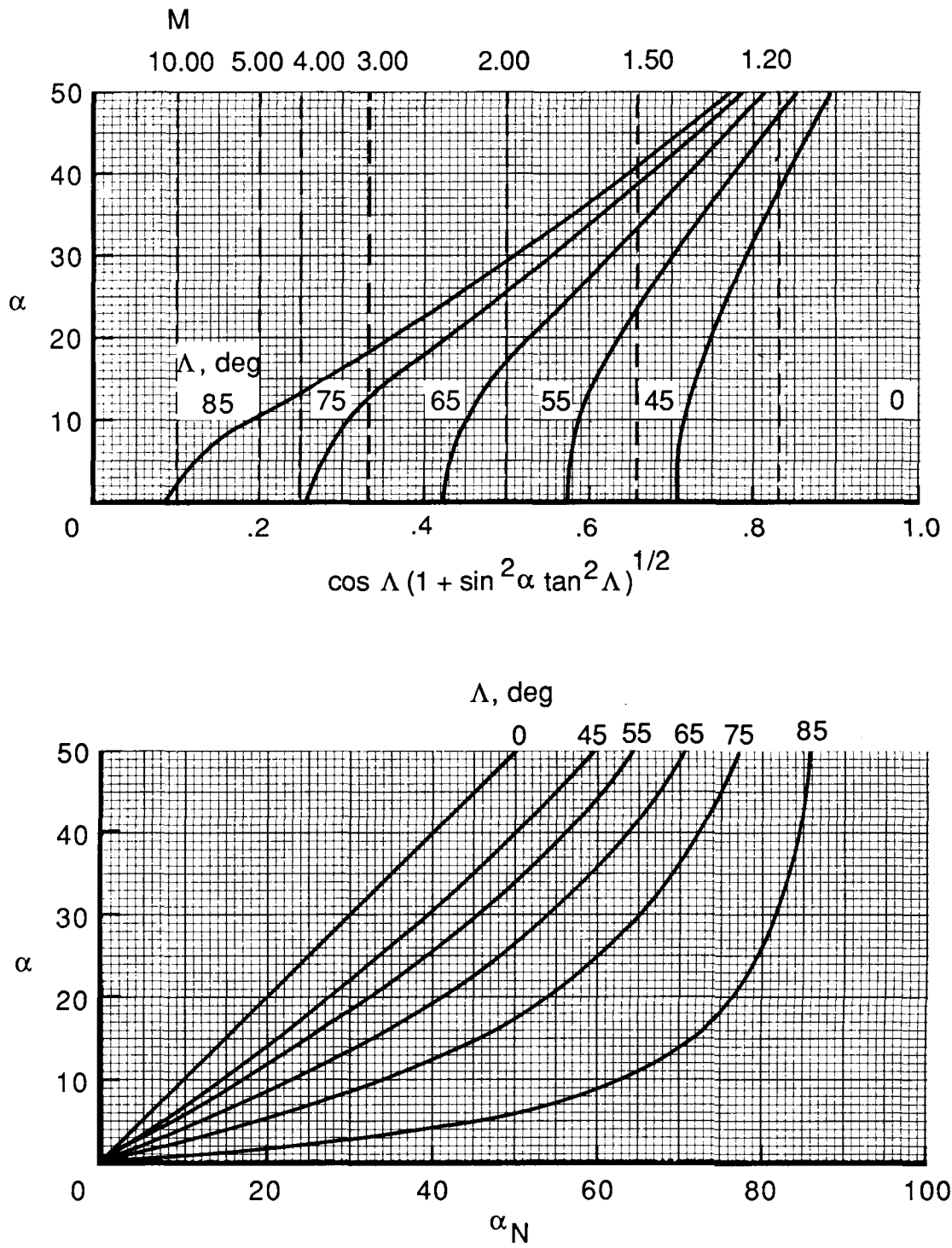


Figure 61. Variation of M_N and α_N with α .

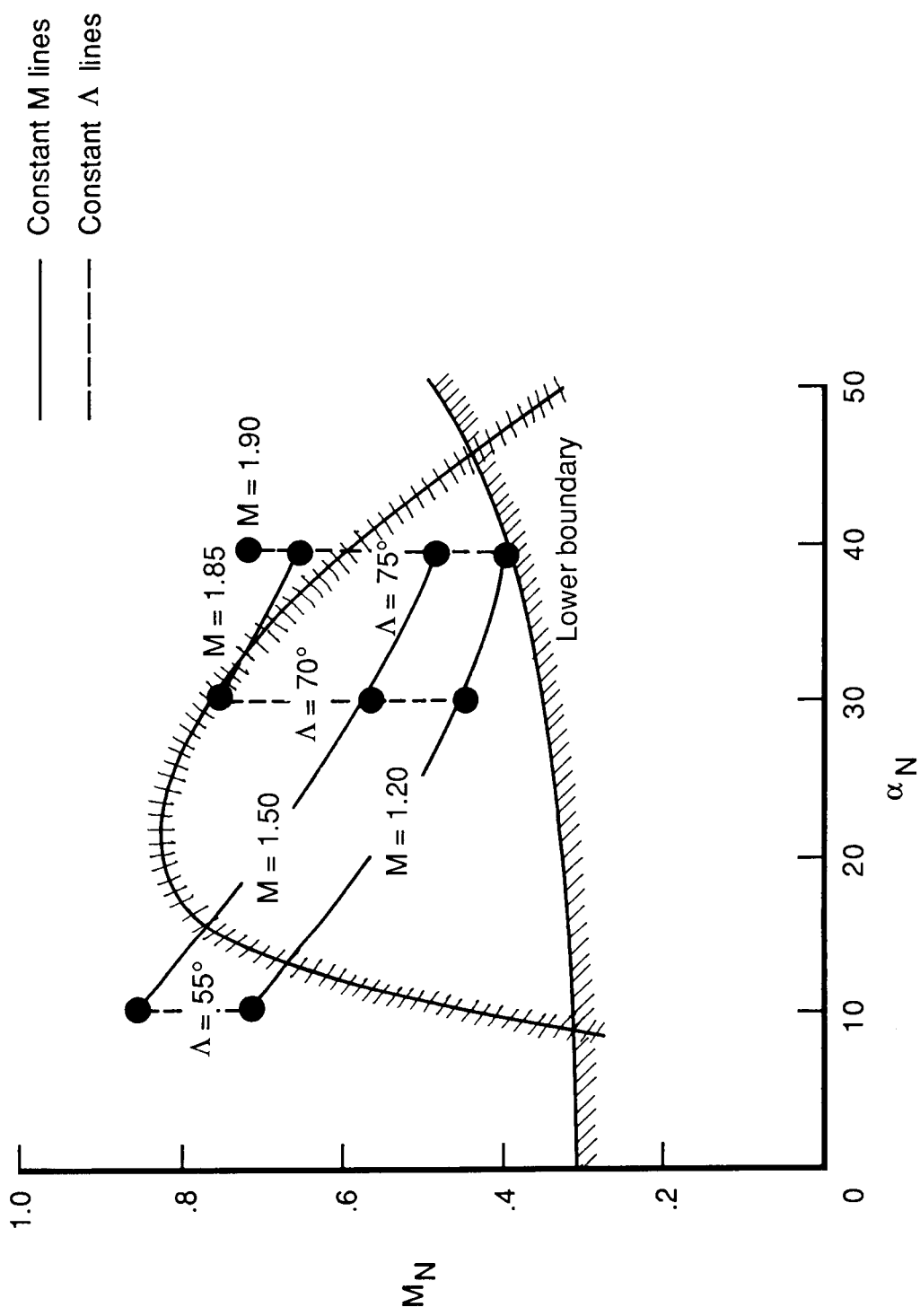


Figure 62. Wing design space concept.

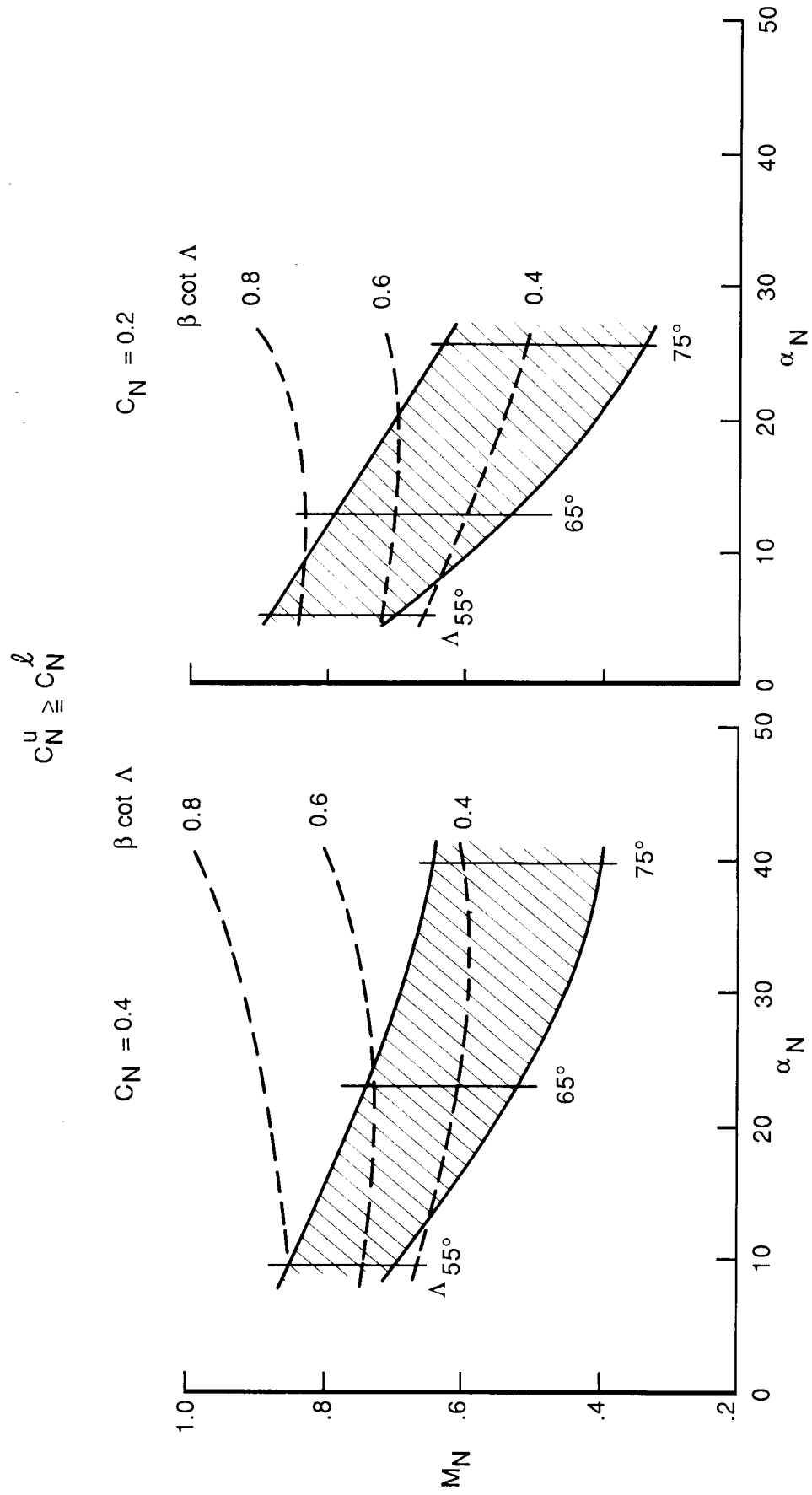


Figure 63. Relationship between wing design space and $\beta \cot \Lambda$.

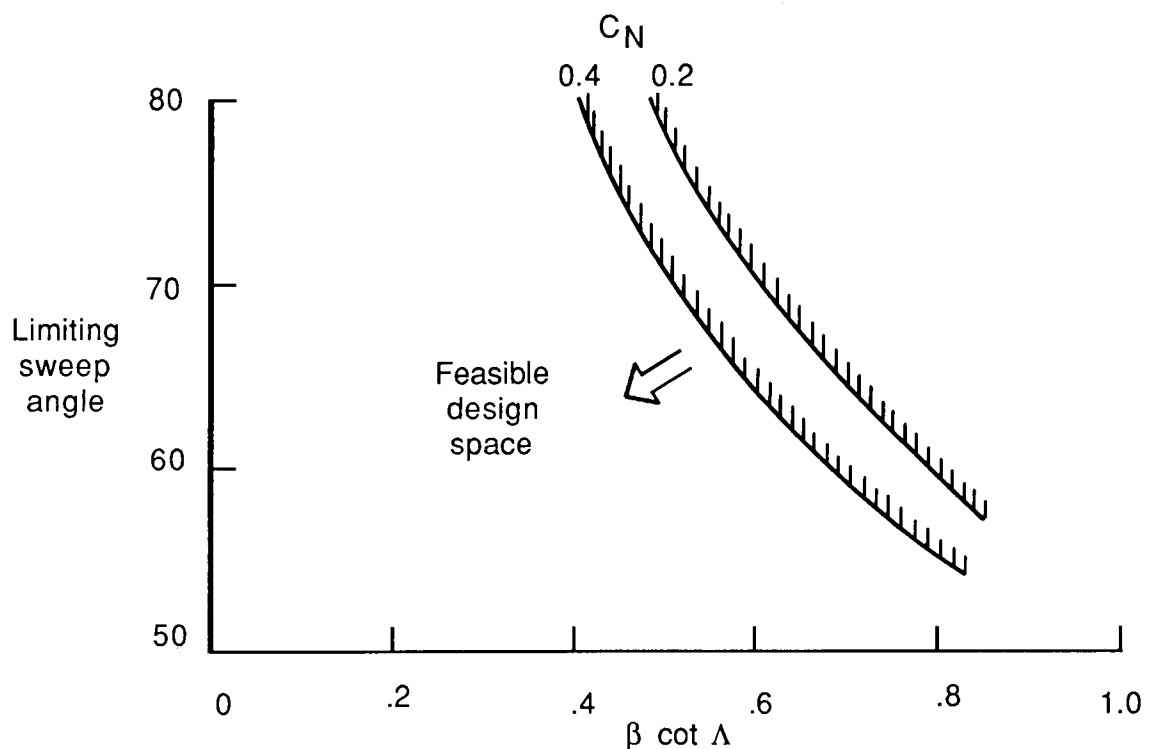


Figure 64. Identification of limiting leading-edge sweep angle.

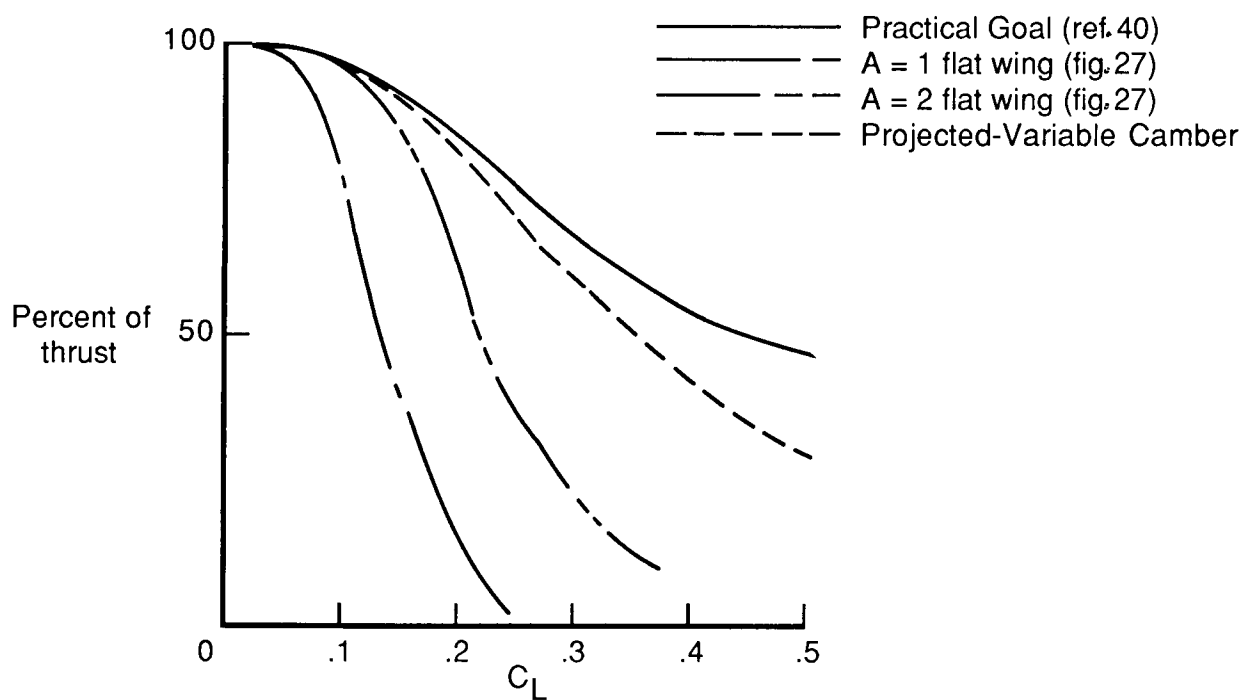


Figure 65. Identification of practical aerodynamic performance goals.



National Aeronautics and
Space Administration

Report Documentation Page

1. Report No. NASA TP-2771	2. Government Accession No.	3. Recipient's Catalog No.		
4. Title and Subtitle Supersonic Aerodynamics of Delta Wings		5. Report Date March 1988		
7. Author(s) Richard M. Wood		6. Performing Organization Code		
9. Performing Organization Name and Address NASA Langley Research Center Hampton, VA 23665-5225		8. Performing Organization Report No. L-16212		
12. Sponsoring Agency Name and Address National Aeronautics and Space Administration Washington, DC 20546-0001		10. Work Unit No. 505-61-71-01		
15. Supplementary Notes		11. Contract or Grant No.		
16. Abstract <p>Through the empirical correlation of experimental data and theoretical analysis, a set of graphs have been developed which summarize the inviscid aerodynamics of delta wings at supersonic speeds. The various graphs which detail the aerodynamic performance of delta wings at both zero-lift and lifting conditions were then employed to define a preliminary wing design approach in which both the low-lift and high-lift design criteria were combined to define a feasible design space.</p>		13. Type of Report and Period Covered Technical Paper		
17. Key Words (Suggested by Authors(s)) Supersonic aerodynamics Delta wings Experiment Nonlinear methodology Wave drag		18. Distribution Statement Unclassified—Unlimited		
19. Security Classif.(of this report) Unclassified		20. Security Classif.(of this page) Unclassified	21. No. of Pages 104	22. Price A06